

---

# **Determination of the Higgs Decay Width at ILC**

---

**Masterarbeit in Physik**

von

**Claude Fabienne Dürig**

angefertigt im

**Physikalischen Institut**

vorgelegt der

**Mathematisch-Naturwissenschaftlichen Fakultät  
der Universität Bonn**

September 2012



1. Gutachter: Prof. Dr. Klaus Desch
2. Gutachter: Prof. Dr. Jochen Dingfelder

Physikalisches Institut  
Universität Bonn  
Nussallee 12  
D - 53115 Bonn

September 2012



## Abstract

This thesis deals with the determination of the total Higgs decay width at the ILC. We perform a model-independent measurement of the Higgs production cross section through WW-fusion  $e^+e^- \rightarrow \nu_e\bar{\nu}_eH$ . From this measurement we can extract information on the coupling  $g_{HWW}$  of the Higgs boson to W-bosons and determine the total decay width of the Higgs boson. The aim of this study is to estimate the measurement accuracies of the total decay width obtainable at the ILC at  $\sqrt{s} = 250$  GeV. The Standard Model Higgs boson with a mass below 140 GeV is expected to decay predominantly into two b-quarks. By using this decay mode the WW-fusion cross section can be measured to an accuracy between 7.2% and 24.32% for  $m_H = 120$  GeV to  $m_H = 140$  GeV, assuming  $250\text{ fb}^{-1}$  of data. The measurement accuracy of the total Higgs decay width varies between approximately 9.0% and 24.44% in the Higgs mass range under consideration.



## Acknowledgements

First of all I would like to thank Prof. Klaus Desch for giving me the opportunity to write my thesis under his supervision, for his sound advice and patience. A special thanks to my co-supervisor, Philip Bechtle, for his inexhaustible help in word and deed. Also, I would like to thank the entire group for providing a nice environment and for lending a helping hand when it was needed. Furthermore, I wish to thank the FLC group at DESY, especially Jenny List and Mikael Berggren, for the help and assistance they provided during the last year.

I would like to thank my aunt and uncle, Beate and Volker, for providing me a home away from home. Just knowing you are there makes things better. Above all, I wish to thank Clemens Wieck for putting up with me through periods of frustration. This work was enhanced and made easier by you being in my life. Lastly, and most importantly, I wish to thank my family - my brother and my parents - for the unfailing encouragement, the endless support and for loving me throughout my life. I know that wherever life brings me, I have you. Dad, you are in my heart as an inspiration and a guide, and there is much of you in this thesis, as there is in all that I do. To Mum, Dad and Olli - my little “Masterpiece” is for you.



# Contents

<b>1</b>	<b>Introduction and Thesis Outline</b>	<b>1</b>
<b>2</b>	<b>Theoretical Background</b>	<b>3</b>
2.1	The Standard Model of Particle Physics . . . . .	3
2.2	The Standard Model Higgs Boson . . . . .	5
2.2.1	Higgs Mechanism . . . . .	5
2.2.2	Properties of the Higgs Boson . . . . .	11
<b>3</b>	<b>Experimental Environment</b>	<b>15</b>
3.1	ILC – The International Linear Collider . . . . .	15
3.2	Basic Design of the ILC . . . . .	16
3.3	ILC Detector Concepts . . . . .	17
<b>4</b>	<b>Software Framework</b>	<b>21</b>
<b>5</b>	<b>Signal Process and Background Events</b>	<b>23</b>
5.1	Signal Process . . . . .	23
5.2	Background Processes . . . . .	25
<b>6</b>	<b>Measurement of the Total Higgs Decay Width</b>	<b>33</b>
6.1	Event Selection . . . . .	35
6.2	Determination of the Cross Section $\sigma(\text{WW-fusion})$ . . . . .	47
6.3	Determination of the Total Decay Width of the Higgs Boson . . . . .	55
<b>7</b>	<b>Conclusion and Summary</b>	<b>59</b>
<b>A</b>	<b>Histograms</b>	<b>63</b>

A.1	$m_H = 120 \text{ GeV}$	63
A.2	$m_H = 126 \text{ GeV}$	65
A.3	$m_H = 130 \text{ GeV}$	68
A.4	$m_H = 140 \text{ GeV}$	71
<b>List of Figures</b>		<b>77</b>
<b>List of Tables</b>		<b>80</b>
<b>Bibliography</b>		<b>81</b>
<b>Eidesstattliche Versicherung</b>		<b>84</b>

# Chapter 1

## Introduction and Thesis Outline

In the 1960s and 1970s a theory emerged which has become well-tested over time and currently is the best description of the world of particle physics. The so-called *Standard Model* of particle physics has successfully explained experimental results and precisely predicted a large variety of phenomena, but it does not explain everything. It describes all the known fundamental particles, but only three out of the four fundamental forces. The *theory of almost everything* can neither answer questions about dark matter particles, nor does it account for neutrino oscillations, just mentioning two examples. In 1964 the *Higgs boson* was postulated, a massive scalar particle which is a key building block in the Standard Model, as it explains the origin of particle masses, but it was not found for almost 50 years. On the 4th of July 2012 the ATLAS and CMS working groups at the *Large Hadron Collider* (LHC) finally confirmed the observation of a Higgs-like particle with a  $5\sigma$  level of validation.

The largest new project in particle physics after the LHC is the *International Linear Collider* (ILC). A collider like ILC is called *precision machine*, since it is able to precisely measure particle properties and physics effects that are found at a *discovery machine* like LHC, thus making it a logical complement to it. One of the most important parts of the ILC physics programme is a precision test of the Standard Model predictions of the Higgs boson. The investigation and precise determination of Higgs boson properties includes without limitation the absolute branching ratios of the Higgs boson in all possible decay modes, getting information on the Higgs boson coupling to other particles in proportion to its mass, as well as the determination of the partial and the total decay widths.

In this analysis we perform a simulation measurement of the Higgs decay width at the ILC. We study the feasibility of the measurement for four Higgs masses 120 GeV, 126 GeV, 130 GeV and 140 GeV, along with a centre of mass energy of  $\sqrt{s} = 250$  GeV and an integrated luminosity of  $\mathcal{L} = 250 \text{ fb}^{-1}$ . The aim of this study is to estimate the measurement accuracies of the total decay width obtainable at the ILC at  $\sqrt{s} = 250$  GeV, since there are recent discussions of the possibility of staging the ILC and starting with a

“Higgs factory” operating at  $\sqrt{s} = 250$  GeV instead of  $\sqrt{s} = 500$  GeV.

The three main Higgs boson production processes in the Standard Model are WW-fusion, ZZ-fusion and Higgs-strahlung. Higgs-strahlung and WW-fusion have production cross sections that are large enough for precision tests. Both processes provide direct access to the coupling between gauge bosons and the Higgs boson. The Higgs-strahlung cross section reaches its maximum at centre of mass energies close to  $\sqrt{s} = m_Z + m_H$ . The large Higgs-strahlung contribution at  $\sqrt{s} = 250$  GeV makes the analysis challenging, not forgetting about the generally large background at low centre of mass energies. The Standard Model Higgs boson with a mass below 140 GeV is expected to decay predominantly into a  $b\bar{b}$  final state. Therefore we perform the measurement of the Higgs decay width through a WW-fusion process with the Higgs boson decaying into two b-quarks. By measuring the WW-fusion cross section through the process  $e^+e^- \rightarrow b\bar{b}\nu_e\bar{\nu}_e$ , we get direct access to the coupling  $g_{HWW}$  of the Higgs boson to W-bosons which then provides us the possibility to determine the total Higgs decay width with only small model-dependence. By using the relation between partial and total decay width and by exploiting the proportionality between coupling and cross section and partial decay width, respectively, the measurement of the WW-fusion cross section can be transformed into a measurement of the partial and thus into a measurement of the total Higgs decay width.

In chapter 2 we give an introduction to the Standard Model of particle physics and the Higgs boson properties that are important for the analysis. In chapter 3 a short introduction to the ILC is given. Since the LHC is a discovery machine for the Higgs boson, which is unable to determine total cross sections, it is difficult to make absolute measurements of the total decay width. Precise and model-independent measurements can be performed at a linear collider like ILC. We discuss the importance of the ILC project and give a short overview of the basic design and the detector model. The signal and background events used in the analysis have to be generated, simulated and finally reconstructed before an analysis can be performed. A short introduction to the software framework is given in chapter 4, before we discuss the signal and background processes in chapter 5. There are various backgrounds that can cause a signal similar to the desired Higgs signal. We discuss all important background processes in detail and comment on the WW-fusion signal. In chapter 6 each step of the analysis is described in detail. First of all, we want to remove as much of the background and extract as much of the Higgs signal as possible. Therefore, we start the analysis by applying various selection cuts, the motivation and results of which are discussed in detail. After the selection we determine the measurement accuracies of the WW-fusion cross section by applying a  $\chi^2$ -fit on the missing mass distribution consisting of the remaining signal and background events. We compare the results to a former study, give an estimation of the Higgs-strahlung cross section and a short overview of the coupling. The final part is the determination of the Higgs decay width measurement accuracies, which we compare to other indirect methods. In chapter 7 a summary and a conclusion is given.

# Chapter 2

## Theoretical Background

In this chapter we give a short introduction to the physical background which is important for the analysis. We start with a brief review of the Standard Model of particle physics, before we discuss the Standard Model Higgs boson and its properties.

### 2.1 The Standard Model of Particle Physics

In the 1960s and 1970s a theory emerged that described all of the known elementary particle interactions, except gravity. This theory is based on two families of elementary particles: quarks and leptons. It includes quantum chromodynamics (QCD) and the Glashow–Salam–Weinberg theory of electroweak interactions, which contains quantum electrodynamics (QED). This theory has come to be called the *Standard Model* (SM) of particle physics [1].

In the current view, the basic constituents of all matter are three kinds of elementary particles: leptons and quarks, both are structureless and point-like fermions, as well as the mediators for the different types of interaction. There are six leptons and six flavours of quarks, which fall naturally into three generations (tab. 2.1). Each lepton and each quark has a corresponding antiparticle with the same quantum numbers of opposite sign. In total, there are 12 leptons and 12 quarks.

Mathematically, the SM is built upon the requirement of *local gauge invariance* under the gauge group  $SU(3)_C \times SU(2)_L \times U(1)_Y$ , accounting for the strong, weak and electromagnetic interaction. The indices represent the charges of the groups, respectively:  $C$  for colour in QCD,  $L$  for left-handed isospin of the weak interaction and  $Y$  for hypercharge.

Every interaction has its mediators, the photon for the electromagnetic, the  $W^\pm$ - and  $Z$ -boson for the weak and the gluons for the strong interaction. The gauge bosons are listed in tab. 2.2. Particles which participate in strong interactions carry colour charge. There are three different colour charges - red, green and blue. Each gluon carries one unit of colour and one of anticolour. It would appear then, that there should be nine species of gluons. In

Particle	Flavour			$Q/ e $
leptons	e	$\mu$	$\tau$	-1
	$\nu_e$	$\nu_\mu$	$\nu_\tau$	0
quarks	u	c	t	+2/3
	d	s	b	-1/3

Table 2.1: Lepton and quark classification by their charge  $Q/|e|$  [2].

terms of  $SU(3)_C$  colour symmetry, these nine states constitute a colour octet and a colour singlet. Only colour singlet states can exist as free particles. Therefore, a colour singlet massless gluon would exist as a free particle and behave like a strong interacting photon, thus it would give rise to a strong force of infinite range. The strong force is of short range, therefore we know that physical gluons are confined. So we know there are eight physical gluons, represented by the colour octet [1]. Consequently, there are 12 gauge bosons in total.

Interaction	Mediator	$Q/ e $
strong	gluon g	0
electromagnetic	photon $\gamma$	0
weak	$W^\pm, Z$	$\pm 1, 0$

Table 2.2: The SM gauge bosons [2].

As mentioned before, the strong interaction can be described by the  $SU(3)_C$  symmetry group, where  $C$  indicates the colour charge. The symmetry group of the electromagnetic and the weak interactions is  $SU(2)_L \times U(1)_Y$ . The electromagnetic and weak interactions are unified by the Glashow–Salam–Weinberg theory. The  $SU(2)_L$  group describes transformations of left-handed multiplets of the weak isospin, and  $U(1)_Y$  describes phase transformations of the hypercharge  $Y$ . After spontaneous symmetry breaking of  $SU(2)_L \times U(1)_Y$  via the Higgs mechanism, as explained in the next section, only a  $U(1)$  symmetry will remain unbroken, the symmetry group describing the electromagnetic force. Furthermore,  $SU(2)_L$  and  $SU(3)_C$  are non-Abelian groups allowing self-coupling of the respective gauge bosons, whereas  $U(1)_Y$  is not. In QCD, the zero mass and the self-coupling of gluons give rise to *quark confinement*, which is the reason for quarks not to be observed as isolated particles. Quarks can only exist in form of colourless combinations called *baryons* ( $qqq$ ) and *mesons* ( $q\bar{q}$ ), which are generally called *hadrons*.

Leptons carry no colour charge, so they do not participate in strong interactions. Neutrinos are electrically neutral particles, carrying no charge  $Q/|e|$ , thus they experience no electromagnetic forces. Nevertheless, all of them join in the weak interactions. There are two kinds of weak interactions: *charged* (mediated by the  $W^\pm$ ) and *neutral* (mediated by the

$Z$ ). The primitive vertices for strong, electromagnetic, and neutral weak interactions all share the feature that the same quark or lepton comes out as went in - accompanied of course by a gluon, photon, or  $Z$ . In QCD the colour of a quark may change, but the flavour never does. The charged weak interactions are the only ones that can change flavour.

Although the SM currently is the best description of the subatomic world, it is incomplete and there is still much to be learned about. One of the major key building blocks in the SM of particles physics is the Higgs boson explaining the origin of particle masses. In 2012 the ATLAS and CMS working groups at the LHC announced the observation of a Higgs-like particle. It was postulated in 1964 and not found for almost 50 years.

## 2.2 The Standard Model Higgs Boson

### 2.2.1 Higgs Mechanism

As mentioned before, an important ingredient of modern particle physics is the spontaneous symmetry breakdown of  $SU(2)_L \times U(1)_Y$  to  $U(1)_{\text{em}}$ . In group theory language, three of the four generators of  $SU(2) \times U(1)$  are broken. Physically, this means that three of the SM gauge bosons gain masses ( $W_\mu^\pm$  and  $Z_\mu$ ) and one remains massless (the photon, denoted by  $A_\mu$ ). This process is called *Higgs mechanism*, named after one of its founders, Peter Higgs.

To understand the principles of spontaneous symmetry breakdown, let us look at a simple example, following [3, 4]. Consider a real scalar field  $\phi$  with Lagrange density

$$\mathcal{L} = \frac{1}{2}(\partial_\mu\phi)^2 - \frac{1}{2}\mu^2\phi^2 - \frac{1}{4}\lambda\phi^4, \quad (2.1)$$

with  $\mu, \lambda \in \mathbb{R}$ .  $\mathcal{L}$  is invariant under the discrete symmetry  $\phi \rightarrow -\phi$ . Since the potential  $V(\phi) = \frac{1}{2}\mu^2\phi^2 + \frac{1}{4}\lambda\phi^4$  must be bounded from below, we have  $\lambda > 0$ . For  $\mu^2$  both signs are possible, but only in the case  $\mu^2 < 0$  the ground state of  $\phi$  is non-vanishing:

$$\phi = \pm\sqrt{-\frac{\mu^2}{\lambda}}. \quad (2.2)$$

The potentials  $V(\phi)$  for  $\mu^2 < 0$  and  $\mu^2 > 0$  are illustrated in fig. 2.1. The ground state value in eq. 2.2 is called vacuum expectation value (VEV), denoted by  $v$ . From eq. 2.2 it is obvious that the theory at hand has two possible vacua. The important point is that either choice for  $v$  breaks the original reflection symmetry. To look at the properties of the system after symmetry breakdown, we expand the Lagrangian (eq. 2.1) around the VEV  $v$  in terms of a shifted field  $\eta = \phi - v$ . The result reads

$$\mathcal{L} = \frac{1}{2}(\partial_\mu\eta)^2 + \mu^2\eta^2 - \lambda v\eta^3 - \frac{1}{4}\lambda\eta^4. \quad (2.3)$$

We observe that  $\eta$  describes a particle with mass  $m_\eta = \sqrt{-2\mu^2}$ .

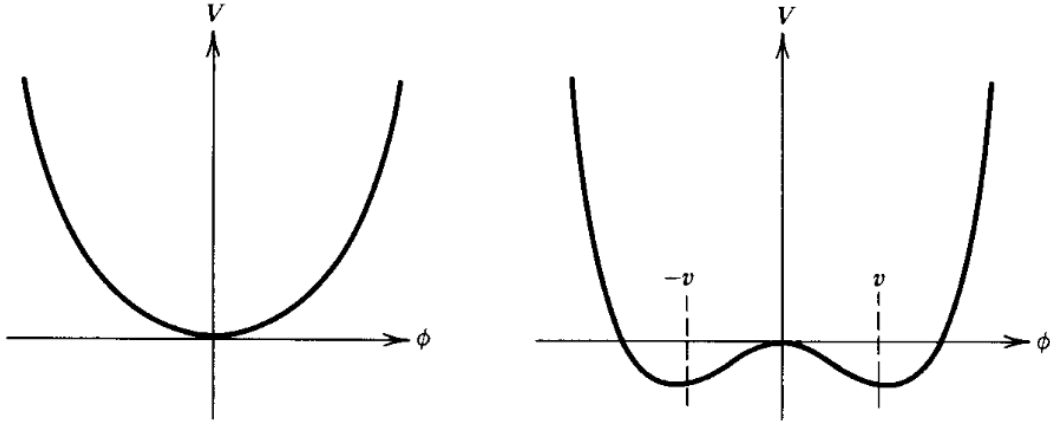


Figure 2.1: Potential  $V(\phi) = \frac{1}{2}\mu^2\phi^2 + \frac{1}{4}\lambda\phi^4$  for  $\mu^2 > 0$  (left) and  $\mu^2 < 0$  (right), and  $\lambda > 0$  [3].

Let us now look at the spontaneous symmetry breakdown of a  $U(1)$  gauge symmetry and the actual Higgs mechanism (from there, it is a short way to the case of  $SU(2)$  or  $SU(2) \times U(1)$ ). In this case the scalar field is taken to be complex and it transforms under  $U(1)$  as

$$\phi \rightarrow e^{i\alpha(x)}\phi. \quad (2.4)$$

The gauging procedure renders a Lagrangian of the form

$$\mathcal{L} = (\partial^\mu + ieA^\mu)\phi^*(\partial_\mu - ieA_\mu)\phi - \mu^2\phi^*\phi - \lambda(\phi^*\phi)^2 - \frac{1}{4}F_{\mu\nu}F^{\mu\nu}. \quad (2.5)$$

Here,  $\partial_\mu - ieA_\mu \equiv D_\mu$  is the covariant derivative and  $F_{\mu\nu}$  is the usual field strength of the gauge field  $A_\mu$ . As before, we choose  $\mu^2 < 0$  to achieve a ground state that is not invariant under the  $U(1)$  symmetry. A naive approach would be to expand eq. 2.5 in terms of the VEV of  $\phi$  and two real scalar fields:  $\phi(x) = \sqrt{\frac{1}{2}}(v + \eta(x) + i\xi(x))$ . We would then observe that  $\eta$  plays the same role as in our previous example, but  $\xi$  remains massless. In fact, this can be generalised by stating *Goldstone's theorem* [3]: Spontaneous breakdown of a continuous symmetry implies the existence of a massless, spinless particle.

However, it turns out that a more convenient approach is taking  $\phi(x) = \sqrt{\frac{1}{2}}(v + h(x))$ . Here,  $h$  is a real scalar, from now on called *Higgs boson*. Inserting this expression into eq. 2.5, we are left with

$$\mathcal{L} = \frac{1}{2}(\partial_\mu h)^2 - \lambda v^2 h^2 + \frac{1}{2}e^2 v^2 A_\mu^2 - \lambda v h^3 - \frac{1}{4}\lambda h^4 + \frac{1}{2}e^2 A_\mu^2 h^2 + v e^2 A_\mu^2 h - \frac{1}{4}F_{\mu\nu}F^{\mu\nu}. \quad (2.6)$$

From this we deduce the following facts: The theory now describes two interacting massive particles, the gauge boson  $A_\mu$  and the Higgs field  $h$ . In particular, no massless Goldstone boson appears in the Lagrangian, due to the particular choice of expression for  $\phi(x)$ . The Goldstone boson has been “eaten” by the gauge boson to render the latter massive [3]. This

is called Higgs mechanism. The mass of the Higgs boson

$$m_h = \sqrt{2\lambda v^2}, \quad (2.7)$$

is one of the most sought after parameters in modern particle physics.

A small caveat remains: As stated in the beginning of this chapter, the SM Higgs mechanism also involves an  $SU(2)$  gauge symmetry. The mathematics in this case is more complicated, the complete calculation can be found in the literature [3, 4, 5] and is beyond the scope of this thesis. Performing the computation correctly, one can deduce that after symmetry breakdown of  $SU(2)_L \times U(1)_Y$  one obtains mass terms for three of the four gauge bosons. To achieve this, the field  $\phi$  is chosen to be an  $SU(2)_L$  doublet with hypercharge  $Y = 1$ . When  $\phi$  obtains a VEV the symmetries under which it is charged are spontaneously broken, as in our simple examples. It turns out that there is one unbroken symmetry left over, which is a combination of  $SU(2)_L \times U(1)_Y$ . It is a  $U(1)$  symmetry with generator

$$Q = T_L^3 + \frac{1}{2} Y \equiv Q_{\text{em}}, \quad (2.8)$$

where  $\vec{T}_L = \frac{1}{2}\vec{\sigma}$  are the generators of  $SU(2)_L$ .  $Q$  generates exactly the symmetry group of electromagnetism, and the massless gauge boson of the unbroken symmetry is the photon. Specifically, the new gauge bosons after symmetry breakdown are defined as follows. Denoting the gauge bosons of the original  $SU(2)_L$  symmetry by  $W_\mu^a$ , where  $a = 1 \dots 3$ , and the one of  $U(1)_Y$  by  $B_\mu$ , one defines the physical  $W^\pm$ -bosons by

$$W_\mu^\pm = \sqrt{\frac{1}{2}} (W_\mu^1 \mp i W_\mu^2). \quad (2.9)$$

The photon and the Z-boson are given by a linear combination of the form

$$A_\mu = B_\mu \cos \theta_W + W_\mu^3 \sin \theta_W, \quad (2.10a)$$

$$Z_\mu = -B_\mu \sin \theta_W + W_\mu^3 \cos \theta_W, \quad (2.10b)$$

where  $\theta_W$  denotes the so-called *Weinberg angle*, the mixing angle of electroweak interactions. It is defined by the ratio of the coupling constants of  $SU(2)_L$  and  $U(1)_Y$ , denoted by  $g$  and  $g'$ :

$$\tan \theta_W = \frac{g'}{g}. \quad (2.11)$$

Using this mixing angle, one can express the coupling constant of the unbroken  $U(1)_{\text{em}}$  gauge symmetry as

$$e \equiv g \sin \theta_W = g' \cos \theta_W. \quad (2.12)$$

Experimentally, the value of  $\theta_W$  has been determined to be approximately  $30^\circ$  [6].

Now that we have described the origin of the SM gauge boson masses, let us turn to the fermions.

Up to now, the fermions remain massless in our discussion. To understand how mass terms for the latter can be generated, let us have a closer look at the quantum numbers of the Higgs field  $\phi$  under  $SU(2)_L \times U(1)_Y$ . Being a doublet of  $SU(2)$  it can combine with an antidioublet (e.g the left-handed fermionic antidioublet  $\bar{L}$ ) to a gauge invariant singlet. We observe that new terms of the form

$$\mathcal{L}_{\text{Yuk}} = -G(\bar{R}\phi^\dagger L + \bar{L}\phi R), \quad (2.13)$$

where  $G = \text{const.}$  and  $R$  denotes a right-handed  $SU(2)$  singlet, are now gauge invariant, since also the hypercharges of the couplings add up to zero. Couplings of the form 2.13 are called *Yukawa couplings*. The intriguing feature of these is that fermionic mass terms are generated once  $\phi$  gets a VEV.

We conclude that the Higgs mechanism generates mass terms for gauge bosons of broken symmetries. In addition, the Higgs field is responsible for the fermionic mass terms in the SM via its Yukawa couplings.

## Higgs Boson Search and Mass Constraints

The existence of a neutral scalar particle, the Higgs boson, is predicted by the Higgs mechanism. The theory does not predict its mass, from now on denoted by  $m_H$ , but only gives a forecast of its couplings to fermions and to gauge bosons as a function of  $m_H$ .

Today the Higgs boson search is carried out at LHC, taking advantage of results from former experiments which give information about the allowed Higgs boson mass region. In the 1990s at LEP, which shut down in 2000, the Higgs boson has been produced in association with a Z-boson. In the LEP1 phase, the  $e^+e^-$ -collider operated at centre of mass energies close to  $m_Z$ . During the LEP2 phase, the centre of mass energy was increased, reaching 209 GeV. It was able to exclude Higgs boson masses below 114.4 GeV in direct Higgs searches. Indirect constraints about the Higgs mass could be obtained from electroweak precision measurements when accounting for the Higgs boson's quantum effects. At LEP and SLC in Stanford, the Z-boson production could be studied with great precision, making the experiments sensitive to quantum effects coming from the Higgs boson. A similar sensitivity could be obtained from precision measurements of the W-boson mass, which have been performed at LEP and at the Tevatron in Illinois, at which the Higgs search continued. Taking all precision measurements together in a global fit, this yields an upper bound of the Higgs boson mass of 190 GeV at 95% confidence level (CL). A CL of 95% means that there is a probability of at least 95% that the result is reliable. Tevatron has operated at a centre of mass energy of 1.96 TeV. Combining the results of the two experiments CDF and DØ at Fermilab Tevatron, which shut down in 2011, a Higgs boson mass between

$$156 \text{ GeV} < m_H < 177 \text{ GeV} \quad (2.14)$$

could be excluded. Moreover, the data have shown an excess of events with respect to the background estimation in the mass range between  $115 \text{ GeV} < m_H < 135 \text{ GeV}$  with  $2.2\sigma$ . Combining the constraints from the different experiments at LEP and Tevatron, leads to a SM Higgs boson mass range of

$$115 \text{ GeV} < m_H < 156 \text{ GeV}. \quad (2.15)$$

In December 2011, the ATLAS and CMS collaborations presented new results on the Higgs boson search using data that correspond to an integrated luminosity of  $4.9 \text{ fb}^{-1}$  collected at a centre of mass energy of  $7 \text{ TeV}$ . Both experiments excluded at 95% CL a SM Higgs boson in most of the mass region between about  $130 \text{ GeV}$  and  $400 \text{ GeV}$ .

The ATLAS working group published results of the Higgs search in the diphoton channel in which the largest excess with respect to the background was observed at  $126.5 \text{ GeV}$  with a local significance of  $2.8\sigma$  [7]. The Higgs mass range between  $113 \text{ GeV}$  and  $115 \text{ GeV}$ , and between  $134.5 \text{ GeV}$  and  $136 \text{ GeV}$  could be excluded at 95% CL. In the decay channel  $H \rightarrow WW \rightarrow l\nu l\nu$ , ATLAS could exclude the SM Higgs boson within the mass range of  $m_H = 145 \text{ GeV} - 206 \text{ GeV}$  [8]. In the search for four-lepton final states,  $H \rightarrow ZZ \rightarrow 4l$ , the CMS working group could exclude SM Higgs boson masses  $m_H > 134 \text{ GeV}$  [9]. They additionally observed an excess of the four-lepton invariant mass around  $119 \text{ GeV}$ ,  $126 \text{ GeV}$  and  $320 \text{ GeV}$ . The ATLAS and CMS collaborations could significantly narrow the allowed SM Higgs boson mass range to

$$115.5 \text{ GeV} < m_H < 127 \text{ GeV}. \quad (2.16)$$

On the 4th of July 2012, ATLAS and CMS presented an update of the Higgs searches, independently combining about  $5 \text{ fb}^{-1}$  of data collected at  $\sqrt{s} = 7 \text{ TeV}$  and more than  $5 \text{ fb}^{-1}$  at  $\sqrt{s} = 8 \text{ TeV}$ . Both experiments observed an excess in the diphoton invariant mass spectrum at about  $126 \text{ GeV}$  (fig. 2.2) with a local significance of  $4.5\sigma$  and  $4.1\sigma$ , respectively. Moreover, an excess in the four-lepton invariant mass spectrum around  $126 \text{ GeV}$ , which can be interpreted as a signal of the  $H \rightarrow ZZ \rightarrow 4l$  decay channel, is observed by both experiments with the significance of  $3.4\sigma$  and  $3.2\sigma$ , respectively. Combining all available channels, the significance of the signal is around  $5.0\sigma$  (fig. 2.3) for both ATLAS and CMS [10]. These results are published in the papers [11, 12].

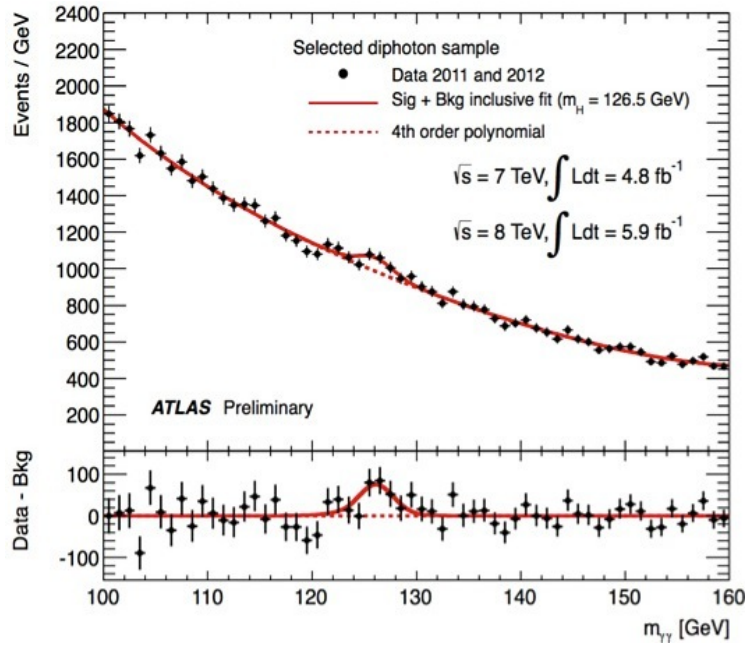


Figure 2.2: Mass distribution for the two-photon channel. The new Higgs-like particle appears as an excess around 126.5 GeV [11].

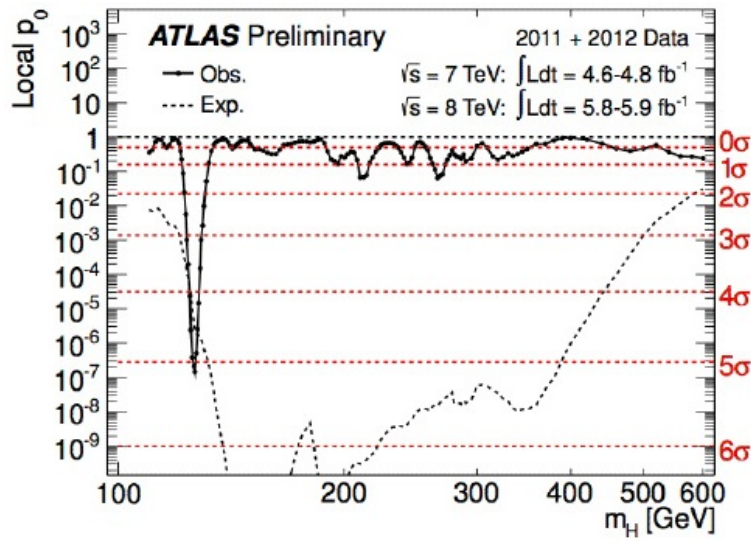


Figure 2.3: Probability of background to produce a signal-like excess. At 126.5 GeV there is an excess with  $5\sigma$  significance [11].

### 2.2.2 Properties of the Higgs Boson

#### Production Processes of the Higgs Boson

At a linear  $e^+e^-$ -collider the main Higgs production mechanisms are the WW-fusion, the ZZ-fusion and the Higgs-strahlung process (fig. 2.4):

$$\text{Higgs-strahlung: } e^+e^- \rightarrow Z^* \rightarrow ZH$$

$$\text{WW-fusion: } e^+e^- \rightarrow \nu_e\bar{\nu}_e WW \rightarrow \nu_e\bar{\nu}_e H$$

$$\text{ZZ-fusion: } e^+e^- \rightarrow e^+e^- ZZ \rightarrow e^+e^- H$$

The advantages of the Higgs-strahlung process are the well-known properties of the Z-boson. By detecting the products of the Z-boson, Higgs-strahlung allows the search of Higgs signals and the determination of its properties without any further assumptions on its decay mode and therefore no need to analyse its decay products.

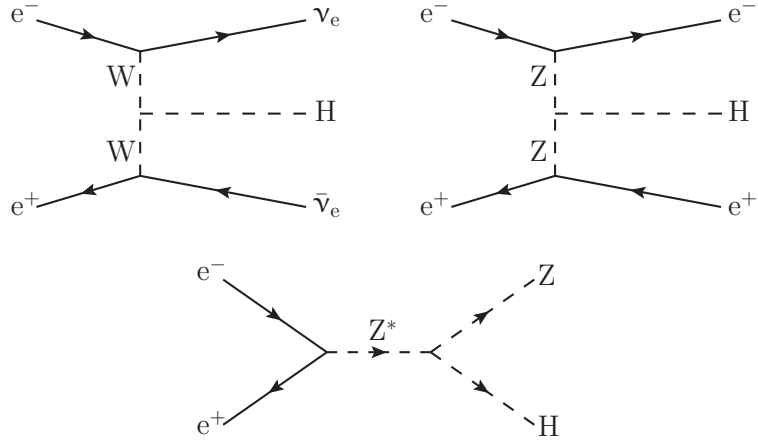


Figure 2.4: The main Higgs production channels: WW-fusion (top left), ZZ-fusion (top right) and Higgs-strahlung (bottom).

In Higgs-strahlung the Higgs boson is emitted from the Z-boson line, while WW-fusion and ZZ-fusion are formation processes of the Higgs boson in the collision of two quasi-real W- or Z-bosons radiated off the  $e^-$ - and  $e^+$ -beam. The cross section of the ZZ-fusion process is suppressed by one order of magnitude compared to the WW-fusion cross section, mainly due to the ratio of the neutral and charged couplings:  $16 \cos^4(\theta_W) \sim 9.5$  [13]. In contrast to Higgs-strahlung and WW-fusion this process is also possible in  $e^-e^-$ -collisions with approximately the same total cross section as in  $e^+e^-$ -collisions [13].

In the  $H\nu_e\bar{\nu}_e$  and  $He^+e^-$  final state, both Higgs-strahlung and the corresponding fusion

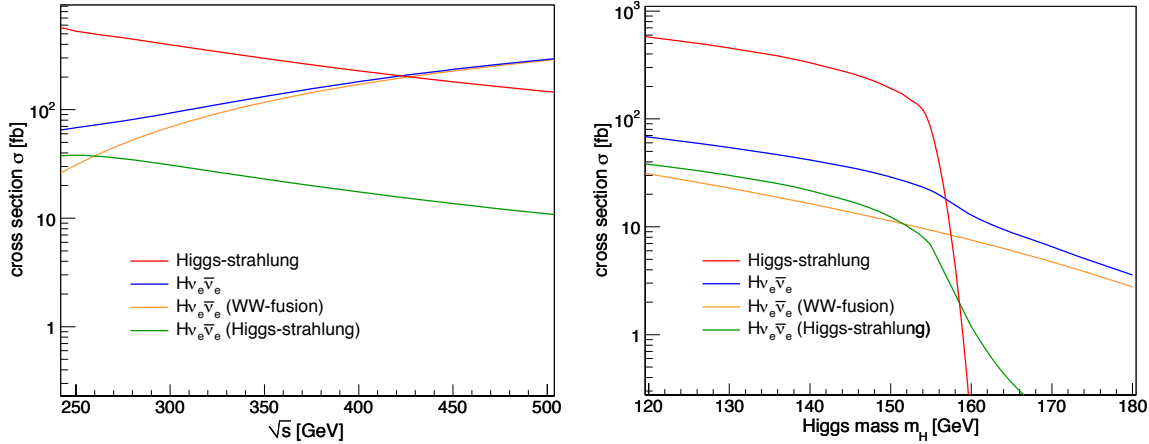


Figure 2.5: Production cross section  $\sigma$  as a function of  $\sqrt{s}$  for  $m_H = 120$  GeV (l.) and as a function of  $m_H$  for  $\sqrt{s} = 250$  GeV (r.).

process contribute non-negligible interference. The dependence of the different cross sections on the centre of mass energy  $\sqrt{s}$  is depicted in fig. 2.5. The production cross section of the Higgs-strahlung process scales as  $\frac{1}{s}$ , whereas the WW-fusion cross section increases as  $\log\left(\frac{s}{m_H^2}\right)$  [14]. For this reason and due to the enhanced cross section at  $\sqrt{s} = m_H + m_Z$ , the Higgs-strahlung diagrams give the dominant contribution to the combined process at low energies. As  $\sqrt{s}$  increases, the production cross section for Higgs-strahlung decreases, whereas WW-fusion becomes the dominant process [14].

## Branching Ratios of the Higgs Boson

The couplings of the Higgs boson to fermions and gauge bosons can be expressed as [15]

$$\begin{aligned} \text{coupling to fermions} \quad g_{Hff} &= [\sqrt{2}G_F]^{\frac{1}{2}} m_f, \\ \text{coupling to gauge bosons} \quad g_{HVV} &= 2 [\sqrt{2}G_F]^{\frac{1}{2}} m_V^2. \end{aligned}$$

The couplings depend on the mass of the gauge boson  $m_V$  or the fermion  $m_f$ , respectively.  $G_F$  denotes the Fermi coupling constant.

The branching ratio of each decay channel of the Higgs boson depends on the coupling and on the Higgs mass itself (fig. 2.6). In the mass region  $m_H \leq 140$  GeV, the Higgs boson mainly decays into a pair of b-quarks while the decay into  $\tau$ -leptons is the second most preferred decay mode. Nevertheless, once the decay channel into a pair of W-bosons opens, the Higgs boson is expected to decay into W-pairs due to the larger coupling to gauge bosons compared to the coupling to fermions. At the threshold  $m_H \gtrsim 2m_W$ , the branching ratio for the Higgs-decay into two W-bosons is about 100%. Beyond this threshold the decay proceeds almost entirely through  $H \rightarrow WW$  and  $H \rightarrow ZZ$  [14].

The measurement of branching ratios is one important topic in the ILC physics programme.

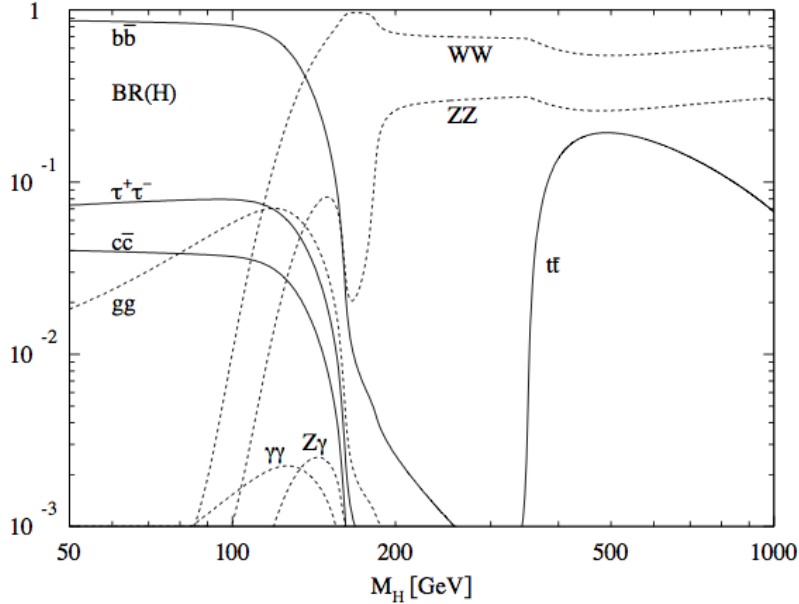


Figure 2.6: Branching ratios of the SM Higgs boson as a function of  $m_H$  [16].

For  $m_H \lesssim 140$  GeV many branching ratios can be measured, since  $b\bar{b}$ ,  $c\bar{c}$  and  $gg$  final states have large decay rates. These branching ratios allow the determination of the Higgs couplings to the corresponding particles. In general, for  $m_H \gtrsim 120$  GeV the branching ratio of  $H \rightarrow WW$  increases and allows the measurement of  $g_{HWW}$  in a model-independent way.

### Total Decay Width of the Higgs Boson

At Higgs masses  $m_H \leq 140$  GeV the total decay width is very narrow  $\Gamma_H^{\text{tot}} \leq 10$  MeV (fig. 2.7), whereas for  $m_H \geq 140$  GeV it increases rapidly [14]. Within a mass interval of approximately 30 GeV,  $\Gamma_H^{\text{tot}}$  increases from about 5 MeV to roughly 0.5 GeV. For  $m_H = 190$  GeV the total decay width is approximately  $\Gamma_H^{\text{tot}} \sim 1$  GeV. Beyond this threshold, it can be measured directly by reconstructing the Higgs boson line-shape [17]. Below this value the detector resolution on the Higgs boson mass is significantly larger than the natural width of the Higgs boson.

For light Higgs bosons the determination has to be performed using indirect methods. At a linear  $e^+e^-$ -collider, one can determine the coupling  $g_{HWW}$  by transforming the measurement of  $\sigma(WW\text{-fusion})$  into a measurement of the partial decay width  $\Gamma_H(H \rightarrow WW)$ . Since it is combined with the measurement of  $BR(H \rightarrow WW)$  the transformation is not completely free of model assumptions. Using the relation between total and partial decay width automatically leads to the determination of the total Higgs decay width  $\Gamma_H^{\text{tot}}$ . Another possibility is the measurement of the coupling  $g_{HZZ}$  from the Higgs-strahlung cross section  $\sigma(e^+e^- \rightarrow HZ)$ . The determination of the partial decay width  $\Gamma_H(H \rightarrow WW)$

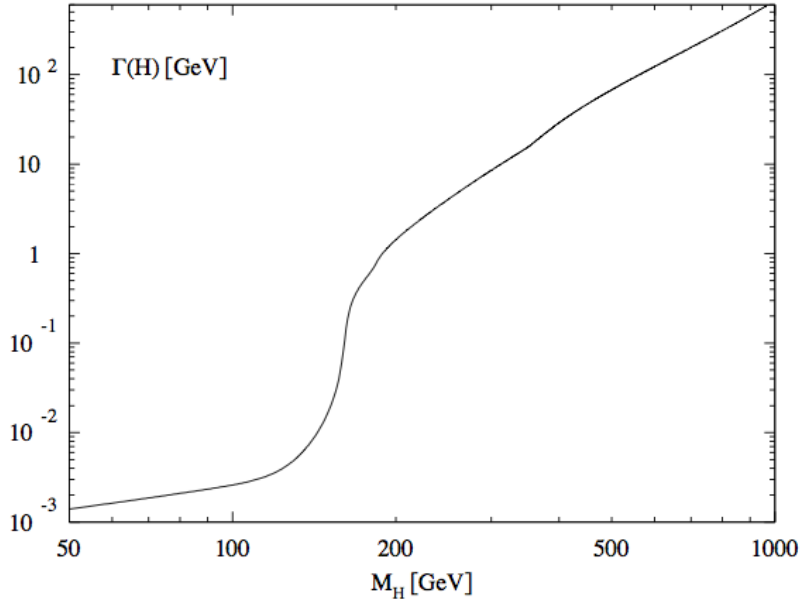


Figure 2.7: Total decay width of the SM Higgs boson as a function of  $m_H$  [16].

then follows from the  $SU(2) \times U(1)$  relation of the couplings  $g_{HWW}/g_{HZZ} = 1/\cos(\theta_W)$  [14]. This measurement is again combined with the measurement of  $BR(H \rightarrow WW)$ . In this case the accuracy of the Higgs decay width measurement then follows from that of  $BR(H \rightarrow WW)$  and  $g_{HWW}$ . Another possible indirect way of determination is via the measurement of the  $\gamma\gamma \rightarrow H$  cross section at a  $\gamma\gamma$ -collider combined with a measurement of  $BR(H \rightarrow \gamma\gamma)$  in  $e^+e^-$ -collisions [18].

## Chapter 3

# Experimental Environment

In this chapter we give a short introduction to the ILC, which is the new important project in particle physics. Since it is difficult to make absolute measurements of Higgs boson properties at the LHC, precise and model-independent measurements can be performed at a linear collider like ILC. There are recent discussions of the possibility of staging the ILC and starting with a machine running at  $\sqrt{s} = 250$  GeV for Higgs studies instead of 500 GeV. An overview of the ILC, its motivation, design and the major detector models is given.

### 3.1 ILC – The International Linear Collider

The main question one could ask concerning the ILC probably is:

*Why do we need a linear collider when we already have the LHC?*

The LHC is a *circular collider* using protons, which are not fundamental particles. The exact kinematic configuration of each collision and the centre of mass energy which is available for particle creation are unknown, since the energy is not equally distributed among the quarks and gluons. However, it is a source of an immense amount of different backgrounds. Thus, a circular hadron collider like LHC can be called *discovery machine*. It can be used for looking for new particles and new physics effects. A circular hadron collider provides high energies and luminosities at the expense of precision.

Now, what would differ when using leptons instead of hadrons in a circular collider? In a circular lepton collider, the problem of radiation losses would appear. Synchrotron radiation occurs when relativistic particles move through a magnetic field which forces them on a roughly circular trajectory. At high energies leptons are highly relativistic due to their small masses and the emitted photons represent considerable energy loss through synchrotron radiation [6].

However, in general, a lepton collider has several advantages over a hadron collider. First of all it has a well defined interaction point of the order of a few micrometers, which is

many orders of magnitude smaller than the LHC is able to obtain. Additionally, a lepton collider also has a well defined centre of mass energy since two point-like particles collide, compared to the collision of two composite particles in a hadron collider. As a result, the problem of not knowing the kinematic configuration and the centre of mass energy is not relevant at all. This cleaner environment helps during event reconstruction.

All these discussed advantages of lepton colliders without the drawback of radiation losses, which can be solved by guiding the beam particles along straight lines, are brought together in the concept of a linear lepton collider. An electron-positron linear collider can be called *precision machine*. It provides high precision and exactly known initial state conditions at the expense of energy and luminosity. Such a collider is able to precisely measure particle properties and effects that will be found at the LHC and thus is a logical complement to a discovery machine. Now that a Higgs-like particle is found at the LHC, one of the main topics of the physics programme at the ILC will be the investigation of the Higgs boson properties as well as the verification of Standard Model predictions. Furthermore, precision measurements of the top quark, Z-boson and W-boson properties can provide hints towards new physics [19].

## 3.2 Basic Design of the ILC

The ILC is planned to be operating in a continuos centre of mass energy range of  $\sqrt{s} = 200 \text{ GeV} - 500 \text{ GeV}$ , upgradeable to  $\sqrt{s} = 1 \text{ TeV}$  and with possible calibration runs at the Z-mass energy [20]. The basic design of the ILC is depicted in fig. 3.1. It consists of an electron and a positron accelerator, which have the shape of two almost identical arms. The electron source is a laser illuminating a photocathode in a DC gun. Free electrons, that are produced by the photoelectric effect, are accelerated to 150 keV [20]. The DC gun is located in the positron arm and generates 76 MeV electrons, which are then further accelerated to 5 GeV in super-conducting radio-frequency (RF) structures. Filled into the damping rings the  $e^-$ -beam is accumulated and the required bunch structure is created. The particle bunches circulate in the damping ring, lose energy via synchrotron radiation and are re-accelerated each time they pass through a cavity. The synchrotron radiation reduces the motion in all directions, while the cavity re-accelerates only those particles in the desired direction. Thus, the particle bunch becomes more and more parallel in motion, resulting in a significant reduction of the beam emittance. Then the electrons are injected into the main linac for acceleration. This is performed by approximately 280 RF cavities having an acceleration gradient of 31.5 MV/m [20]. Some bunches continue straight through to the interaction point, whereas electrons with an energy of 150 GeV are extracted from the main linac to generate positrons. They are diverted into the undulator, which acts as a source of high energy photons which are later converted into  $e^+e^-$ -pairs. The positrons get separated from the electrons and photons in the beam, accelerated up to

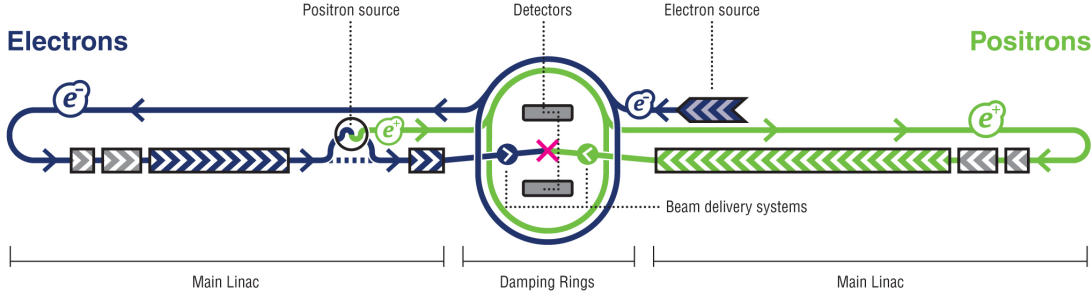


Figure 3.1: Basic design of the International Linear Collider [21].

5 GeV, and transported into the damping rings. From there on they follow a path through the linac until they reach the interaction point, which is identical to the one previously described for electrons. At the interaction point, the  $e^-$ - and  $e^+$ -beam are brought to collision under a crossing angle of 14 mrad [20]. Typical for a linear collider, the ILC provides only one interaction point. In order to be able to carry out more than one experiment at such a machine, the interaction point is going to be shared alternately by two independent moveable detectors in a so-called *push-pull* detector maintenance. Two independent detectors can be moved on and off beam line. In the first four years of operation it is planned to collect an integrated luminosity of  $500 \text{ fb}^{-1}$  [20]. The large range of the physics programme that can be performed at the ILC is challenging for the ILC detectors. There are recent discussions of staging the ILC and starting with a “Higgs factory” operating at  $\sqrt{s} = 250 \text{ GeV}$ . Building a machine for this centre of mass energy would amount to approximately 70% of the cost of the TDR machine. Another option is the construction of the whole tunnel for a  $\sqrt{s} = 500 \text{ GeV}$  machine but only installing half of the super-conducting cavities, which minimises the downtime between the phases of the machine. This option yields 80% of the cost of the TDR machine. A machine operating at  $\sqrt{s} = 500 \text{ GeV}$  yields 100% of the cost [22].

### 3.3 ILC Detector Concepts

In 2009, three detector concept groups submitted Letters of Intent to the *International Detector Advisory Group* (IDAG). The *International Large Detector* (ILD), the design of which is based on the *Global Large Detector* (GLD) and the *Large Detector Concept* (LDC), which both merged to form the ILD concept in 2007, as well as the *Silicon Detector Concept* (SiD) and the *Fourth Concept* (4th). Subsequently, the ILD and SiD concepts were validated by the IDAG and are encouraged to provide a technical design report of the two detectors in 2012. In the following, both detector models are described shortly. Further information and detailed descriptions of the detector concepts can be found in the respective detector outline documents [19, 23, 24].

## Silicon Detector Concept

Based on silicon technology, the main features of the SiD are the pixel vertex detector, the silicon tracking and silicon-tungsten electromagnetic calorimeter, as well as the hadronic calorimeter, and a muon system [25]. Silicon technology reaches huge insensitivity to radiation. The silicon vertex detector tracker and the calorimeter can absorb a large amount of background radiation without any sizeable damage. The fast readout of silicon detectors is the main advantage. Event cleanliness is improved due to the limited recording of backgrounds. The SiD systems only record backgrounds from a single bunch crossing accompanying a signal event [25]. The SiD employs *particle flow calorimetry* [26]. The detector placement is required to be within a solenoid. The radius is designed to be small in order to reduce the costs. A total magnetic field of 5 T within the solenoid would confine the electron-positron pairs to a minimal radius [25]. In order to compensate for the small radius, there has to be a consequent improvement of the vertexing performance.

## International Large Detector Concept

The design of the ILD is based on the GLD and the LDC detector concepts. Both the use of particle flow algorithms and similar structures were the reasons for merging the concepts. In both concepts, the main trackers are large Time Projection Chambers (TPC). The main difference comes from the overall size and the magnetic field. GLD plans a magnetic field of 3 T with larger geometry size, while a magnetic field of 4 T is foreseen for LDC [25]. The overall dimensions of the ILD are subject of current optimisation studies. The final ILD has a pixel vertex detector, which is placed at closest distance from the interaction point. It consists of several layers of silicon pixel sensors allowing accurate measurements of the positions of charged particles. The vertex detector is surrounded by the tracking system, the central component of which is the TPC providing up to 224 precise measurements along the track of a charged particle [25]. The tracking system in turn is surrounded by the calorimeters. An electromagnetic calorimeter (ECal) is optimised for the measurement of photons and electrons and a hadronic calorimeter (HCal) deals with hadronic showers. The super-conducting coil is placed outside the calorimeters to minimise the material budget between the calorimeters and the trackers as it is required by the particle flow. The ILD detector design asks for a 3.5 T magnetic field [25]. The detector is enclosed by a return yoke, which is instrumented for tail catching and muon identification purposes.

The main differences of the ILD and SiD lie in the presence of a TPC that replaces part of the silicon strip tracker, in the use of a lower magnetic field parameter (3.5 T instead of 5 T), and in the consequently resulting larger overall dimensions. By the choice of magnetic field the beam-pipe has to be slightly larger than in SiD (1.45 cm) in order to filter out most of the pair production background [25].

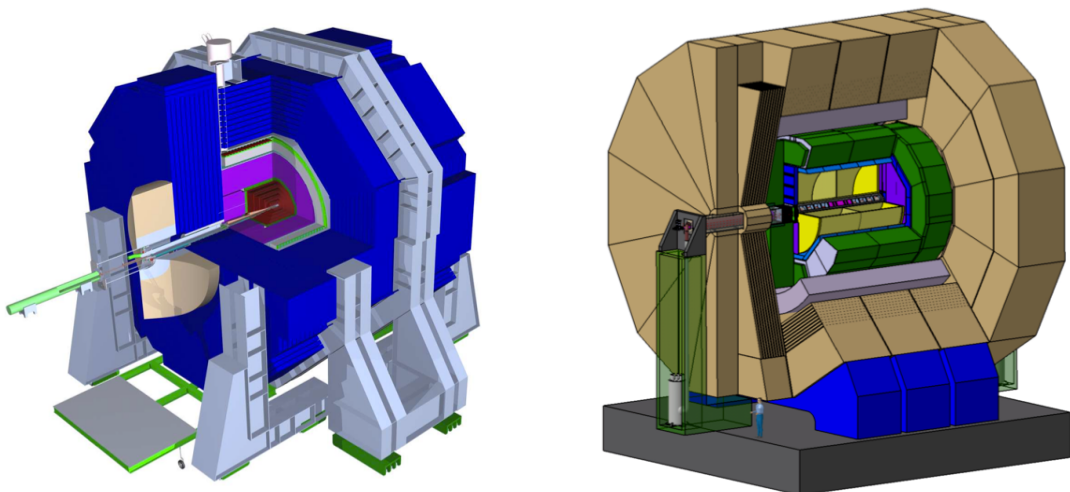


Figure 3.2: An artist's impression of the SiD detector [23] (left) and of the ILD detector [19] (right).



## Chapter 4

# Software Framework

The analysis is based on the knowledge of particle properties and their behaviour in the detector. In order to get information on the particles produced in  $e^+e^-$ -collisions in the ILC detector in a simulation measurement as it is conducted here, four major steps have to be performed. The signal and background processes used in the analysis have to be generated, simulated, reconstructed, and finally stored in a convenient data structure for further analysis. The different programmes used for each task are introduced shortly.

The events are generated using the Monte Carlo event generator WHIZARD 1.95 [27]. PYTHIA [28] is used for the decay and hadronisation of the events generated by WHIZARD. If the PYTHIA library is present it will be called for that purpose from inside WHIZARD, so no external interface is needed [29]. The events can be written to files in standard formats including ASCII (American Standard Code for Information Interchange), STDHEP (Standard High Energy Physics), the Les Houches event format (LHEF) or HEPMC (High Energy Physics Monte Carlo).

After the event generation we can simulate the passage of the particles through the detector material. For the simulation and reconstruction the ILC SOFTWARE framework [30] is used. In this analysis we use ILCSOFT version 01-11.

The interactions between the generated final state particles and the detector are simulated with MOKKA [31], an ILC-specific GEANT4-based full detector simulator. We use version mokka-07-06-p02. We can now simulate the passage of the particles through the detector material. Here, factors such as the magnetic field and the rate of energy loss of the particles in each major part of the detector are imposed on the moving particles. The physical properties of the detector material are always taken into account. Each layer of the detector is modelled separately. The input required by MOKKA includes the STDHEP file produced by WHIZARD, as well as a realistic detailed model of the full detector. In this study the detector model ILD\_00 is fully simulated.

As a reminder, starting inside the detector and moving outwards, the ILD\_00 detector model consists of a 6-layer vertex detector which offers a point resolution of  $3\text{ }\mu\text{m}$ , silicon internal and forward trackers, a TPC having about 224 sample points per track with point resolutions  $\geq 100\text{ }\mu\text{m}$ , silicon external and endcap trackers, ultra high granularity ECal and HCal, a super-conducting solenoid of 3.5 T, and return yokes with muon detectors [19, 25]. The transverse momentum resolution ( $\Delta(1/p_T) = \Delta(p_T)/p_T^2$ ) is expected to be  $2.0 \cdot 10^{-5}\text{ GeV}^{-1}$  asymptotically, worsening to  $9.0 \cdot 10^{-5}\text{ GeV}^{-1}$  at 10 GeV, and to  $9.0 \cdot 10^{-4}\text{ GeV}^{-1}$  at 1 GeV [19].

The MOKKA output consists of an LCIO file containing MCParticles and hits in the sub-detectors, as well as an XML file containing the geometry description of the different sub-detectors of the detector model, that is used for the simulation. GEAR [32] (GEometry API for Reconstruction) is the geometry package of the ILCsoft framework, in which the detector details are described using XML files. The *Linear Collider Input/Output* persistency framework (LCIO) [33] is the standard for ILC related detector studies. It provides a set of data classes which serve as persistency framework. In this study we use version v01-51-02.

After detector simulation, the reconstruction of the physics objects is performed with MARLIN (Modular Analysis and Reconstruction for the Linear Collider) [34]. It is a C++ application framework for LCIO data analysis and reconstruction code. We use MARLIN version v01-00. MARLIN uses as input the LCIO file which is provided by MOKKA. A steering mechanism reads the LCIO files and processes them on an event-by-event basis. There is a plug-in mechanism which allows to load modules, so-called processors, which perform the actual computing task. The processors analyse data in an LCEvent and create additional output collections that are added to the event. An XML steering file defines which processor to use with which data collection.

We use LCTUPLE for creating Ntuples for the final analysis. It is a MARLIN package that creates a simple ROOT [35] TTree with column-wise Ntuple structure from LCIO collections. The quantitative properties of the reconstructed particles and jets are stored in the Ntuple data structure and analysed using ROOT (version 5.28), an object-orientated framework for data analysis in high energy physics. The analysis includes the selection criteria, fit procedure, and extraction of the desired physics observables: mass, width, etc., as well as the achievable uncertainties of these quantities.

## Chapter 5

# Signal Process and Background Events

In our analysis we are looking for WW-fusion production processes which we refer to as *signal*. Processes that have topologies similar to the signal process thus giving wrong information are referred to as *background*. We shall strive to analyse and count as much of the signal events as possible and, equally important, suppress the contribution of the background to the data.

### 5.1 Signal Process

In  $e^+e^-$ -collisions, Higgs-strahlung and the WW-fusion process (cf. section 2.2.2) are both capable of generating the  $\nu_e\bar{\nu}_eH$  final state.

The corresponding leading order diagrams are depicted in fig. 2.4. WW-fusion is a process whereby both the incoming positron and electron convert into neutrinos radiating W-bosons, which fuse to form the Higgs boson. This production process has unique features, which provide us the direct measurement of the coupling of the Higgs boson to W-bosons and the determination of the total Higgs decay width. In our Higgs mass range  $m_H = 120 \text{ GeV} - 140 \text{ GeV}$ , the main Higgs decay mode is  $H \rightarrow b\bar{b}$  (cf. fig. 2.6). We will use this decay as our final state, so our signal consists of two jets with missing energy:

$$e^+e^- \longrightarrow \nu_e\bar{\nu}_eH \longrightarrow \nu_e\bar{\nu}_e b\bar{b}.$$

The WW-fusion process has the advantage of having a very clear signature of two energetic, strongly forward jets. In the  $\nu_e\bar{\nu}_eH$  final state, Higgs-strahlung and the WW-fusion process cannot be taken separately as non-interfering. The interference decreases the total Higgs boson production cross section [36]. Near the threshold energy  $\sqrt{s} = m_H + m_Z$  the contribution of Higgs-strahlung and WW-fusion are of the same order and the interference

term is not negligible:

$$\sigma(e^+e^- \rightarrow \nu_e \bar{\nu}_e H) = \sigma_{WW\text{-fusion}} + \sigma_{\text{Higgs-strahlung}} + \sigma_{\text{interference}}. \quad (5.1)$$

Therefore, we consider both mechanisms as interfering and generate the signal event sample  $e^+e^- \rightarrow \nu_e \bar{\nu}_e H$  with the event generator WHIZARD for the polarisation states  $P(e^+e^-) = (+1, -1)$  and  $P(e^+e^-) = (-1, +1)$  and combine them to a sample corresponding to the beam polarisation  $P(e^+e^-) = (0.3, -0.8)$ . We will have a closer look at this procedure later in this chapter.

Higgs-strahlung can also result in the final states  $\nu_\mu \bar{\nu}_\mu H$  and  $\nu_\tau \bar{\nu}_\tau H$ . Since we cannot distinguish between the different neutrino flavours, these final states have to be taken into account. Therefore we create a total  $\nu_l \bar{\nu}_l H$  final state sample to the corresponding beam polarisation and luminosity, which contains WW-fusion events, Higgs-strahlung events and the interference term. We expect the majority of events in the sample to be Higgs-strahlung events. The interference term is expected to be small. The event samples for the four different Higgs masses contain all possible Higgs boson decay channels. As discussed before, most of the events in the samples are expected to be  $H \rightarrow b\bar{b}$ , since it is the most preferred decay mode in the low Higgs boson mass range. We will try to reduce events resulting from the Higgs-strahlung process and events which are not  $\nu_e \bar{\nu}_e b\bar{b}$  final states later in the analysis.

## 5.2 Background Processes

### Processes with $b\bar{b}\nu_l\bar{\nu}_l$ final state

Next to Higgs-strahlung there are more background processes which can form a  $b\bar{b}\nu_l\bar{\nu}_l$  final state, representing a background very similar to our signal. It results in two jets consisting of b-quarks with large missing four-momentum. On the one hand, there are processes with electron neutrinos (fig. 5.2), which occur because of the exchange of a W-boson. On the other hand, there are processes that can happen for all the different neutrino flavours (fig. 5.3) [37]. This kind of background represents the so-called *irreducible background*.

### W-boson pair production

Semileptonic decays of W-boson pairs can cause a signal very similar to our Higgs signal. One W decays either into an electron or a muon and its associated neutrino, while the other W decays into a quark-antiquark pair:

$$e^+ e^- \rightarrow W^+ W^- \rightarrow \nu_l l^\pm q\bar{q}.$$

However, most of the time the resulting lepton appears to be isolated, whereas leptons in the signal appear in the jets at most [37]. The other two possible decay channels of the W-pair are the fully leptonic decay ( $\nu_l \nu_l \nu_l$ ), in which each W decays into a lepton and its associated neutrino, and the fully hadronic one, in which each W decays into two quarks:

$$e^+ e^- \rightarrow W^+ W^- \rightarrow q\bar{q} q\bar{q}.$$

The fully hadronic W-decay results in a four-jet final state, in which some of the light quark or c-jets can be misidentified as b-jets [37]. The near absence of b-quark production in W-decays can help to reduce the background substantially. The fully leptonic decay is excluded here. It could be easily reduced by the number of charged tracks, but it does not form a signal similar to ours anyway. The W-pair is emitted back-to-back, so in this process the decay products tend to be produced in the forward and backward direction with respect to the beam axis, thus resulting in low transverse momentum.

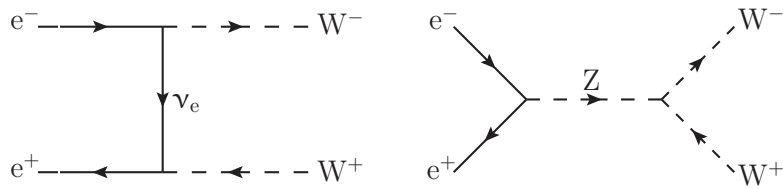


Figure 5.1: Feynman diagram of the W-boson pair production process via t-channel (l.) and via s-channel (r.).

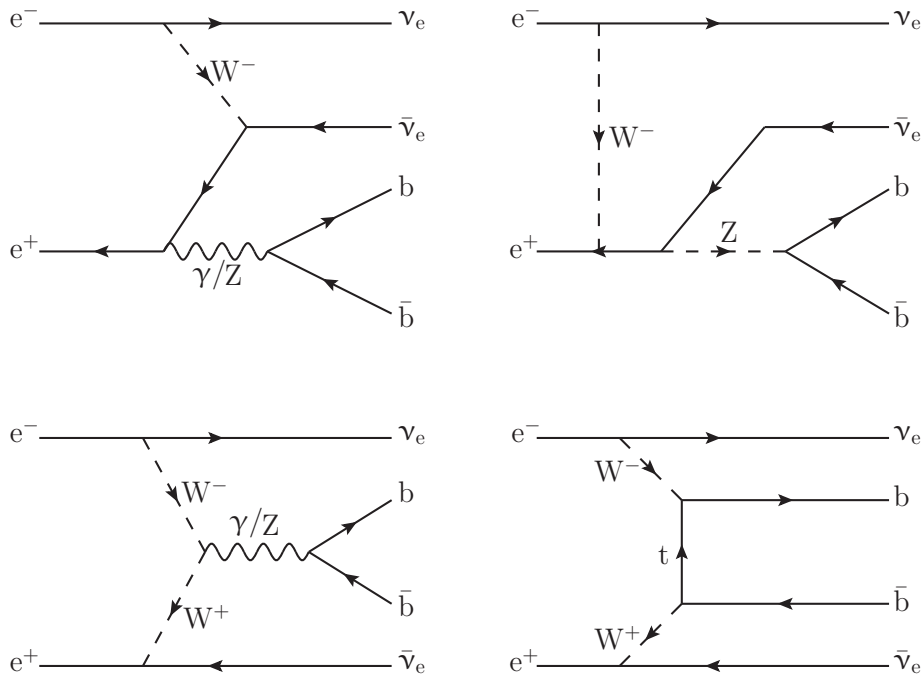


Figure 5.2: Feynman diagrams for background processes with  $b\bar{b}\nu_e\bar{\nu}_e$  final state, which occur exclusively for electron neutrinos via the exchange of a  $W$ -boson.

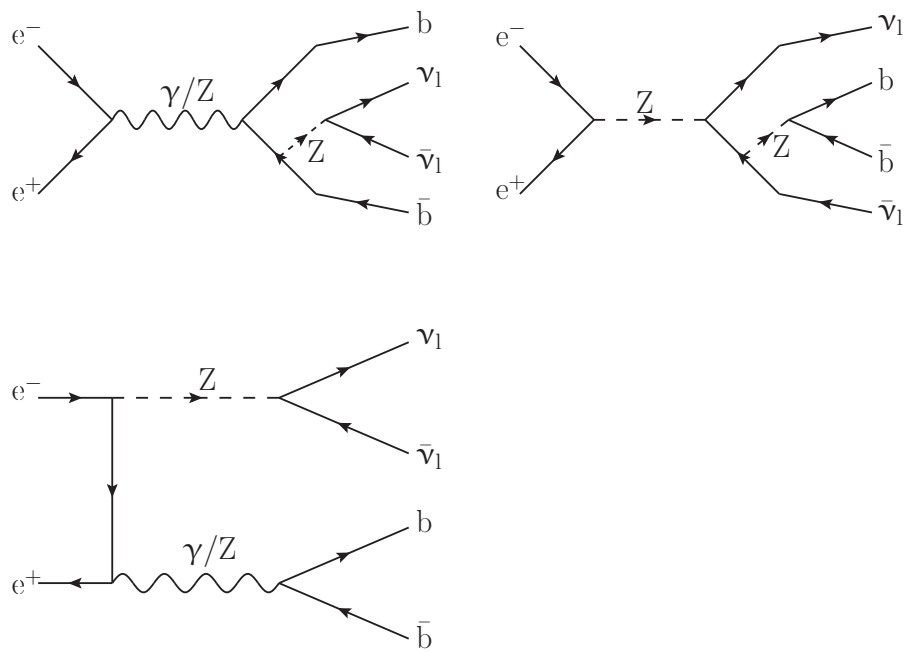


Figure 5.3: Feynman diagrams for background processes with  $b\bar{b}\nu_1\bar{\nu}_1$  final state. The processes occur for all of the three different neutrino flavours.

## Z-boson pair production

In the Z-boson pair production process  $e^+e^- \rightarrow ZZ$ , Z-bosons are produced at small angles from the  $e^+e^-$ -beams. Events associated with a certain geometrical distribution of the decay particles can be reduced by using this characteristic. Therefore, a cut on  $\cos(\theta_{\text{jet}})$ , where  $\theta_{\text{jet}}$  is the angle of the Z-boson with respect to the beam axis, is very effective for reducing Z-boson pair background. Analogous to the W-pair production, in the Z-pair production process the decay products are usually produced back-to-back, thus resulting in low transverse momentum. Furthermore, decay products of Z-pair and W-pair production processes are expected to be boosted stronger. There are three different final states, which can cause a signal in the detector which is similar to our signal process and therefore represent possible background. The first possible final state is

$$e^+e^- \rightarrow ZZ \rightarrow \nu_l \bar{\nu}_l q \bar{q}.$$

One Z-boson decays into neutrinos, whereas the other one decays into a quark-antiquark pair. This final state represents an irreducible background if the quark-antiquark pair is composed of b-quarks. This background is already taken into account in the background processes with  $b\bar{b}\nu_l\bar{\nu}_l$  final state, as discussed before.

Another possible final state is given by:

$$e^+e^- \rightarrow ZZ \rightarrow l^+l^-q\bar{q}.$$

In this case, there is at least one isolated lepton. Background events with  $l^-l^+q\bar{q}$  final state originate almost exclusively from Z-pair production processes.

Another potential background is given by four-jet events. Similar to the hadronic W-decay, the Z-pair can decay into a four-jet final state

$$e^+e^- \rightarrow ZZ \rightarrow q\bar{q}q\bar{q},$$

in which again some of the light quark or c-jets are misidentified as b-jets.

## Single W-boson and Z-boson production

Another important background is given by the production process of a single W-boson (fig. 5.5):

$$e^+e^- \rightarrow W^\pm e^\pm \nu_e \rightarrow \nu_e e^\pm q\bar{q}.$$

The W-boson is produced together with an  $e^\pm$  and a neutrino. Since the spectator  $e^\pm$  radiates a photon, it develops no appreciable transverse momentum and escapes undetected

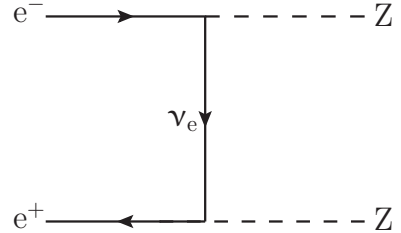


Figure 5.4: Feynman diagram of the Z-pair production process via  $\nu_e$  exchange in the t-channel.

down the beam-pipe. The other  $e^\mp$  couples to a  $W^\mp$  and the resulting neutrino carries away the transverse momentum of the order of the  $W$ -boson mass. The neutrino remains undetected. Decaying into two quarks, the  $W$  production process leaves a signature in the detector similar to our signal. Due to the near absence of  $b$ -quarks, this background can be reduced by using a *b-tagging algorithm*.

The production process of single  $Z$ -bosons (fig. 5.5) gives an additional background:

$$e^+ e^- \rightarrow Z e^- e^+ \rightarrow q \bar{q} e^- e^+.$$

The production of a single  $Z$ -boson is accompanied by an  $e^+ e^-$ -pair. The spectator  $e^\pm$  again escapes detection in the beam-pipe while the other  $e^\mp$  has low momentum and the system resembles a  $Z$ -boson production by *initial state radiation* (ISR). At least one final state lepton is isolated.

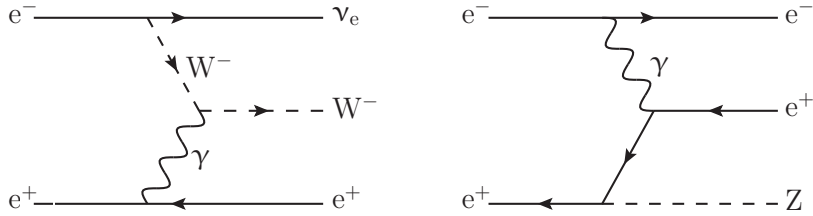


Figure 5.5: *Leading order Feynman diagrams of the production process of a single  $W$ -boson (l.) and a single  $Z$ -boson (r.).*

## Quark-antiquark pairs

The most tedious background is  $e^+ e^- \rightarrow q \bar{q}$  (fig. 5.6). The cross section of this process is more than 1000 times larger than the signal cross section. The two-fermion background can proceed via the exchange of a virtual  $Z$  or  $\gamma$ . The production of two fermions can be accompanied by radiating a real photon off the initial state electron or positron. This process does not occur at the full centre of mass energy. So-called *radiative returns*, which occur very often, decrease the effective centre of mass energy to roughly the  $Z$ -boson

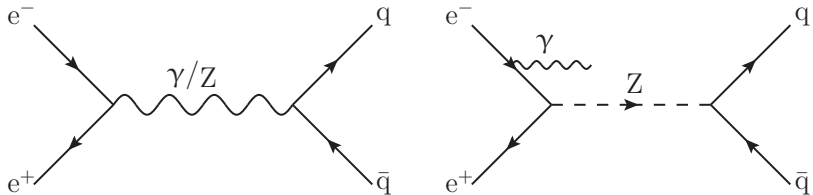


Figure 5.6:  *$q\bar{q}$ -pair production by  $\gamma$  or  $Z$  exchange (l.) and  $q\bar{q}$ -pair production via  $Z$ -boson with radiative returns (r.).*

resonance, so that a real Z-boson can be produced instead of a virtual one. Due to ISR photons, which are emitted at low angle and lost along the beam-line, the two-fermion process obtains large missing momentum. Additionally, quarks tend to be produced in forward direction so that part of the signal can remain undetected, which then results in missing four-momentum. The transverse momentum is very small in this case. Additionally, a  $q\bar{q}$ -pair can arise from two-photon interactions via the exchange of two virtual photons. The cross section of the two-photon interaction is very large, but their particular features allow to suppress them at an early stage of the analysis. The electron and positron are scattered at very low polar angles and then escape into the beam-pipe, carrying away almost the entire initial energy [38]. Therefore, background events from two-photon processes are found to be negligible in this analysis.

For the most important SM processes contributing to the background, the dependence of the production cross section on the centre of mass energy is illustrated in fig. 5.7. We expect that the  $q\bar{q}$  background gives the largest contribution to the background at  $\sqrt{s} = 250$  GeV.

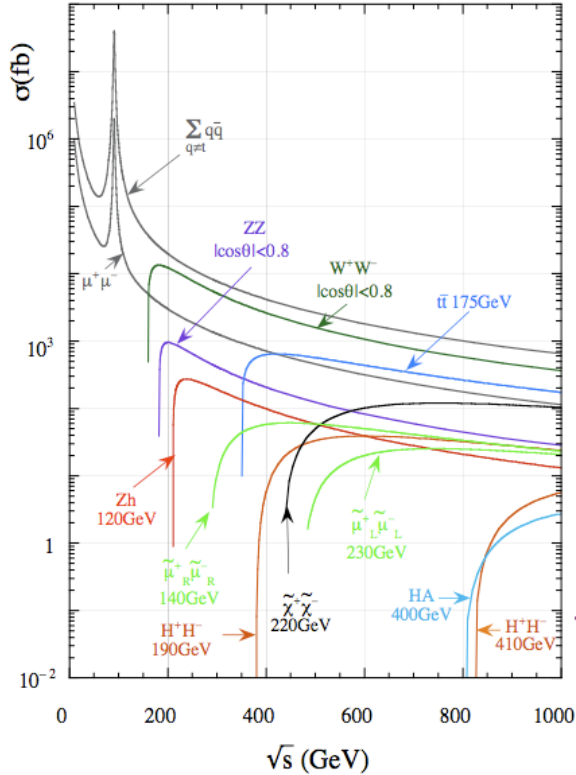


Figure 5.7: Production cross section  $\sigma$  for SM processes as a function of  $\sqrt{s}$  [39].

## Signal and Background Event Samples

As already mentioned, we generate a signal sample of the  $\nu_l \bar{\nu}_l H$  ( $l = e, \mu, \tau$ ) final state for the polarisation states  $P(e^+e^-) = (+1, -1)$  and  $P(e^+e^-) = (-1, +1)$ . After generating the events, we perform the ILD\_00 full detector simulation and event reconstruction as discussed in chapter 4. The samples have to be scaled to a beam polarisation of  $P(e^+e^-) = (0.3, -0.8)$ , since it is the polarisation used in the analysis. The ILC baseline design foresees a longitudinal electron polarisation of 80% and a positron polarisation of 30%. The latter can be increased to 60%. Therefore, we take both available polarisation state samples and combine them to a  $P(e^+e^-) = (0.3, -0.8)$  sample. In order to do so, we can generally express the cross section corresponding to the desired beam polarisation as [40]

$$\sigma_{P(e^+e^-)} = \left( \frac{1 - P_{e^-}}{2} \right) \left( \frac{1 + P_{e^+}}{2} \right) \sigma_{RL} + \left( \frac{1 + P_{e^-}}{2} \right) \left( \frac{1 - P_{e^+}}{2} \right) \sigma_{LR}, \quad (5.2)$$

where  $\sigma_{RL}$  stands for the cross section at  $P(e^+e^-) = (+1, -1)$  and  $\sigma_{LR}$  for  $P(e^+e^-) = (-1, +1)$ . In case of  $P(e^+e^-) = (0.3, -0.8)$ , the  $P(e^+e^-) = (+1, -1)$  state has a weight of 0.585 and the  $P(e^+e^-) = (-1, +1)$  state has a weight of 0.035:

$$\sigma_{0.3,-0.8} = 0.585 \cdot \sigma_{RL} + 0.035 \cdot \sigma_{LR}. \quad (5.3)$$

The number of events in the new  $\nu_l \bar{\nu}_l H$  samples for the four different Higgs masses are listed in tab. 5.1. Additionally, we give a rough estimation of the number of  $\nu_l \bar{\nu}_l b\bar{b}$  and  $\nu_e \bar{\nu}_e b\bar{b}$  events expected in each sample. The samples contain all possible decay modes of the Higgs boson, but we expect the majority of events to be Higgs-decays into b-quarks.

Additionally, we create WW-fusion and Higgs-strahlung samples in the same way, which we then compare to the  $\nu_l \bar{\nu}_l H$  samples to observe the interference term during the event selection. An estimation of the WW-fusion cross section and the expected number of WW-fusion events for each Higgs mass are listed in tab. 5.2. The Higgs-strahlung contribution in the signal samples is listed in tab. 5.3. The interference term is small.

As discussed, the background consists of  $b\bar{b}\nu_l \bar{\nu}_l$ ,  $q\bar{q}\nu_l \bar{\nu}_l$  ( $q \neq b$ ),  $q\bar{q}\nu_l l$ ,  $q\bar{q}l^-l^+$ ,  $q\bar{q}q\bar{q}$  and  $q\bar{q}$  events. The corresponding event samples are available on the DESY grid for the discussed polarisation states. We use samples for  $\sqrt{s} = 250$  GeV, generated and reconstructed using the detector model ILD\_00. Each DST data sample has to be scaled to an integrated luminosity of  $\mathcal{L} = 250 \text{ fb}^{-1}$  and a beam polarisation of  $P(e^+e^-) = (0.3, -0.8)$ . The numbers of all relevant background events are listed in tab. 5.4. As it will become clear in the following chapter, the large Higgs-strahlung contribution, as well as the severe background environment at  $\sqrt{s} = 250$  GeV can make it challenging to find WW-fusion events.

$m_H$ [GeV]	$N(\nu_l \bar{\nu}_l H)$	$N(\nu_e \bar{\nu}_e H)$	$N(\nu_l \bar{\nu}_l b\bar{b})$	$N(\nu_e \bar{\nu}_e b\bar{b})$
120	20 430	10 166	13 870	6 902
126	17 428	8 218	11 831	5 517
130	17 203	8 098	11 679	5 498
140	12 771	6 206	8 671	4 213

Table 5.1: Number of events in the  $\nu_l \bar{\nu}_l H$  signal samples and a rough estimation of event numbers expected for the  $\nu_e \bar{\nu}_e H$ ,  $\nu_l \bar{\nu}_l b\bar{b}$  and  $\nu_e \bar{\nu}_e b\bar{b}$  final state at  $\sqrt{s} = 250$  GeV,  $\mathcal{L} = 250$  fb $^{-1}$  and  $P(e^+ e^-) = (0.3, -0.8)$ .

$m_H$ [GeV]	$\sigma(e^+ e^- \rightarrow \nu_e \bar{\nu}_e H)$ [fb]	$N(\nu_e \bar{\nu}_e H)$	$\sigma(\nu_e \bar{\nu}_e H \rightarrow \nu_e \bar{\nu}_e b\bar{b})$ [fb]	$N(\nu_e \bar{\nu}_e b\bar{b})$
120	18.08	4 520	12.26	3 065
126	13.71	3 426	9.30	2 325
130	13.37	3 343	9.06	2 266
140	9.59	2 398	6.50	1 626

Table 5.2: Rough estimation of the event numbers expected for WW-fusion with  $H \rightarrow b\bar{b}$  at  $\sqrt{s} = 250$  GeV,  $\mathcal{L} = 250$  fb $^{-1}$  and  $P(e^+ e^-) = (0.3, -0.8)$ .

$m_H$ [GeV]	$\sigma(e^+ e^- \rightarrow \nu_l \bar{\nu}_l H)$ [fb]	$N(\nu_l \bar{\nu}_l H)$	$N(\nu_e \bar{\nu}_e H)$	$N(\nu_l \bar{\nu}_l b\bar{b})$	$N(\nu_e \bar{\nu}_e b\bar{b})$
120	64.08	16 019	5 754	10 876	3 908
126	56.01	14 002	4 702	9 506	3 192
130	54.61	13 653	4 548	9 257	3 088
140	39.39	9 345	3 280	6 344	2 228

Table 5.3: Event numbers expected for Higgs-strahlung with  $H \rightarrow b\bar{b}$  at  $\sqrt{s} = 250$  GeV,  $\mathcal{L} = 250$  fb $^{-1}$  and  $P(e^+ e^-) = (0.3, -0.8)$ .

$e^+ e^- \rightarrow$	$\nu_l \bar{\nu}_l b\bar{b}$	$\nu_l \bar{\nu}_l q\bar{q}$	$q\bar{q} l^+ l^-$	$q\bar{q} l\nu_l$	$q\bar{q} q\bar{q}$	$q\bar{q}$
event number	30 562	119 296	299 741	1 730 574	3 908 020	$26.016 \cdot 10^6$

Table 5.4: Background samples corresponding to an integrated luminosity  $\mathcal{L} = 250$  fb $^{-1}$  and a beam polarisation  $P(e^+ e^-) = (0.3, -0.8)$  at  $\sqrt{s} = 250$  GeV.



## Chapter 6

# Measurement of the Total Higgs Decay Width

For the simulation of the measurement of  $\Gamma_H^{\text{tot}}$  we take the Higgs mass to be 120 GeV, 126 GeV, 130 GeV and 140 GeV along with a centre of mass energy of 250 GeV and an integrated luminosity of  $250 \text{ fb}^{-1}$ . The beam polarisation is set to be  $P(e^+e^-) = (0.3, -0.8)$ . In the low Higgs mass range  $\Gamma_H^{\text{tot}}$  can be determined indirectly by measuring the coupling  $g_{\text{HWW}}$ . The coupling  $g_{\text{HWW}}$  describes the decay of the Higgs boson into two W-bosons as well as the WW-fusion process (fig. 6.1).

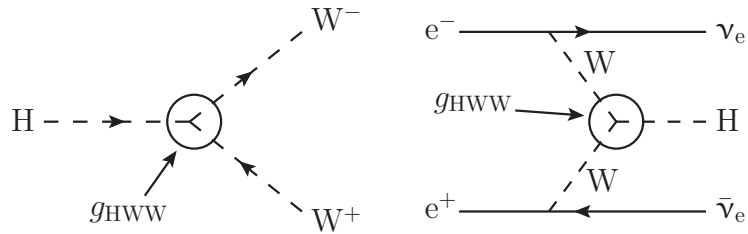


Figure 6.1: Higgs-decay into two W-bosons (l.) and the WW-fusion process (r.).

Both the partial decay width and the cross section of the WW-fusion process can be expressed in terms of the coupling. The unknown coupling  $g_{\text{HWW}}$  relates to the partial decay width and the WW-fusion cross section as [15]

$$\Gamma_H(H \rightarrow WW) = \frac{g_{\text{HWW}}^2 m_H^3}{64\pi m_W^2} \left(1 - \frac{4m_W^2}{m_H^2} + \frac{12m_W^4}{m_H^4}\right) \left(1 - \frac{4m_W^2}{m_H^2}\right)^{\frac{1}{2}}, \quad (6.1)$$

$$\sigma(\text{WW-fusion}) \rightarrow \frac{g_{\text{HWW}}^2 G_F^2}{32\pi^3} \left[ \left(1 + \frac{m_H^2}{s}\right) \log \frac{s}{m_H^2} - 2 \left(1 - \frac{m_H^2}{s}\right) \right]. \quad (6.2)$$

The proportionality following from eq. 6.1 and eq. 6.2

$$\Gamma_H(H \rightarrow WW) \propto g_{HWW}^2 \propto \sigma(WW\text{-fusion}), \quad (6.3)$$

can be used for the indirect determination of  $\Gamma_H^{\text{tot}}$ . The measurement of  $\sigma(WW\text{-fusion})$  can be transformed into a measurement of the partial decay width and thus into a measurement of the total decay width - almost free of model assumptions [37]. With eq. 6.3, the relation between total and partial decay width can be expressed as

$$\Gamma_H^{\text{tot}} = \frac{\Gamma_H(H \rightarrow WW)}{BR(H \rightarrow WW)} \longrightarrow \Gamma_H^{\text{tot}} \propto \frac{\sigma(WW\text{-fusion})}{BR(H \rightarrow WW)}. \quad (6.4)$$

A slight model-dependence is introduced due to the use of  $BR(H \rightarrow WW)$ , which can be measured independently.

In the analysis, the WW-fusion process with a Higgs decaying into two b-quarks provides us the direct measurement of the coupling  $g_{HWW}$ . By determining the cross section of the WW-fusion process via

$$\sigma(WW\text{-fusion}) = \frac{\sigma_{\text{fus}}(H \rightarrow b\bar{b})}{BR(H \rightarrow b\bar{b})} = \frac{N_{WW}}{\mathcal{L} \cdot BR(H \rightarrow b\bar{b})}, \quad (6.5)$$

where  $N_{WW}$  is the number of WW-fusion events, we can determine the partial decay width (cf. eq. 6.4) and finally  $\Gamma_H^{\text{tot}}$  [14].

The performed analysis works as follows: First of all, we try to remove as much of the background contribution as possible while retaining as much of the signal as possible. Therefore we apply various selection cuts. Unfortunately, some WW-fusion events are removed in the selection as well. The efficiency  $\epsilon$ , with which WW-fusion events pass the event selection is defined as

$$\epsilon = \frac{N'_{WW}}{N_{WW}}, \quad (6.6)$$

where  $N_{WW}$  and  $N'_{WW}$  are the number of WW-fusion events before and after the selection, respectively. The second step is the determination of  $\sigma(WW\text{-fusion})$ . We cannot completely remove the background contribution during the event selection. The remaining contributions to the  $\nu\bar{\nu}b\bar{b}$  final state from WW-fusion, Higgs-strahlung and background can be separated by exploiting their different characteristics in the spectrum of the  $\nu\bar{\nu}$  invariant mass, which is measurable through the missing mass distribution. Therefore we use a  $\chi^2$ -fit on the missing mass distribution of the remaining background  $N'_{\text{bgnd}}$ , WW-fusion  $N'_{WW}$  and Higgs-strahlung  $N'_{ZH}$  events, in order to extract the number of WW-fusion events that have passed the selection cuts. By knowing  $N'_{WW}$  we can determine the measurement accuracies of the total WW-fusion cross section (modify eq. 6.5 with eq. 6.6). The third and final step is the determination of the measurement accuracies of  $\Gamma_H^{\text{tot}}$ .

## 6.1 Event Selection

We start the simulation of the measurement by removing the background contribution from the events. The goal is to select WW-fusion events, which consist of missing four-momentum and two b-jets, and to remove as much of the background contribution as possible. We have generated a signal sample that includes all events with final state  $\nu_1\bar{\nu}_1H$ . As already discussed in section 2.2.2, the preferred decay mode of the Higgs boson is into two b-quarks. We expect most of the events in the signal sample to be  $\nu_1\bar{\nu}_1b\bar{b}$  final states. Additionally, we have generated WW-fusion and Higgs-strahlung samples to observe the interference term in comparison to the total  $\nu_1\bar{\nu}_1H$  sample during the event selection. The most important backgrounds in this channel are two-fermion events, Z-pairs decaying to neutrinos and hadrons, and W-pairs, where one W decays hadronically and the other W decays into a neutrino and a lepton which escapes undetected. The number of events before the event selection is listed in tab. 6.1.

	$m_H = 120 \text{ GeV}$	$m_H = 126 \text{ GeV}$	$m_H = 130 \text{ GeV}$	$m_H = 140 \text{ GeV}$
$N_{WW}$	4 525	3 426	3 343	2 398
$N_{ZH}$	16 019	14 002	13 653	9 345
$N_{\text{bgd}}^{\text{tot}}$	$32.104 \cdot 10^6$			

Table 6.1: Number of Higgs-strahlung, WW-fusion and background events before the event selection. The interference term is small, so it is not listed here.

We start the analysis by forcing the events into two jets. All reconstructed particles are clustered into two jets which are assumed to come from the Higgs-decay  $H \rightarrow b\bar{b}$ . The selection of signal events is performed in three stages. The first step involves two pre-cuts, using the number of charged tracks and the removal of isolated leptons in the events. The second step involves cuts on kinematic variables, followed by the third step which contains more event specific cuts, such as a b-tag for example, in order to select the desired  $\nu_e\bar{\nu}_e b\bar{b}$  state originating from WW-fusion. As an example, we always display the background and signal histograms with the corresponding cut regions for  $m_H = 120 \text{ GeV}$  before cuts. The corresponding histograms after cuts and the histograms for the other three Higgs masses before and after cuts can be found in the appendix of this thesis.

We start reducing the background with a cut on the number of charged tracks,  $N_{\text{ctrk}}$ . The multiplicity of the signal events is not very high. On the average every b-quark hadronises into less than ten hadrons. Background events can contain much more particles, for example originating from hadronic decays of W- and Z-pairs. We ask for at least ten charged tracks to certainly exclude purely leptonic final states. We keep every event in the

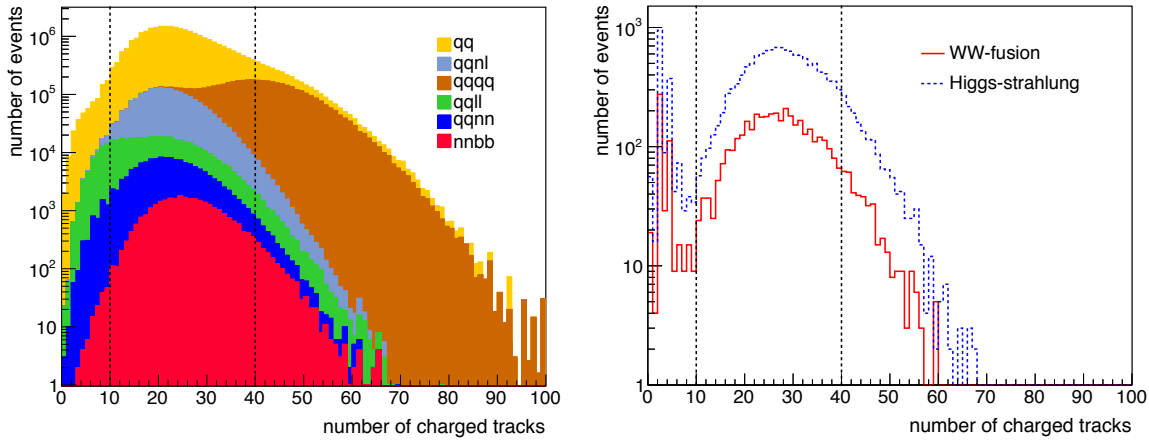


Figure 6.2: Number of charged tracks for  $m_H = 120$  GeV of the background (stacked, left) and the signal (overlaid, right) before a cut is applied.

interval

$$10 \leq N_{\text{ctrk}} \leq 40. \quad (6.7)$$

The number of charged tracks of the background and the signal for  $m_H = 120$  GeV is depicted in fig. 6.2. The distribution of the signal displays the WW-fusion and Higgs-strahlung contribution in the  $\nu_l \bar{\nu}_l H$  sample. It is evident that the lower threshold helps to remove mainly  $q\bar{q}l^+l^-$  and  $q\bar{q}$  events. The upper cut removes  $q\bar{q}q\bar{q}$  and  $q\bar{q}$  background. Quark-antiquark pairs are characterised by high multiplicity. In case of  $m_H = 120$  GeV, this cut helps to reduce Higgs-strahlung (fig. A.1).

Our signal consists of missing four-momentum and two b-jets. Since the neutrino mode is selected, we have events with no leptons. If there are leptons in the signal, they appear in the jets at most. Therefore we remove events with isolated leptons. This selection cut does not have any effect on the events in the signal sample. Leptons are defined as isolated if they have a transverse momentum of  $p_T > 5$  GeV and no other particle nearby within a half opening angle of  $25^\circ$  [37]. Backgrounds which contain leptons like  $q\bar{q}l^+l^-$  and  $q\bar{q}l\nu_l$  can be further reduced by applying this cut.

We continue the event selection by performing a selection cut on the visible invariant mass  $m_{\text{vis}}$ . The invariant mass of the visible four-momentum  $p_{\text{vis}}$  is defined as

$$m_{\text{vis}} = \sqrt{E_{\text{vis}}^2 - |\mathbf{p}_{\text{vis}}|^2}. \quad (6.8)$$

The visible mass distribution of the background and the signal for  $m_H = 120$  GeV is illustrated in fig. 6.3. The visible invariant mass  $m_{\text{vis}}$  should be consistent with  $m_H$ . As we can see in fig. 6.3, the distribution of the signal indeed shows a resonance at  $m_{\text{vis}} = m_H$ . The distribution to lower masses is due to ISR photon emission. ISR decreases the centre of mass energy  $\sqrt{s}$  that is used for this calculation [37]. We apply the visible mass cut

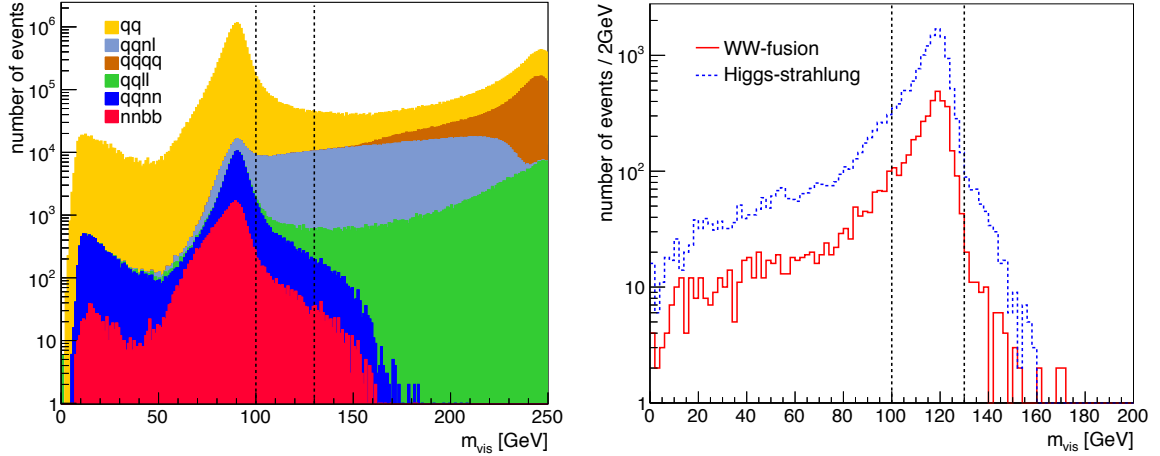


Figure 6.3: Visible mass distribution for  $m_H = 120$  GeV of the background (stacked, left) and the signal (overlaid, right) before a cut is applied.

$$m_H - 20 \text{ GeV} \leq m_{\text{vis}} \leq m_H + 10 \text{ GeV} \quad (6.9)$$

on every Higgs mass distribution. The histogram after every cut except from  $m_{\text{vis}}$  can be found in the appendix (fig. A.1). Evidently this cut is very successful in background reduction. In particular, the selection cut has a great effect on the  $q\bar{q}$  background, where the incoming leptons annihilate into a virtual  $Z$  or  $\gamma$ , which then decays into two fermions. ISR photons, which are preferably emitted in beam-pipe direction and might escape detection faking missing energy, can bring the invariant visible mass of the two-fermion system back to  $m_{\text{vis}} \approx m_Z$ . Even though the invariant mass of the two-fermion background peaks at  $m_Z$ , the tail of the visible mass distribution is still large enough to make this process one of the dominant backgrounds after this cut. Additionally, background processes coming from W- or Z-boson pairs are well rejected. For higher Higgs masses, the signal peak at  $m_H$  and the background peak at  $m_{\text{vis}} \approx m_Z$  in the corresponding distribution are further separated. Hence, the separation of the signal and the background is much better for higher Higgs masses.

The visible energy  $E_{\text{vis}}$  is defined as the sum of energies of all reconstructed particles in the event,

$$E_{\text{vis}} = \sum_i E_i. \quad (6.10)$$

The distribution of the visible energy of the signal and the background for  $m_H = 120$  GeV before a selection cut is applied is depicted in fig. 6.4. There are three peaks in the visible energy distribution of the background. The first peak at  $E_{\text{vis}} \sim m_Z$  is due to mainly  $q\bar{q}$  background, since the energy of photons resulting from radiative returns to the  $Z$ -peak is expected to be at around  $\sqrt{s} = m_Z$ . The second peak is at about  $E_{\text{vis}} \sim \frac{\sqrt{s}}{2} = 125$  GeV. The main contribution to this peak are events in which one of the colliding leptons loses

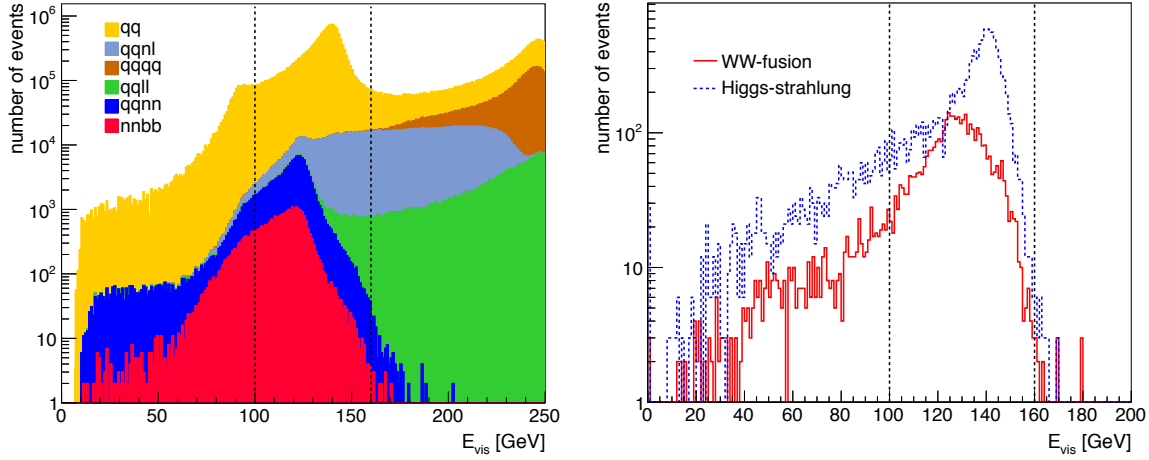


Figure 6.4: Visible energy distribution for  $m_H = 120$  GeV of the background (stacked, left) and the signal (overlaid, right) before a cut is applied.

most of its energy via ISR. The third peak at full centre of mass energy corresponds to events, in which all particles are detected. We now apply a cut on the visible energy and select events which fulfil

$$100 \text{ GeV} \leq E_{\text{vis}} \leq 160 \text{ GeV}. \quad (6.11)$$

This selection cut does not remove the background much further (fig. A.2), in particular only  $q\bar{q}$  background is affected. We slightly change the cut range for the other three Higgs masses. For  $m_H = 126$  GeV we apply the cut

$$105 \text{ GeV} \leq E_{\text{vis}} \leq 160 \text{ GeV} \quad (6.12)$$

and for  $m_H = 130$  GeV we keep all events within

$$110 \text{ GeV} \leq E_{\text{vis}} \leq 160 \text{ GeV}. \quad (6.13)$$

In case of  $m_H = 140$  GeV we change the cut to

$$125 \text{ GeV} \leq E_{\text{vis}} \leq 170 \text{ GeV}. \quad (6.14)$$

Now we proceed by applying a cut on the total transverse momentum of all reconstructed particles  $\sum p_T$ . In contrast to  $m_H = 120$  GeV, for higher Higgs masses the distribution of the total transverse momentum of Higgs-strahlung moves to lower  $\sum p_T$ , while the WW-fusion distribution always remains unchanged. At high  $\sum p_T$  we have more WW-fusion events than Higgs-strahlung events. Therefore, we apply the following cut,

$$20 \text{ GeV} \leq \sum p_T \leq 80 \text{ GeV}. \quad (6.15)$$

A change of the upper threshold to lower  $\sum p_T$  has no effect on the number of remaining background events. The background and signal distributions are illustrated in fig. 6.5 for

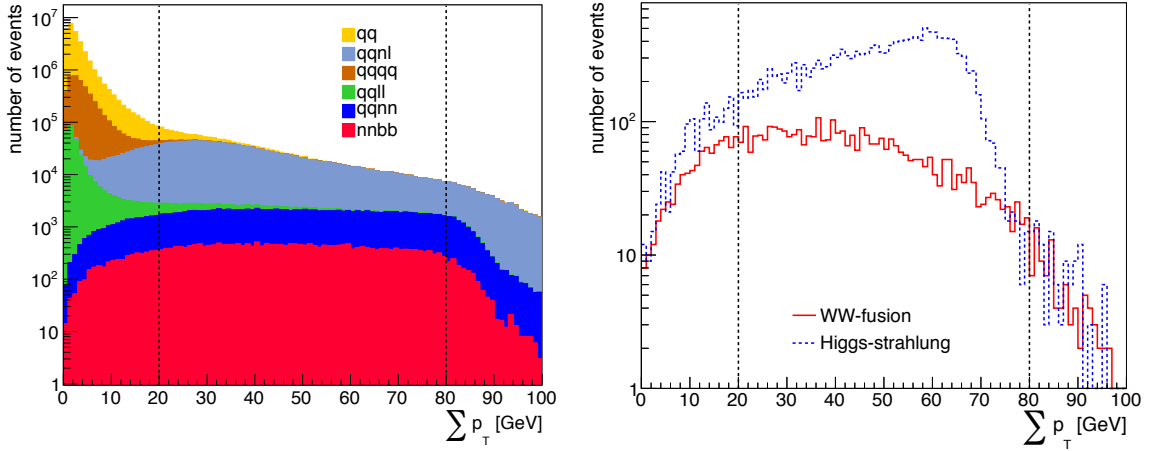


Figure 6.5: Total transverse momentum for  $m_H = 120$  GeV of the background (stacked, left) and the signal (overlaid, right) before a cut is applied.

$m_H = 120$  GeV. Due to momentum conservation the visible transverse momentum is equal to the invisible transverse momentum, but has opposite sign. Missing transverse momentum of backgrounds without neutrinos,  $q\bar{q}l^+l^-$ ,  $q\bar{q}q\bar{q}$  and  $q\bar{q}$ , is due to particles that stay undetected. As a result those backgrounds mainly consist of events with low total transverse momentum. In case of the  $q\bar{q}$  background, ISR photons are emitted at low polar angles. Generally, quarks tend to be produced in forward direction. So in both cases particles can stay undetected causing low transverse momentum. Similarly, in W- and Z-pair production decay products are produced back-to-back, thus resulting in low transverse momentum. The cut on the total transverse momentum reduces backgrounds without neutrinos in the final state and especially the main  $q\bar{q}$  background (fig. A.2).

Each b-quark decays into a complex shower of many elementary particles referred to as jets. Each jet consists of many tracks which are clustered according to an algorithm called *clustering algorithm*. We have started the analysis by forcing the events into two jets using the so-called *Durham algorithm* [41]. The Durham algorithm offers two variables, the Durham parameters  $Y_{23}$  and  $Y_{12}$ . With both parameters we can achieve a discrimination between the signal and backgrounds with different numbers of jets. The first selection cut is based on  $Y_{23}$ , which is the threshold value to reconstruct two jets as three jets. Thus, a cut on  $Y_{23}$  reduces background events that are misidentified as two-jet events. It especially helps to fully exclude hadronic W-pair and Z-pair production events which are four-jet events misidentified as two-jet events. In fig. 6.6 we can see the  $Y_{23}$  distribution of the background and the signal for  $m_H = 120$  GeV before a selection cut is applied. We choose to keep events with

$$Y_{23} \leq 0.02 \quad (6.16)$$

for all four Higgs masses. Below this value we assume to have only two-jet events. This cut helps to reduce background effectively.

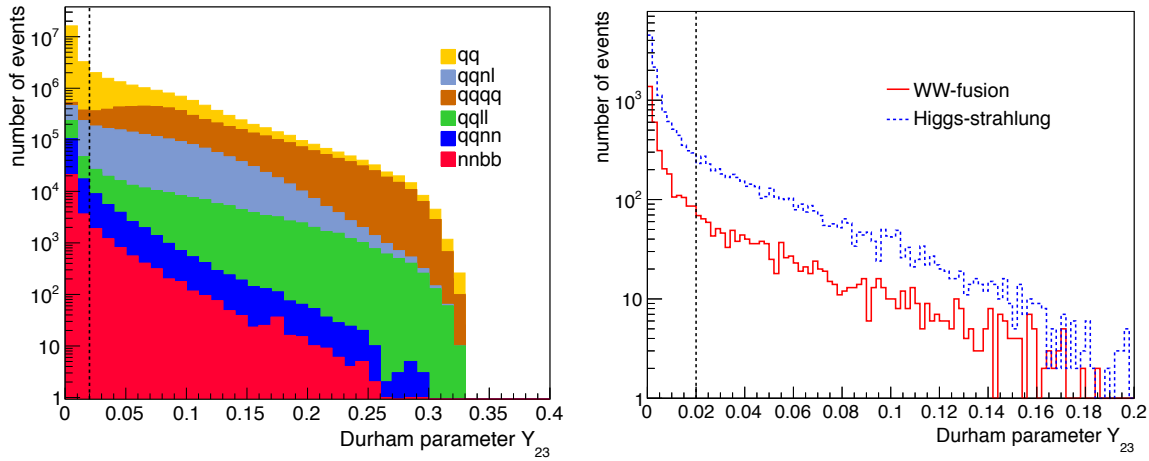


Figure 6.6: Durham parameter  $Y_{23}$  for  $m_H = 120$  GeV of the background (stacked, left) and the signal (overlaid, right) before a cut is applied.

Next to the cut on  $Y_{23}$ , the discrimination between the signal and backgrounds with different numbers of jets is further achieved by a selection cut on the second Durham parameter  $Y_{12}$ , which corresponds to the minimum  $Y$ -parameter for the two-jet hypothesis in the Durham algorithm. Therefore the next selection cut is based on  $Y_{12}$  at which the number of jets changes from two to one. We select events within the range

$$0.2 \leq Y_{12} \leq 0.8 \quad (6.17)$$

for all four Higgs masses. In this range we expect to have only two-jet events. In fig. 6.7 we illustrate the distribution of  $Y_{12}$  for signal and background for  $m_H = 120$  GeV. Background is not reduced much further after this cut (fig. A.3). However, for higher Higgs masses Higgs-strahlung moves to larger  $Y_{12}$ -values (fig. A.11, fig. A.20, fig. A.29). Thus, this cut helps to reduce Higgs-strahlung in case of higher  $m_H$ .

Since the production cross section of the total background is much larger than the production cross section of the signal, the identification of the b-jets is necessary to exclude background events and get a good signal-to-background ratio. This identification is called *b-tagging*. B-tagging is performed by using the *LCFIVertex flavour tagging package* [42], which is embedded in MARLIN. It is based on a neutral net approach, which combines track and vertex information to distinguish b-, c- and light jets. For each jet the routine returns a b-tag value, a number between 0 and 1 corresponding to b-jet likelihood. For b-jets we expect a peak at 1, and 0 for jets of the other flavours. For both jets, we require

$$\text{bttag} \geq 0.85. \quad (6.18)$$

In fig. 6.8 we can see the combined b-jet likelihood of the two jets of the background and the signal before a selection cut is applied. This cut helps to remove events in the signal

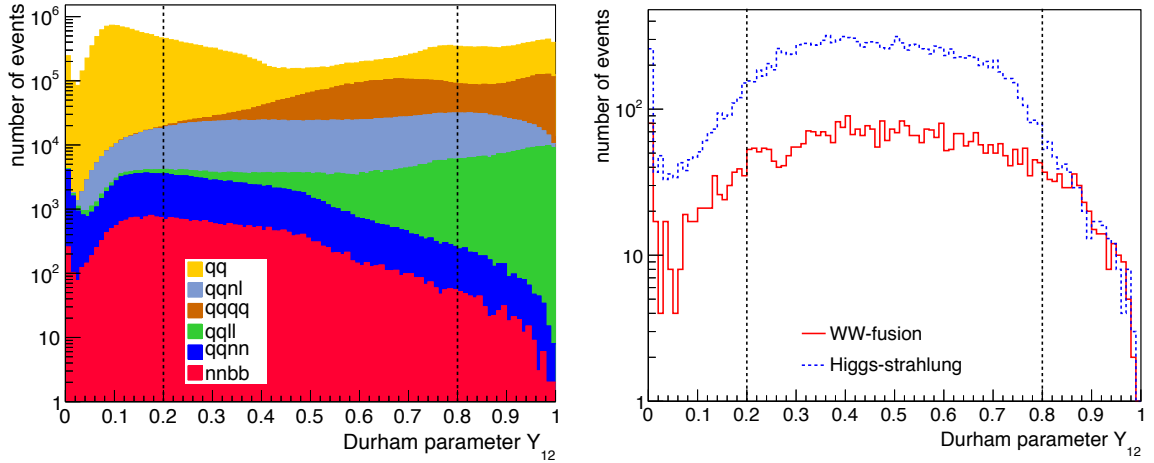


Figure 6.7: *Durham parameter  $Y_{12}$  for  $m_H = 120$  GeV of the background (stacked, left) and the signal (overlaid, right) before a cut is applied.*

sample that are not  $H \rightarrow b\bar{b}$  events. Evidently b-tagging is very effective in background reduction (fig. A.4). Due to the near absence of b-quarks in backgrounds originating from W-boson and Z-boson processes, backgrounds like  $q\bar{q}\nu_l\bar{\nu}_l$  and  $q\bar{q}l^+l^-$  are further reduced. The background sample  $q\bar{q}\nu_l\bar{\nu}_l$  does not contain any b-quarks at all, though some events remain after the b-tag. Some of the light quark jets are misidentified as b-jets. In general, for  $m_H = 126$  GeV, 130 GeV and 140 GeV we have less b-jet events in the signal sample since the branching ratio  $BR(H \rightarrow b\bar{b})$  decreases for larger Higgs masses. For  $m_H = 140$  GeV the branching ratio of  $H \rightarrow b\bar{b}$  is of the same order as the branching ratio of  $H \rightarrow WW$ .

After having performed a b-tag on the two jets in order to select the desired WW-fusion signal with final state  $\nu_e\bar{\nu}_e b\bar{b}$ , we now perform the next selection cut on another jet property. Since the W- and Z-boson in the corresponding backgrounds are relatively boosted, the total momentum in beam direction is larger as compared to WW-fusion and Higgs-strahlung events. In fig. 6.9 the background and signal distributions for  $m_H = 120$  GeV are depicted. The backgrounds  $q\bar{q}$ ,  $q\bar{q}\nu_l$ , and  $q\bar{q}q\bar{q}$  show the strongest distribution at large momenta. A selection cut on this variable helps to reduce these backgrounds. We keep events within the range

$$-60 \text{ GeV} \leq \sum p_z \leq 60 \text{ GeV}. \quad (6.19)$$

This cut is the same for all Higgs masses. It is very helpful to reduce the massive contribution of the two-fermion background.

As discussed before, some backgrounds in the analysis come from W-pair and Z-pair production processes. These productions happen predominantly via exchange reactions which lead to a strongly increasing differential cross section towards large absolute values

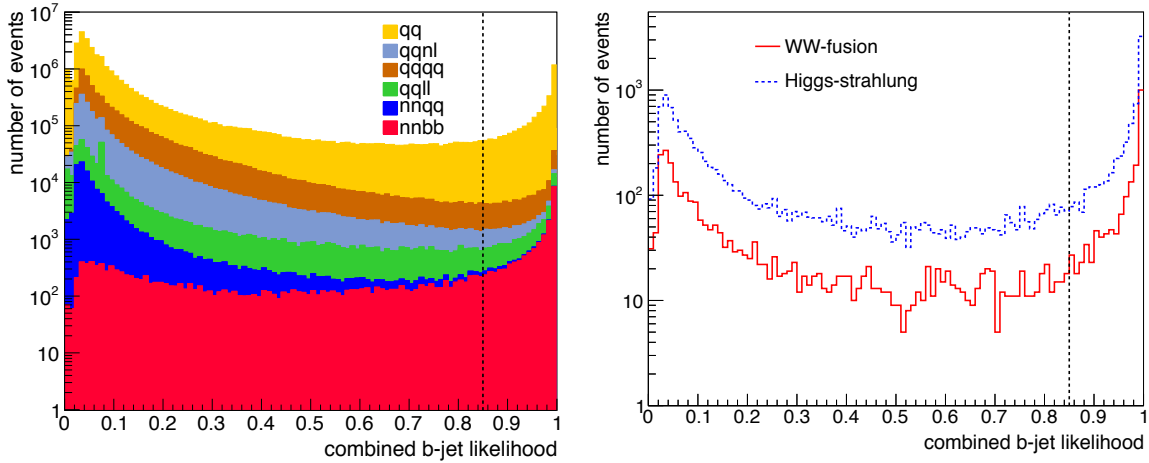


Figure 6.8: Combined  $b$ -jet likelihood for  $m_H = 120$  GeV of the background (stacked, left) and the signal (overlaid, right) before a cut is applied.

of the cosine of the polar angle [43]. Thus, the Z- and W-bosons are produced at small angles from the  $e^+e^-$ -beams and therefore the angular distribution of the processes have peaks in the forward and backward regions. On the contrary, Higgs-strahlung is expected to decrease towards the forward and backward direction. The  $\cos(\theta_{\text{jet}})$ -spectrum of the signal and background, as depicted in fig. 6.10 for  $m_H = 120$  GeV before cuts, is expected to discriminate between signal and background, especially background from W- and Z-pair production. We do not expect to remove Higgs-strahlung background [43]. For this reason, we require the angle of the reconstructed Higgs boson with respect to the beam axis to be

$$|\cos(\theta_{\text{jet}})| \leq 0.95. \quad (6.20)$$

As expected, background originating from W- and Z-boson pair production processes, especially  $l^+l^-q\bar{q}$ , can be further reduced by applying this selection cut.

In tab. 6.2 we see the different cuts and their effect on the signal sample  $\nu_1\bar{\nu}_1H$  divided into WW-fusion and Higgs-strahlung events for better visualisation for the four different Higgs masses. The efficiencies with which the WW-fusion and Higgs-strahlung events have passed the selection are listed in tab. 6.3. For  $m_H = 120$  GeV the selection cuts and their effect on each background sample that was used in the analysis are listed in tab. 6.4. In tab. 6.5, tab. 6.6 and tab. 6.7 we summarise the cutflow and the different background samples for  $m_H = 126$  GeV, 130 GeV and 140 GeV, respectively. Additionally, the total number of background events are listed. During the event selection, we always compare the total  $\nu_1\bar{\nu}_1H$  sample to the WW-fusion and Higgs-strahlung sample to observe the effects of the cuts on the interference term. After the selection the interference term is negligible. All histograms and tables in this study are therefore based on the WW-fusion and Higgs-strahlung samples.

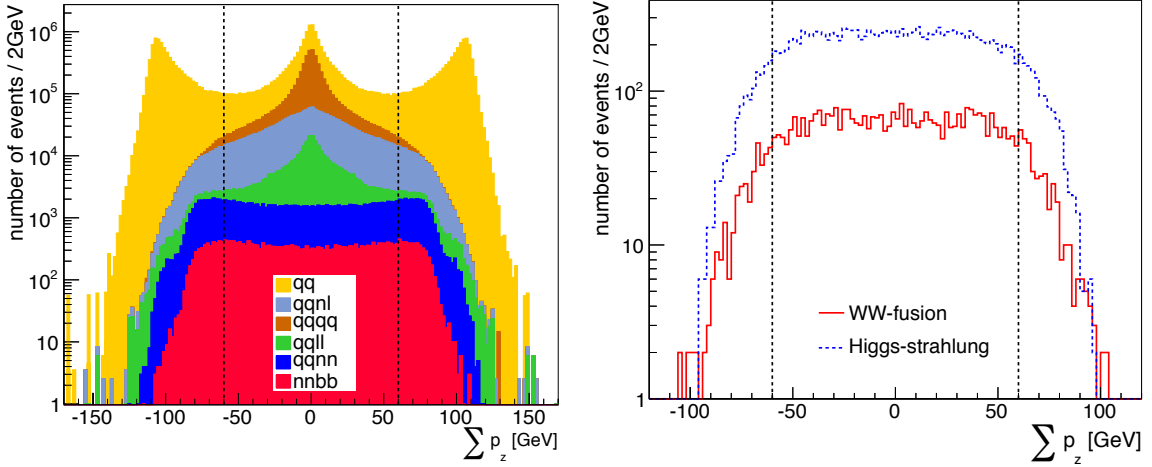


Figure 6.9: Total momentum in beam direction for  $m_H = 120$  GeV of the background (stacked, left) and the signal (overlaid, right) before a cut is applied.

Apparently, for  $m_H = 120$  GeV the contribution of  $\nu_l \bar{\nu}_l H$  events is larger than the total background contribution after the event selection. As expected, the Higgs-strahlung contribution in the signal sample is still larger than the WW-fusion contribution after the cuts. Next to Higgs-strahlung, the irreducible background  $\nu_l \bar{\nu}_l b\bar{b}$  gives the largest contribution to the background for  $m_H = 120$  GeV. The two-fermion background could be reduced from approximately  $26.016 \cdot 10^6$  events to roughly 133 events. However, the total background is still large after the selection.

This result is not surprising for the centre of mass energy and beam polarisation used in this analysis. At low centre of mass energies there is a very large background contribution, while additionally the Higgs-strahlung production cross section attains its maximum around  $\sqrt{s} = m_H + m_Z$ . Furthermore the beam polarisation  $P(e^+e^-) = (0.3, -0.8)$  increases the Higgs-strahlung contribution since the Z-boson couples to left- and right-handed particles, whereas the W-boson only couples to purely left-handed particles. Nevertheless, the W-boson background is suppressed by the choice of polarisation. We achieve the best signal-to-background ratio for  $m_H = 120$  GeV. The WW-fusion efficiency is larger than the efficiency for Higgs-strahlung events.

For each Higgs mass, Higgs-strahlung always gives a larger contribution compared to WW-fusion in the event sample. The Higgs-strahlung and WW-fusion distribution of the different cut parameters are most of the time of similar shape thus making the choice of cuts less effective for Higgs-strahlung events.

For higher Higgs masses we start with less signal events due to the decreasing branching ratio  $BR(H \rightarrow b\bar{b})$ . The variation of some selection cuts helps to reduce the background and to keep more WW-fusion events. Simultaneously, we can distinguish a bit better between Higgs-strahlung and WW-fusion for  $m_H = 126$  GeV, 130 GeV and 140 GeV. In the end there are much less WW-fusion and Higgs-strahlung events remaining for higher Higgs

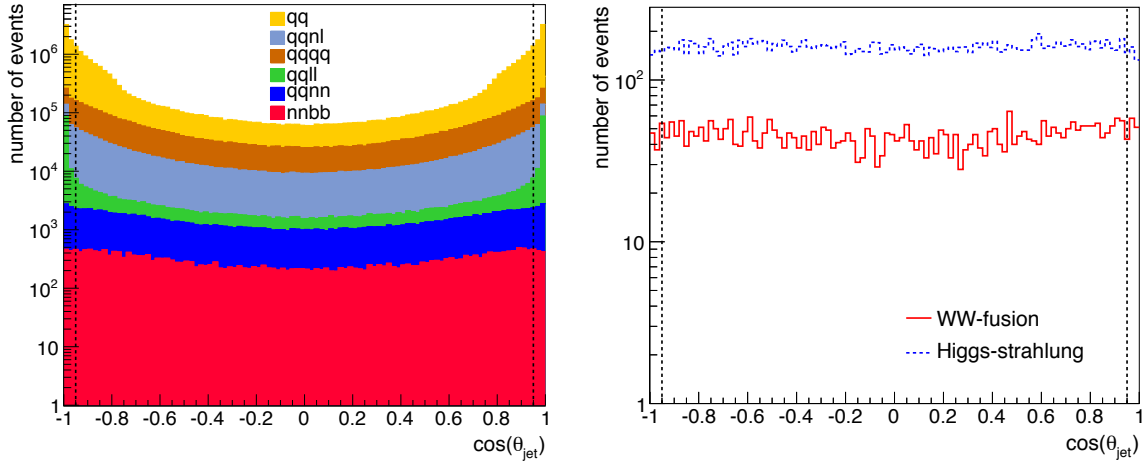


Figure 6.10: Angular distribution of the jets for  $m_H = 120$  GeV of the background (stacked, left) and the signal (overlaid, right) before a cut is applied.

masses and the efficiencies are small. For  $m_H = 120$  GeV we have the largest background contribution after the event selection. WW-fusion and Higgs-strahlung efficiency are of the same size. During the event selection, more cuts have been tested to further reduce the background, without the desired effect.

	$m_H = 120$ GeV		$m_H = 126$ GeV		$m_H = 130$ GeV		$m_H = 140$ GeV	
	$N_{WW}$	$N_{ZH}$	$N_{WW}$	$N_{ZH}$	$N_{WW}$	$N_{ZH}$	$N_{WW}$	$N_{ZH}$
no cut	4 525	16 019	3 426	14 002	3 343	13 653	2 398	9 345
$N_{ctrk}$	3 581	11 975	2 663	10 918	2 587	10 437	1 776	7 128
no isolated leptons	3 581	11 892	2 663	10 918	2 587	10 437	1 776	7 128
$m_{vis}$	2 899	8 058	2 07	8 356	1 892	7 494	1 124	4 416
$E_{vis}$	2 887	8 041	2 023	8 356	1 877	7 485	1 093	4 170
$\sum p_T$	2 596	7 391	1 577	7 448	1 535	6 909	897	3 669
$Y_{23}$	1 824	5 408	1 053	4 860	928	4 212	426	1 740
$Y_{12}$	1 778	5 260	965	4 594	848	3 894	377	1 431
btag	974	2 932	547	2 574	440	2 139	208	789
$ \sum p_z $	920	2 837	519	2 546	405	2 130	195	786
$ \cos(\theta_{jet}) $	898	2 767	507	2 546	401	2 079	190	759
number of events	898	2 767	507	2 546	401	2 079	190	759

Table 6.2: Cutflow and the number of WW-fusion and Higgs-strahlung events for the four different Higgs masses after every single cut.

$N(\nu_1 \bar{\nu}_1 H) \rightarrow N'(\nu_1 \bar{\nu}_1 b\bar{b})$			$N(\nu_1 \bar{\nu}_1 b\bar{b}) \rightarrow N'(\nu_1 \bar{\nu}_1 b\bar{b})$		
$m_H$	$\epsilon_{WW\text{-fusion}}$	$\epsilon_{Higgs\text{-strahlung}}$	$m_H$	$\epsilon_{WW\text{-fusion}}$	$\epsilon_{Higgs\text{-strahlung}}$
120 GeV	19.8 %	17.3 %	120 GeV	29.3 %	25.4 %
126 GeV	14.8 %	17.9 %	126 GeV	21.8 %	26.7 %
130 GeV	12.0 %	15.2 %	130 GeV	17.7 %	22.4 %
140 GeV	7.9 %	8.5 %	140 GeV	11.7 %	11.9 %

Table 6.3: Efficiency  $\epsilon$  of WW-fusion and Higgs-strahlung events for the four different Higgs masses.

	$N_{\text{bgd}}^{\text{tot}}$	$\nu_1 \bar{\nu}_1 b\bar{b}$	$\nu_1 \bar{\nu}_1 q\bar{q}$	$q\bar{q}l^+l^-$	$q\bar{q}lv$	$q\bar{q}q\bar{q}$	$q\bar{q}$
no cut	$32.104 \cdot 10^6$	30 562	119 296	299 741	1 730 574	3 908 020	$26.016 \cdot 10^6$
$10 < N_{\text{ctrk}} < 40$	$27.747 \cdot 10^6$	27 883	110 291	229 073	1 682 652	1 603 046	$23.821 \cdot 10^6$
no isolated leptons	$19.847 \cdot 10^6$	24 012	88 998	153 540	1 156 157	1 150 993	$17.274 \cdot 10^6$
$100 \text{ GeV} < m_{\text{vis}} < 130 \text{ GeV}$	1 396 258	1 513	8 601	5 496	171 555	591	1 208 502
$100 \text{ GeV} < E_{\text{vis}} < 160 \text{ GeV}$	1 023 459	1 507	8 571	4 198	144 193	372	864 618
$20 \text{ GeV} < \sum p_T < 80 \text{ GeV}$	113 211	1 203	6 977	1 207	102 225	7	1 592
$Y_{23} < 0.02$	28 682	706	4 386	470	21 836	0	1 284
$0.2 < Y_{12} < 0.8$	23 931	626	3 932	394	18 333	0	646
btag $> 0.85$	844	378	24	43	100	0	299
$ \sum p_z  < 60 \text{ GeV}$	553	308	14	32	65	0	134
$ \cos(\theta_{\text{jet}})  < 0.95$	534	298	14	32	57	0	133
number of events	534	298	14	32	57	0	133

Table 6.4: Cutflow and number of events for every background process for  $m_H = 120$  GeV. The total number of background events after every cut is listed.

	$N_{\text{bgd}}^{\text{tot}}$	$\nu_1 \bar{\nu}_1 b\bar{b}$	$\nu_1 \bar{\nu}_1 q\bar{q}$	$q\bar{q}l^+l^-$	$q\bar{q}lv$	$q\bar{q}q\bar{q}$	$q\bar{q}$
no cut	$32.104 \cdot 10^6$	30 562	119 296	299 741	1 730 574	3 908 020	$26.016 \cdot 10^6$
$10 < N_{\text{ctrk}} < 40$	$27.474 \cdot 10^6$	28 883	110 291	229 073	1 682 652	1 603 046	$23.821 \cdot 10^6$
no isolated leptons	$19.846 \cdot 10^6$	23 012	88 998	153 540	1 156 157	1 150 993	$17.274 \cdot 10^6$
$106 \text{ GeV} < m_{\text{vis}} < 136 \text{ GeV}$	1 047 860	1 040	5 548	6 196	181 973	782	852 321
$105 \text{ GeV} < E_{\text{vis}} < 160 \text{ GeV}$	985 320	1 040	5 545	5 922	177 193	728	794 892
$20 \text{ GeV} < \sum p_T < 80 \text{ GeV}$	142 909	878	4 714	1 760	134 047	3	1 507
$Y_{23} < 0.02$	27 271	421	2 408	588	22 654	1	1 199
$0.2 < Y_{12} < 0.8$	24 385	390	2 271	508	20 533	0	683
btag $> 0.85$	1 404	224	15	65	111	0	289
$ \sum p_z  < 60 \text{ GeV}$	465	193	9	38	73	0	152
$ \cos(\theta_{\text{jet}})  < 0.95$	449	187	9	36	65	0	152
number of events	449	187	9	36	65	0	152

Table 6.5: Cutflow and number of events for every background process for  $m_H = 126$  GeV. The total number of background events after every cut is listed.

	$N_{\text{bgrd}}^{\text{tot}}$	$\nu_1 \bar{\nu}_1 b\bar{b}$	$\nu_1 \bar{\nu}_1 q\bar{q}$	$q\bar{q} l^+ l^-$	$q\bar{q} l\nu$	$q\bar{q} q\bar{q}$	$q\bar{q}$
no cut	$32.104 \cdot 10^6$	30 562	119 296	299 741	1 730 574	3 908 020	$26.016 \cdot 10^6$
$10 < N_{\text{ctrk}} < 40$	$27.474 \cdot 10^6$	27 881	110 291	229 073	1 682 652	1 603 046	$23.821 \cdot 10^6$
no isolated leptons	$19.846 \cdot 10^6$	24 012	88 998	153 540	1 156 157	1 150 993	$17.274 \cdot 10^6$
$110 \text{ GeV} < m_{\text{vis}} < 140 \text{ GeV}$	1 012 320	837	4 560	6 538	189 123	961	810 301
$110 \text{ GeV} < E_{\text{vis}} < 160 \text{ GeV}$	886 064	834	4 557	6 012	177 915	850	695 896
$20 \text{ GeV} < \sum p_T < 80 \text{ GeV}$	147 341	689	3 930	2 007	139 381	6	1 328
$Y_{23} < 0.02$	25 447	278	1 806	561	21 802	1	999
$0.2 < Y_{12} < 0.8$	23 386	254	1 705	496	20 318	0	613
btag $> 0.85$	564	129	14	58	101	0	262
$ \sum p_z  < 60 \text{ GeV}$	382	115	10	36	69	0	152
$ \cos(\theta_{\text{jet}})  < 0.95$	366	109	10	34	61	0	152
number of events	366	109	10	34	61	0	152

Table 6.6: Cutflow and number of events for every background process for  $m_H = 130 \text{ GeV}$ . The total number of background events after every cut is listed.

	$N_{\text{bgrd}}^{\text{tot}}$	$\nu_1 \bar{\nu}_1 b\bar{b}$	$\nu_1 \bar{\nu}_1 q\bar{q}$	$q\bar{q} l^+ l^-$	$q\bar{q} l\nu$	$q\bar{q} q\bar{q}$	$q\bar{q}$
no cut	$32.104 \cdot 10^6$	30 562	119 296	299 741	1 730 574	3 908 020	$26.016 \cdot 10^6$
$10 < N_{\text{ctrk}} < 40$	$27.474 \cdot 10^6$	27 883	110 291	229 073	1 682 652	1 603 046	$23.821 \cdot 10^6$
no isolated leptons	$19.846 \cdot 10^6$	24 012	88 998	153 540	1 156 157	1 150 993	$17.274 \cdot 10^6$
$120 \text{ GeV} < m_{\text{vis}} < 150 \text{ GeV}$	884 034	496	2 773	7 744	206 139	1 635	665 247
$125 \text{ GeV} < E_{\text{vis}} < 170 \text{ GeV}$	847 580	465	2 651	7 354	201 547	1 590	633 973
$20 \text{ GeV} < \sum p_T < 80 \text{ GeV}$	170 047	365	2 216	2 678	163 329	59	1 400
$Y_{23} < 0.02$	27 242	123	830	464	24 811	1	1 013
$0.2 < Y_{12} < 0.8$	25 798	107	737	417	23 688	1	848
btag $> 0.85$	621	58	7	58	144	0	354
$ \sum p_z  < 60 \text{ GeV}$	448	57	7	38	111	0	235
$ \cos(\theta_{\text{jet}})  < 0.95$	433	56	7	36	99	0	235
number of events	433	56	7	36	99	0	235

Table 6.7: Cutflow and number of events for every background process for  $m_H = 140 \text{ GeV}$ . The total number of background events after every cut is listed.

## 6.2 Determination of the Cross Section $\sigma$ (WW-fusion)

We now continue with the determination of the WW-fusion cross section, which can be used to extract information on the coupling  $g_{HWW}$  of the Higgs boson to W-bosons, as well as to indirectly determine  $\Gamma_H^{\text{tot}}$ .

After the event selection, the dominant background to WW-fusion is represented by Higgs-strahlung. In order to determine  $\sigma(\text{WW-fusion})$  we need to extract the number of WW-fusion events  $N'_{\text{WW}}$  that have passed the event selection. The WW-fusion process with  $\nu\bar{\nu}b\bar{b}$  final state can be separated from the corresponding one in Higgs-strahlung by exploiting their different characteristics in the  $\nu\bar{\nu}$  invariant mass, which are measurable through the missing mass distribution. Therefore, we apply a  $\chi^2$ -fit on the shape of the missing mass distribution consisting of WW-fusion, Higgs-strahlung and background events after the selection. We use normalised Monte Carlo data as reference. The result of the fit yields the cross section  $\sigma_{\text{fus}}(H \rightarrow b\bar{b})$ , since only  $H \rightarrow b\bar{b}$  decays are selected. In order to determine the total WW-fusion cross section, eq. 6.5 has to be modified to

$$\sigma(\text{WW-fusion}) = \frac{N'_{\text{WW}}}{\epsilon \cdot \mathcal{L} \cdot BR(H \rightarrow b\bar{b})}. \quad (6.21)$$

The missing four-momentum is defined as the difference between  $\sqrt{s}$  and the sum  $p_{\text{vis}}$  of the four-momentum  $p_i = (E_i, \mathbf{p}_i)$  of every reconstructed particle:

$$p_{\text{vis}} = (E_{\text{vis}}, \mathbf{p}_{\text{vis}}) = \sum_i p_i, \quad p_{\text{mis}} = (\sqrt{s} - E_{\text{vis}}, -\mathbf{p}_{\text{vis}}), \quad (6.22)$$

$$m_{\text{mis}} = \sqrt{E_{\text{mis}}^2 - |\mathbf{p}_{\text{mis}}|^2}. \quad (6.23)$$

For each Higgs mass, the missing mass distribution of the signal and the background before cuts is depicted in fig. 6.11 to fig. 6.15.

In a  $\chi^2$ -fit, the function

$$\chi^2 = \sum_i^{N_{\text{bins}}} (N_i^{\text{pred}} - N_i^{\text{data}})^2 / \sigma^2(N_i^{\text{pred}}) \quad (6.24)$$

has to be minimised. Within ROOT we use the class *TMinuit* for this purpose. In eq. 6.24  $N_i^{\text{data}}$  is the number of data events in bin  $i$ , while  $N_i^{\text{pred}}$  is the number of predicted events in bin  $i$ . In order to fit on the missing mass distribution consisting of background, Higgs-strahlung and WW-fusion, we need to set up  $N_i^{\text{pred}}$  as a function of  $N'_{\text{WW}}$ ,  $N'_{\text{ZH}}$  and  $N'_{\text{brgd}}$ :

$$N_i^{\text{pred}} = N'_{\text{WW},i} + N'_{\text{ZH},i} + N'_{\text{brgd},i} + int_i, \quad (6.25)$$

where  $N'_{\text{WW},i}$ ,  $N'_{\text{ZH},i}$ ,  $N'_{\text{brgd},i}$  and  $int_i$  represent the number of events in bin  $i$  after the selection, respectively [37]. We do not fit on the interference term, it is taken to be fixed.

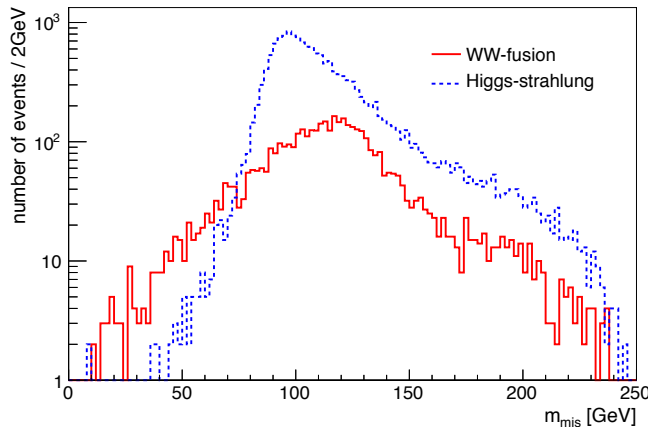


Figure 6.11: Missing mass distribution of WW-fusion and Higgs-strahlung for  $m_H = 120 \text{ GeV}$  before cuts.

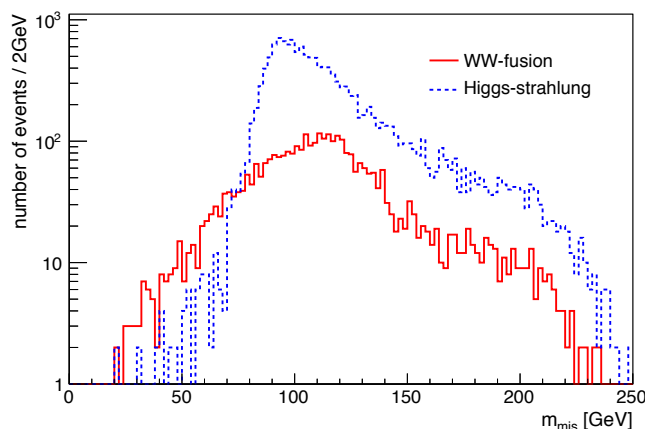


Figure 6.12: Missing mass distribution of WW-fusion and Higgs-strahlung for  $m_H = 126 \text{ GeV}$  before cuts.

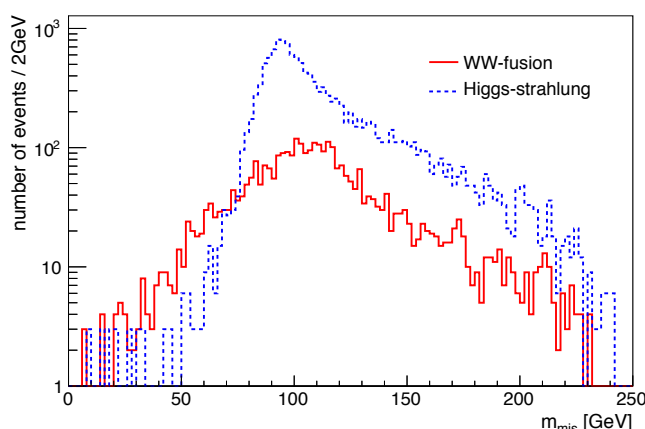


Figure 6.13: Missing mass distribution of WW-fusion and Higgs-strahlung for  $m_H = 130 \text{ GeV}$  before cuts.

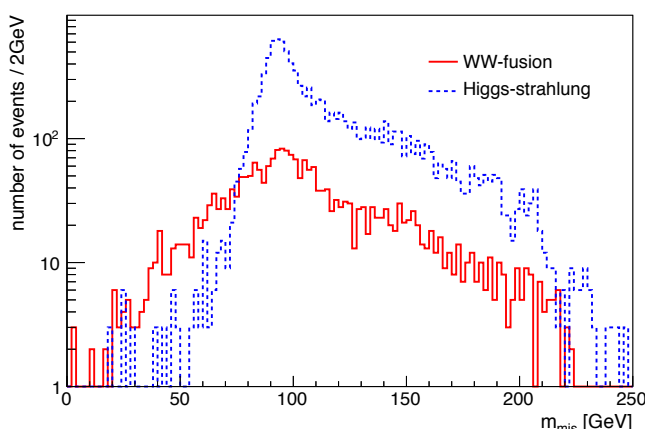


Figure 6.14: Missing mass distribution of WW-fusion and Higgs-strahlung for  $m_H = 140 \text{ GeV}$  before cuts.

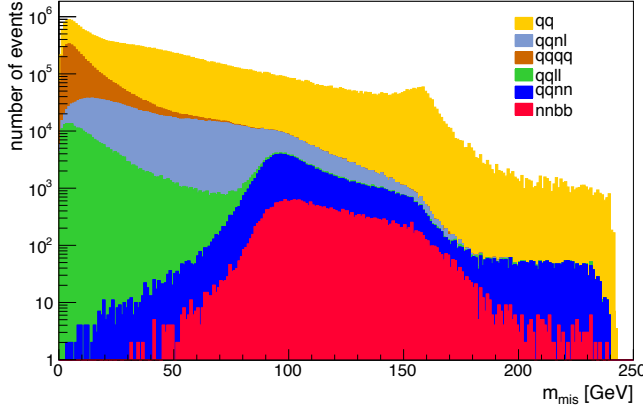


Figure 6.15: Missing mass distribution of the background before cuts at  $\sqrt{s} = 250$  GeV.

The missing mass spectrum for each Higgs mass after cuts, including the distribution of the simulated data is depicted in fig. 6.16 to fig. 6.19, respectively. We expected the shape of the missing mass distribution of Higgs-strahlung to peak at  $m_Z$ . The shape of the WW-fusion distribution is expected to peak at slightly larger missing masses for  $\sqrt{s} = 250$  GeV. In all four cases WW-fusion and Higgs-strahlung are as expected. For  $m_H = 126$  GeV, 130 GeV and 140 GeV, we have even less WW-fusion events compared to  $m_H = 120$  GeV, so the WW-fusion distribution flattens. The fit results are depicted in fig. 6.16 to fig. 6.19 as well. The results obtained from the fit are listed in tab. 6.8.

$m_H$ [GeV]	$N'_{WW} \pm \Delta N'_{WW}$	$N'_{ZH} \pm \Delta N'_{ZH}$	$N'_{bgd} \pm \Delta N'_{bgd}$
120	$873 \pm 58$	$2\,666 \pm 66$	$521 \pm 47$
126	$512 \pm 54$	$2\,497 \pm 85$	$454 \pm 46$
130	$407 \pm 46$	$1\,978 \pm 78$	$349 \pm 39$
140	$185 \pm 44$	$737 \pm 30$	$427 \pm 42$

Table 6.8: Number of WW-fusion, Higgs-strahlung and background events resulting from the  $\chi^2$ -fit for each of the four Higgs masses.

For larger Higgs masses the fit on  $N'_{WW}$  worsens. This can be explained by the decreasing branching ratio  $BR(H \rightarrow b\bar{b})$  (cf. fig. 2.6). Since we have already started with a small number of WW-fusion events and large Higgs-strahlung and background contributions, the number of WW-fusion and Higgs-strahlung events with  $\nu_e \bar{\nu}_e b\bar{b}$  final state decreases as the Higgs mass increases, and thus the fit on  $N'_{WW}$  worsens. For  $m_H = 140$  GeV, the branching ratio  $BR(H \rightarrow b\bar{b})$  is of the same order of  $BR(H \rightarrow WW)$  and the error of the fit on  $N'_{WW}$  is about 23.78% (tab. 6.9). The best fit result is achieved for  $m_H = 120$  GeV.

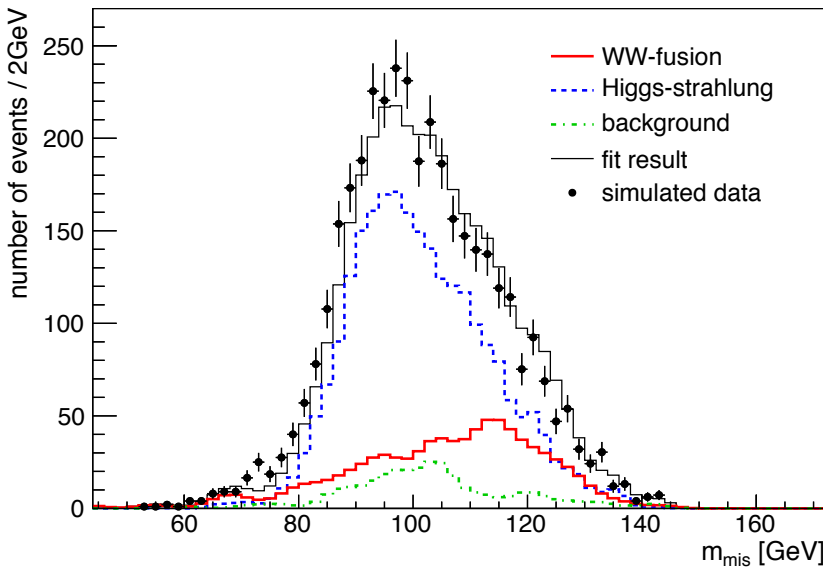


Figure 6.16: Missing mass distribution of WW-fusion, Higgs-strahlung and background for  $m_H = 120$  GeV after cuts, including the fit result.

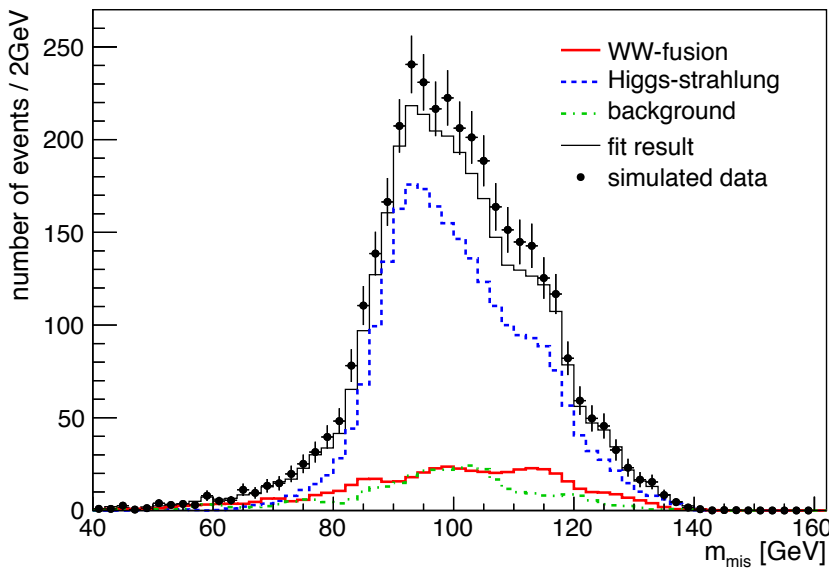


Figure 6.17: Missing mass distribution of WW-fusion, Higgs-strahlung and background for  $m_H = 126$  GeV after cuts, including the fit result.

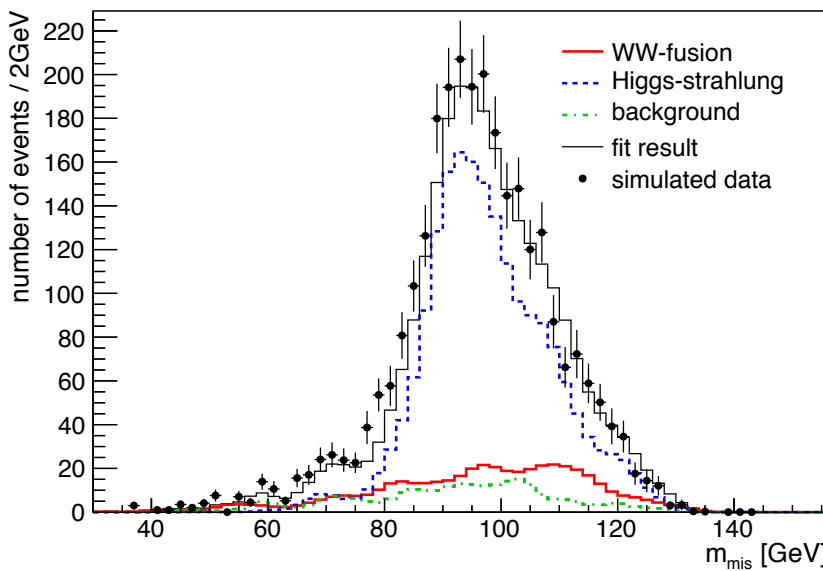


Figure 6.18: Missing mass distribution of WW-fusion, Higgs-strahlung and background for  $m_H = 130$  GeV after cuts, including the fit result.

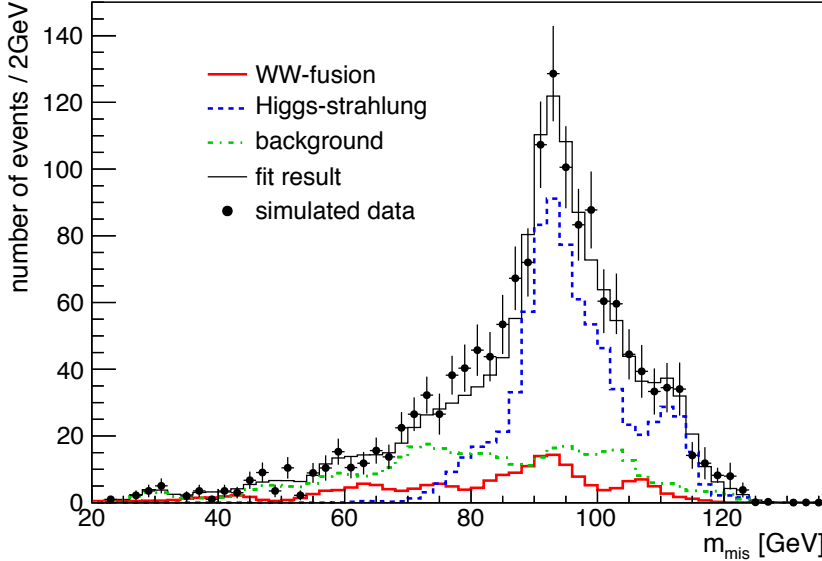


Figure 6.19: Missing mass distribution of WW-fusion, Higgs-strahlung and background for  $m_H = 140$  GeV after cuts, including the fit result.

The relative precision of the WW-fusion cross section measurement can be determined with [37]

$$\frac{\Delta\sigma(\text{WW-fusion})}{\sigma(\text{WW-fusion})} = \sqrt{\left(\frac{\Delta N'_{\text{WW}}}{N'_{\text{WW}}}\right)^2 + \left(\frac{\Delta BR(H \rightarrow b\bar{b})}{BR(H \rightarrow b\bar{b})}\right)^2}. \quad (6.26)$$

The uncertainty in the efficiency is considered negligible. Systematic effects of the luminosity are not considered in this analysis. The resulting measurement accuracies of the WW-fusion cross section for the four different Higgs masses are listed in tab. 6.9.

$m_H$ [GeV]	$\frac{\Delta N'_{\text{WW}}}{N'_{\text{WW}}}$	$\frac{\Delta N'_{\text{ZH}}}{N'_{\text{ZH}}}$	$\frac{\Delta BR(H \rightarrow b\bar{b})}{BR(H \rightarrow b\bar{b})}$	$\frac{\Delta\sigma(\text{WW-fusion})}{\sigma(\text{WW-fusion})}$
120	6.64 %	2.48 %	2.7 %	7.2 %
126	10.54 %	3.40 %	3.0 %	10.96 %
130	11.30 %	3.89 %	3.5 %	11.83 %
140	23.78 %	4.07 %	5.1 %	24.32 %

Table 6.9: Measurement accuracies of the WW-fusion cross section obtained in the low Higgs mass region at  $\sqrt{s} = 250$  GeV, assuming  $250 \text{ fb}^{-1}$  of data.

The determination of the total WW-fusion cross section relies on the measurement of the  $H \rightarrow b\bar{b}$  branching ratio. Since the branching ratio drops rapidly as the Higgs boson mass approaches the threshold for  $H \rightarrow WW$  (cf. fig. 2.6) the expected precision for the cross section measurement does as well. Taking into account the uncertainties from the fit and from the branching ratio measurement, the expected statistical precision of the WW-fusion cross section measurement varies from 7.2% to 24.32% for  $m_H = 120$  GeV to

$m_H = 140$  GeV. The errors of the fit are always larger than the measurement errors of  $BR(H \rightarrow b\bar{b})$ . The latter are taken from the corresponding recent study for ILC [44]: Among other things, the measurement accuracies are determined for a Higgs mass of  $m_H = 120$  GeV and  $m_H = 125$  GeV at a centre of mass energy of  $\sqrt{s} = 250$  GeV and an integrated luminosity of  $\mathcal{L} = 250$  fb $^{-1}$ , assuming  $P(e^+e^-) = (0.3, -0.8)$ . Considering 2011 LHC results, an estimation of the Higgs branching ratio measurement accuracies at the indicated Higgs mass region is given by extrapolating the  $m_H = 120$  GeV results. The entire analysis can be found in [44]. In this study, we take the accuracy obtained for  $m_H = 125$  GeV in our measurement for  $m_H = 126$  GeV.

The analysis has already been performed for the TESLA detector at higher centre of mass energies,  $\sqrt{s} = 500$  GeV and  $\sqrt{s} = 350$  GeV, assuming 500 fb $^{-1}$  of data [37]. It has shown that the accuracy of the fit on  $N'_{WW}$  improves at higher  $\sqrt{s}$ . At the same time, for larger  $m_H$  the signal-to-background ratio is less appealing since  $BR(H \rightarrow b\bar{b})$  decreases. At  $\sqrt{s} = 500$  GeV the WW-fusion cross section can be determined to an accuracy between 2.8% and 13.0% for  $m_H = 120$  GeV to  $m_H = 160$  GeV. At  $\sqrt{s} = 350$  GeV the results are slightly worse since the WW-fusion production cross section decreases to smaller  $\sqrt{s}$ , whereas the Higgs-strahlung cross section rises. In general, for  $m_H \leq 150$  GeV the measurement can be performed with slightly larger errors at  $\sqrt{s} = 350$  GeV, collecting 500 fb $^{-1}$  of data. For example, for  $m_H = 120$  GeV the WW-fusion cross section can be determined to a relative precision of 3.3%. The missing mass distribution for  $m_H = 120$  GeV at  $\sqrt{s} = 500$  GeV and  $\sqrt{s} = 350$  GeV, including the corresponding fit results, are illustrated in fig. 6.20. Both figures are taken from [37]. The distributions show the expected shapes: WW-fusion is wide and peaks at large missing masses and Higgs-strahlung peaks at  $m_Z$ . At  $\sqrt{s} = 500$  GeV the fit on  $N'_{WW}$  can be performed well, due to the dominant WW-fusion distribution in the missing mass spectrum at high  $\sqrt{s}$ . In case of  $\sqrt{s} = 350$  GeV, although the WW-fusion contribution is smaller and Higgs-strahlung larger compared to  $\sqrt{s} = 500$  GeV, the peaks of the WW-fusion and Higgs-strahlung spectrum are far enough separated to be distinguished and fitted on well.

Compared to these results, the outcome of our present study is expected for the following reasons: Compared to  $\sqrt{s} = 350$  GeV and  $\sqrt{s} = 500$  GeV we expected the peak of WW-fusion to lie between  $110$  GeV  $< m_{\text{mis}} < 120$  GeV. Furthermore, we have started with a small number of WW-fusion and a large number of Higgs-strahlung events, since WW-fusion is the dominant Higgs production process at high and Higgs-strahlung at low  $\sqrt{s}$ . Thus we have started the analysis on contrary terms. At  $\sqrt{s} = 350$  GeV, WW-fusion and Higgs-strahlung are of similar size, whereas at  $\sqrt{s} = 500$  GeV Higgs-strahlung after cuts is very small and WW-fusion is large.

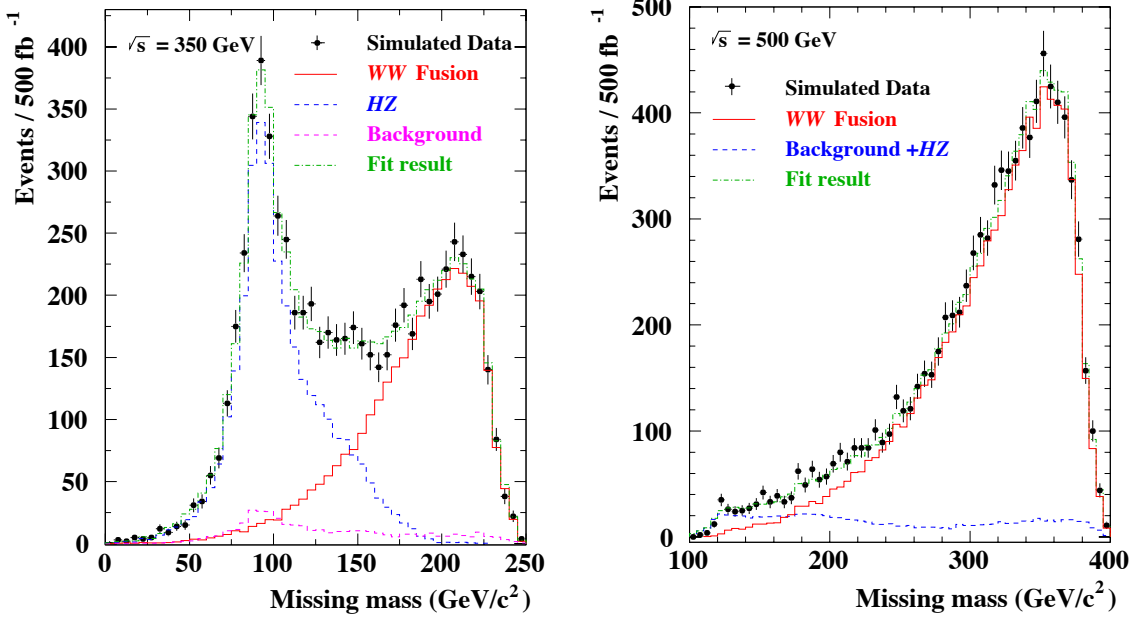


Figure 6.20: Missing mass distribution for  $m_H = 120 \text{ GeV}$  at  $\sqrt{s} = 350 \text{ GeV}$  (l.) and  $\sqrt{s} = 500 \text{ GeV}$  (r.) for TESLA. The figures are taken from [37].

### Estimation of the Measurement Accuracies of $\sigma$ (Higgs-strahlung)

The selection cuts are motivated by the selection of WW-fusion events. They are not based on the selection of Higgs-strahlung events. Nevertheless, the large Higgs-strahlung contribution at  $\sqrt{s} = 250 \text{ GeV}$  makes it possible for us to determine the number of Higgs-strahlung events after the event selection with better precision compared to WW-fusion. Thus, we can additionally extract information on the Higgs-strahlung cross section  $\sigma$ (Higgs-strahlung). For the sake of completeness, the measurement accuracies of the Higgs-strahlung cross section are listed in tab. 6.10.

$m_H \text{ [GeV]}$	$\frac{\Delta N'_{WW}}{N'_{WW}}$	$\frac{\Delta N'_{ZH}}{N'_{ZH}}$	$\frac{\Delta BR(H \rightarrow b\bar{b})}{BR(H \rightarrow bb)}$	$\frac{\Delta \sigma(\text{Higgs-strahlung})}{\sigma(\text{Higgs-strahlung})}$
120	6.64 %	2.48 %	2.7 %	3.66 %
120	10.54 %	3.4 %	3.0 %	4.53 %
130	11.3 %	3.89 %	3.5 %	5.2 %
140	23.78 %	4.07 %	5.1 %	6.52 %

Table 6.10: Measurement accuracies of the Higgs-strahlung cross section obtained for the low Higgs mass range at  $\sqrt{s} = 250 \text{ GeV}$ , assuming  $250 \text{ fb}^{-1}$  of data.

## Short Overview of the Coupling $g_{\text{HWW}}$ and $g_{\text{HZZ}}$

Next to the determination of  $\Gamma_{\text{H}}^{\text{tot}}$  which is performed in the following section, the measurement of the WW-fusion cross section can be used to extract information on the coupling  $g_{\text{HWW}}$ . The cross section for WW-fusion is at leading order and neglecting small interference terms, it only depends on the coupling. The WW-fusion cross section can be expressed as

$$\sigma(\text{WW-fusion}) = \frac{g_{\text{HWW}}^2 m_{\text{W}}^2}{32\pi^3} \int_{\kappa_{\text{H}}}^1 \int_x^1 \frac{dx dy}{[1 + (y - x)/\kappa_{\text{W}}]^2} f(x, y), \quad (6.27)$$

where  $f(x, y)$  is

$$f(x, y) = \left( \frac{2x}{y^3} - \frac{1+3x}{y^2} + \frac{2+x}{y} - 1 \right) \left[ \frac{z}{1+z} - \log(1+z) \right] + \frac{x}{y^3} \cdot \frac{z^2(1-y)}{1+z}, \quad (6.28)$$

with  $\kappa_{\text{H}} = m_{\text{H}}^2/s$ ,  $\kappa_{\text{W}} = m_{\text{W}}^2/s$  and  $z = y(x - \kappa_{\text{H}})/(\kappa_{\text{W}}x)$  [15]. Every parameter in  $f(x, y)$  is known or can be measured. Thus, the WW-fusion cross section provides direct access to  $g_{\text{HWW}}$ , which itself is predicted to be closely linked to the coupling  $g_{\text{HZZ}}$  through  $SU(2) \times U(1)$  symmetry ( $g_{\text{HWW}}/g_{\text{HZZ}} = 1/\cos(\theta_W)$ ). The comparison between  $g_{\text{HZZ}}$  and  $g_{\text{HWW}}$  couplings verify the  $SU(2) \times U(1)$  structure, which is essential to establish the Higgs mechanism. Once the  $SU(2) \times U(1)$  coupling is established, all channels are combined to precisely determine both  $g_{\text{HZZ}}$  and  $g_{\text{HWW}}$  couplings. The coupling to gauge bosons can be probed independently by different observables and best in the measurement of the production cross sections.

In case of  $g_{\text{HZZ}}$ , the Higgs-strahlung cross section  $\sigma(e^+e^- \rightarrow \text{HZ} \rightarrow \text{Hl}^+\text{l}^-)$  can be determined by analysing the recoil mass from  $Z \rightarrow \text{l}^-\text{l}^+$  against the Z-boson. Thus,  $g_{\text{HZZ}}$  can be determined independently of the Higgs decay modes, so no further model assumptions have to be made.

Since other determinations of couplings are partially correlated, it is interesting to perform a global fit to the measurable observables and to extract the Higgs couplings in a model-independent way. This method optimises the available information and can take properly into account the experimental correlation between different measurements [18].

### 6.3 Determination of the Total Decay Width of the Higgs Boson

As already mentioned,  $\Gamma_H^{\text{tot}}$  is predicted to be too narrow to be resolved experimentally for Higgs masses below the ZZ-threshold. Below this threshold indirect methods are applied which exploit the relation between the total and partial decay width for exclusive final states:  $\Gamma_H^{\text{tot}} = \Gamma_H(H \rightarrow X)/\text{BR}(H \rightarrow X)$ . Here, we extract  $\Gamma_H(H \rightarrow WW)$  from the measurement of the WW-fusion cross section combined with a measurement of  $\text{BR}(H \rightarrow WW)$ . The WW-fusion cross section and the partial decay width are equally proportional to  $g_{HWW}^2$  (cf. eq. 6.3). By determining the WW-fusion cross section we can extract information on  $g_{HWW}$  and determine  $\Gamma_H^{\text{tot}}$ . Due to the combined measurement of the branching ratio we get a small model-dependence.

#### Branching Ratio Measurement $\text{BR}(H \rightarrow WW)$

As already discussed, the measurement of  $\text{BR}(H \rightarrow WW)$  provides an alternative means to access  $g_{HWW}$ . This measurement combined with the determination of the Higgs-strahlung and WW-fusion cross sections can be used to extract the Higgs width with good accuracy.

The determination of  $\text{BR}(H \rightarrow WW)$  has been performed using the  $H \rightarrow WW \rightarrow \bar{v}lq\bar{q}$  channel [45]. The signal is characterised by the event topology and the two-jet recoil mass distribution peaking at the Higgs mass. By selecting the decay  $H \rightarrow WW \rightarrow \bar{v}lq\bar{q}$  for the low Higgs mass range ( $110 \text{ GeV} \leq m_H \leq 140 \text{ GeV}$ ) at  $\sqrt{s} = 350 \text{ GeV}$ , assuming  $500 \text{ fb}^{-1}$  of data, the decay mode covers 20.4% of all decays of ZH (with  $H \rightarrow WW$ ). The main background in the corresponding analysis consists of WW, ZZ and  $t\bar{t}$ , and backgrounds coming from processes with  $H \rightarrow X \neq WW$ . The selection cuts are constructed to reduce the specific types of background. After the event selection, which is discussed in detail in [45], the only important background remaining are W-boson pairs, which can be suppressed using a polarised  $e^-$ -beam. The achievable precision in the branching ratio measurement lies between 5.4% and 2.1% for Higgs boson masses between 120 GeV and 160 GeV. Since the analysis covers only 20% of these decay modes, there are several ways to improve the precision of the measurement of the branching ratio.

The independent measurement of  $\text{BR}(H \rightarrow WW)$ , as described above, is not performed in our analysis. The results are taken from the analysis in [45].

Furthermore, the measurement of  $\text{BR}(H \rightarrow WW)$  has been performed at  $\sqrt{s} = 250 \text{ GeV}$  for  $m_H = 120 \text{ GeV}$  and  $125 \text{ GeV}$  assuming  $250 \text{ fb}^{-1}$  of data and a polarisation  $P(e^+e^-) = (0.3, -0.8)$  in a recent study for ILC, obtaining larger errors in the measurement [44, 46].

The relation between the partial decay width and the coupling can be deduced from eq. 6.1. The total decay width can be determined with eq. 6.4, by exploiting the relation between partial and total decay width we can observe that the total decay width is proportional to the WW-fusion cross section divided by the branching ratio  $BR(H \rightarrow WW)$ . The relative precision of the measurement of  $\Gamma_H^{\text{tot}}$  can be determined with [37]

$$\frac{\Delta\Gamma_H^{\text{tot}}}{\Gamma_H^{\text{tot}}} = \sqrt{\left(\frac{\Delta\sigma(\text{WW-fusion})}{\sigma(\text{WW-fusion})}\right)^2 + \left(\frac{\Delta BR(H \rightarrow WW)}{BR(H \rightarrow WW)}\right)^2}. \quad (6.29)$$

The resulting measurement accuracies of  $\Gamma_H^{\text{tot}}$  for the four different Higgs masses are listed in tab. 6.11, taking the measurement accuracies of  $BR(H \rightarrow WW)$  from [45]. At  $\sqrt{s} = 250$  GeV,  $\Gamma_H^{\text{tot}}$  can be determined to an accuracy between 9.0% and 24.44% for Higgs masses between 120 GeV and 140 GeV. The improving accuracy in the measurement of  $BR(H \rightarrow WW)$  for larger  $m_H$  results from the increasing branching ratio of  $H \rightarrow WW$  as the Higgs mass increases. The resulting measurement accuracies of the Higgs decay width follow from the unfortunate outcome of the fits on the missing mass distribution, which have been discussed before. The errors in the cross section measurement are always dominant.

$m_H$ [GeV]	$\frac{\Delta N'_{WW}}{N'_{WW}}$	$\frac{\Delta\sigma(\text{WW-fusion})}{\sigma(\text{WW-fusion})}$	$\frac{\Delta BR(H \rightarrow WW)}{BR(H \rightarrow WW)}$	$\frac{\Delta\Gamma_H^{\text{tot}}}{\Gamma_H^{\text{tot}}}$
120	6.64 %	7.2 %	5.4 %	9.0 %
126	10.54 %	10.96 %	4.6 %*	11.88 %
130	11.3 %	11.83 %	3.3 %	12.28 %
140	23.78 %	24.32 %	2.5 %	24.44 %

Table 6.11: Measurement accuracies of the total decay width of the Higgs boson in the low Higgs mass region at  $\sqrt{s} = 250$  GeV. Value \* is extrapolated from the other results.

Taking the results from the other  $BR(H \rightarrow WW)$  measurement [46] which we have briefly mentioned before, we obtain larger errors:

for  $m_H = 120$  GeV, using  $\Delta BR(H \rightarrow WW)/BR(H \rightarrow WW) = 8.4\%$ , we obtain a relative precision of 11.06%. In case of  $m_H = 126$  GeV, using  $\Delta BR(H \rightarrow WW)/BR(H \rightarrow WW) = 7.2\%$ , an accuracy in the Higgs decay width measurement of 13.11 % can be achieved.

At  $\sqrt{s} = 500$  GeV the total decay width can be determined to a relative precision between 4.9% for  $m_H = 140$  GeV and 6.1% for  $m_H = 120$  GeV. In case of  $\sqrt{s} = 350$  GeV the measurement accuracies of  $\Gamma_H^{\text{tot}}$  vary between 6.3% and 5.1% for the same Higgs mass range. The results for  $\sqrt{s} = 350$  GeV and  $\sqrt{s} = 500$  GeV and the results obtained in our analysis are listed in tab. 6.12.

$m_H$ [GeV]	$\sqrt{s} = 250$ GeV		$\sqrt{s} = 350$ GeV		$\sqrt{s} = 500$ GeV	
	$\Delta\sigma(\text{WW})/\sigma(\text{WW})$	$\Delta\Gamma_H^{\text{tot}}/\Gamma_H^{\text{tot}}$	$\Delta\sigma(\text{WW})/\sigma(\text{WW})$	$\Delta\Gamma_H^{\text{tot}}/\Gamma_H^{\text{tot}}$	$\Delta\sigma(\text{WW})/\sigma(\text{WW})$	$\Delta\Gamma_H^{\text{tot}}/\Gamma_H^{\text{tot}}$
120	7.2 %	9.0 %	3.3 %	6.3 %	2.8 %	6.1 %
126	10.96 %	11.88 %	—	—	—	—
130	11.83 %	12.28 %	3.8 %	5.1 %	3.7 %	5.0 %
140	24.32 %	24.44 %	5.1 %	5.7 %	4.2 %	4.9 %

Table 6.12: Summary of the results obtained for  $\Delta\sigma(\text{WW})/\sigma(\text{WW})$  and  $\Delta\Gamma_H^{\text{tot}}/\Gamma_H^{\text{tot}}$  at  $\sqrt{s} = 250$  GeV with  $\mathcal{L} = 250 \text{ fb}^{-1}$ ,  $\sqrt{s} = 350$  GeV and  $\sqrt{s} = 500$  GeV, assuming  $500 \text{ fb}^{-1}$  of data. The results for  $\sqrt{s} = 350$  GeV and  $\sqrt{s} = 500$  GeV are taken from [37].

We notice that for large  $\sqrt{s}$  the measurement accuracies of the Higgs decay width improve for increasing  $m_H$ . At  $\sqrt{s} = 500$  GeV the WW-fusion contribution is very large and the Higgs-strahlung contribution is very small (cf. fig. 6.20). On the one hand, the improving results to higher  $m_H$  are due to the decreasing branching ratio of  $H \rightarrow b\bar{b}$ . For rising  $m_H$ , we have less b-quark events in the signal sample, thus the number of WW-fusion and Higgs-strahlung events with  $\nu\bar{\nu}b\bar{b}$  final state decreases. The already small Higgs-strahlung contribution decreases and thus is less disturbing in the fit procedure, whereas there are still many WW-fusion events remaining. Of course, the WW-fusion contribution decreases as well, but it is still large enough to be fitted on well. On the other hand, the measurement accuracies of  $BR(H \rightarrow \text{WW})$  increase for higher Higgs masses, since  $BR(H \rightarrow \text{WW})$  rises with increasing  $m_H$  (cf. fig. 2.6), so the resulting measurement accuracies of  $\Gamma_H^{\text{tot}}$  at  $\sqrt{s} = 500$  GeV are even better for higher  $m_H$ . In case of  $\sqrt{s} = 350$  GeV, we have slightly larger errors, since Higgs-strahlung and WW-fusion are of the same size. Since in both cases  $500 \text{ fb}^{-1}$  of data is assumed, at  $\sqrt{s} = 350$  GeV more time is needed for collecting that much data.

Compared to the results which are obtained at high  $\sqrt{s}$  via the WW-fusion cross section measurement, the results at  $\sqrt{s} = 250$  GeV with  $250 \text{ fb}^{-1}$  of data are related to larger errors in the measurement. We can conclude that for  $\sqrt{s} = 250$  GeV the measurement is not suitable and rather futile. More accuracy in the measurement can be achieved at higher centre of mass energies. This measurement is not suitable for a machine operating at  $\sqrt{s} = 250$  GeV instead of  $\sqrt{s} = 500$  GeV. Still, the determination of  $\Gamma_H^{\text{tot}}$  via the coupling  $g_{H\text{WW}}$  is superior to other indirect methods. In the following we briefly discuss the alternative methods.

### Comparison to other Indirect Methods

As already mentioned in section 2.2.2, next to the method used in this analysis, there are two other possibilities to determine  $\Gamma_H^{\text{tot}}$  indirectly.

One possibility works via the measurement of the  $\gamma\gamma \rightarrow H$  cross section at a  $\gamma\gamma$ -collider, in which a light Higgs boson can be observed through its  $b\bar{b}$ -decay. This measurement is combined with the measurement of  $BR(H \rightarrow \gamma\gamma)$  in  $e^+e^-$ -collisions. The cross section  $\sigma(\gamma\gamma \rightarrow H)$  can be determined with high precision. However, the corresponding decay branching ratio can only be measured with an accuracy of 19% for  $500 \text{ fb}^{-1}$  of data and 13% for  $1000 \text{ fb}^{-1}$ , since the SM prediction for  $BR(H \rightarrow \gamma\gamma)$  is only  $2 \cdot 10^{-3}$ . Dominated by the large uncertainty in the  $BR(H \rightarrow \gamma\gamma)$  determination, this method yields a larger error [47, 48].

Another alternative method works via the measurement of the Higgs-strahlung cross section combined with a measurement of  $BR(H \rightarrow WW)$ , assuming the  $SU(2) \times U(1)$  relation  $g_{HWW}/g_{HZZ} = 1/\cos(\theta_W)$  to be valid. By exploiting the measurement of the coupling  $g_{HZZ}$  from  $\sigma(e^+e^- \rightarrow HZ)$ , which at tree level is proportional to  $g_{HZZ}^2$ ,  $g_{HWW}$  can be determined. The accuracy on the total decay width measurement follows then from that of  $BR(H \rightarrow WW)$  and  $g_{HWW}$ . This option yields a relative precision between 5.6% for  $m_H = 120 \text{ GeV}$  and 3.6% for  $m_H = 160 \text{ GeV}$  at  $\sqrt{s} = 350 \text{ GeV}$  [14]. This method is less model-independent, but it achieves a similar result compared to the method which we have used in our analysis, at least in case of high centre of mass energies. Thus, in general methods via the determination of  $g_{HWW}$  are more effective and therefore superior to other methods.

The relative precision in the determination of  $\Gamma_H^{\text{tot}}$  in case of  $\mathcal{L} = 500 \text{ fb}^{-1}$  at  $\sqrt{s} = 350 \text{ GeV}$  for methods using the determination of  $g_{HWW}$  through WW-fusion and Higgs-strahlung are listed in tab. 6.13 [14]. The last row outlines the improvement which can be obtained when using in addition measurements at  $\sqrt{s} = 1 \text{ TeV}$  with  $\mathcal{L} = 1 \text{ ab}^{-1}$ .

Channel	$m_H = 120 \text{ GeV}$	$m_H = 140 \text{ GeV}$	$m_H = 160 \text{ GeV}$
$g_{HWW}$ from $\sigma(e^+e^- \rightarrow H\nu\bar{\nu})$	6.1 %	4.5 %	13.4 %
$g_{HWW}$ from $\sigma(e^+e^- \rightarrow HZ)$	5.6 %	3.7 %	3.6 %
$BR(WW)$ at $\sqrt{s} = 1 \text{ TeV}$	3.4 %	3.6 %	2.0 %

Table 6.13: Measurement accuracies of  $\Gamma_H^{\text{tot}}$  obtained by determining  $g_{HWW}$  through the WW-fusion and Higgs-strahlung cross sections at  $\sqrt{s} = 350 \text{ GeV}$  [14].

## Chapter 7

# Conclusion and Summary

We have performed a model-independent simulation measurement of the WW-fusion cross section and the total Higgs decay width at the ILC through the WW-fusion process  $e^+e^- \rightarrow \nu_e\bar{\nu}_e H \rightarrow \nu_e\bar{\nu}_e b\bar{b}$ . The choice of final state has relied on the preferred Higgs decay mode into b-quarks for  $m_H \leq 140$  GeV. We have used a centre of mass energy of  $\sqrt{s} = 250$  GeV, an integrated luminosity of  $\mathcal{L} = 250$  fb $^{-1}$ , and a beam polarisation of  $P(e^+e^-) = (0.3, -0.8)$ . The detector model ILD\_00 has been fully simulated. We have performed the analysis for four different Higgs masses:  $m_H = 120$  GeV, 126 GeV, 130 GeV, 140 GeV. The goal of this study was to give an estimation of the measurement accuracies of  $\Gamma_H^{\text{tot}}$  obtainable at the ILC at  $\sqrt{s} = 250$  GeV, since there are recent discussions of staging the ILC and beginning with a machine operating at  $\sqrt{s} = 250$  GeV for Higgs studies.

The measurement of the WW-fusion cross section relies on the measurement of the branching ratio  $BR(H \rightarrow b\bar{b})$ , since only  $H \rightarrow b\bar{b}$  decays have been selected. Since the branching ratio drops rapidly as the Higgs boson mass approaches the threshold for  $H \rightarrow WW$ , the expected precision of the cross section measurement does as well. Taking into account the uncertainties from the  $\chi^2$ -fit and from the branching ratio measurement, the expected statistical precision of the WW-fusion cross section measurement varies between 7.2% and 24.32% for  $m_H = 120$  GeV to  $m_H = 140$  GeV. The total Higgs decay width can be determined to a relative precision of 9.0% to 24.44% for  $m_H = 120$  GeV to  $m_H = 140$  GeV. Additionally, we have been able to give an estimation of the measurement accuracies of the Higgs-strahlung cross section. The final results of the accuracies in the WW-fusion cross section and total decay width measurement are summarised in tab. 7.1. Since the determination of the Higgs decay width through the measurement of the WW-fusion cross section is combined with a measurement of the branching ratio  $BR(H \rightarrow WW)$ , we introduce a small model-dependence to the analysis. The corresponding measurement has not been performed in our study, but it has been described briefly. Taking other more recent results for the measurement accuracies of  $BR(H \rightarrow WW)$  from a study for ILC

$m_H$ [GeV]	$\Delta N'_{WW}/N'_{WW}$	$\Delta N'_{ZH}/N'_{ZH}$	$\Delta\sigma(WW)/\sigma(WW)$	$\Delta\sigma(ZH)/\sigma(ZH)$	$\Delta\Gamma_H^{\text{tot}}/\Gamma_H^{\text{tot}}$
120	6.64 %	2.48 %	7.2 %	3.66 %	9.0 %
126	10.54 %	3.4 %	10.96 %	4.53 %	11.88 %
130	11.3 %	3.89 %	11.83 %	5.2 %	12.28 %
140	23.78 %	4.07 %	24.32 %	6.52 %	24.44 %

Table 7.1: Resulting measurement accuracies of the WW-fusion and Higgs-strahlung cross sections and of the Higgs decay width in the low Higgs mass region at  $\sqrt{s} = 250$  GeV.

performed at  $\sqrt{s} = 250$  GeV, we get larger errors in the measurement of  $\Gamma_H^{\text{tot}}$ . For example for  $m_H = 120$  GeV, we achieve an accuracy of 11.06% instead of 9.0%. In case of  $m_H = 126$  GeV we achieve a relative precision in the measurement of  $\Gamma_H^{\text{tot}}$  of 13.11%.

All important background processes have been taken into account. Due to the special features of two-photon background, this background can be easily excluded in the beginning of the analysis. Therefore, it was found to be negligible. The large background and Higgs-strahlung contributions at low centre of mass energies, where the WW-fusion contribution is small, make the analysis challenging at  $\sqrt{s} = 250$  GeV. During event selection, the massive background could be reduced relatively well, though it is still large after the selection. The largest WW-fusion efficiency has been achieved for  $m_H = 120$  GeV. In case of all four Higgs masses, Higgs-strahlung is dominant after the event selection. More cuts have been tested to remove Higgs-strahlung and background, but they had no further effect on the background reduction.

After the event selection, we have performed a  $\chi^2$ -fit on the missing mass distribution consisting of Higgs-strahlung, WW-fusion and background in order to determine the number of WW-fusion events that have passed the cuts. The errors of the fit on  $N'_{WW}$  increase to larger  $m_H$ , since the WW-fusion contribution is even smaller than it is for  $m_H = 120$  GeV, since  $BR(H \rightarrow b\bar{b})$  decreases. For every Higgs mass, the errors of the fit are always larger compared to the measurement accuracies of  $BR(H \rightarrow b\bar{b})$ , which worsen for higher  $m_H$ . In the determination of  $\Gamma_H^{\text{tot}}$ , the errors of the cross section measurement are always larger than the measurement accuracies of  $BR(H \rightarrow WW)$ . The improving measurement accuracies of  $BR(H \rightarrow WW)$  for higher  $m_H$ , which are due to the increasing branching ratio of  $H \rightarrow WW$  at high  $m_H$ , have no improving effect on the measurement accuracies of  $\Gamma_H^{\text{tot}}$ , which worsen for larger  $m_H$ .

At high  $\sqrt{s}$  the WW-fusion production cross section increases, whereas the background and Higgs-strahlung contributions decrease, thus making the determination of the WW-fusion cross section and total decay width easier. Referring to a former study on this topic for TESLA in the same Higgs mass region, the WW-fusion and Higgs-strahlung missing mass

---

distributions can be distinguished and fitted on well at  $\sqrt{s} = 350$  GeV. At  $\sqrt{s} = 500$  GeV the small Higgs-strahlung contribution can be suppressed very well, thus having almost entirely WW-fusion events in the end (cf. tab. 6.12). Both cases use  $\mathcal{L} = 500 \text{ fb}^{-1}$ . Therefore more time is needed for collecting data at  $\sqrt{s} = 350$  GeV. We have compared the indirect method used in our analysis with alternative options. We conclude that in general, the measurement of  $g_{\text{HWW}}$  provides the most effective model-independent method to determine the total Higgs decay width in case of high  $\sqrt{s}$  in the Higgs mass range under consideration. The former study for TESLA has shown that the measurement can be performed with an accuracy of  $\mathcal{O}(5\%)$  at centre of mass energies  $\sqrt{s} \geq 350$  GeV, assuming  $\mathcal{L} = 500 \text{ fb}^{-1}$ . Thus the results at high centre of mass energies show more accuracy in the measurement compared to  $\sqrt{s} = 250$  GeV. We conclude that the presented measurement of the Higgs decay width cannot be performed with high precision at  $\sqrt{s} = 250$  GeV and therefore is not suitable for a machine operating at this centre of mass energy.



# Appendix A

## Histograms

### A.1 $m_H = 120$ GeV

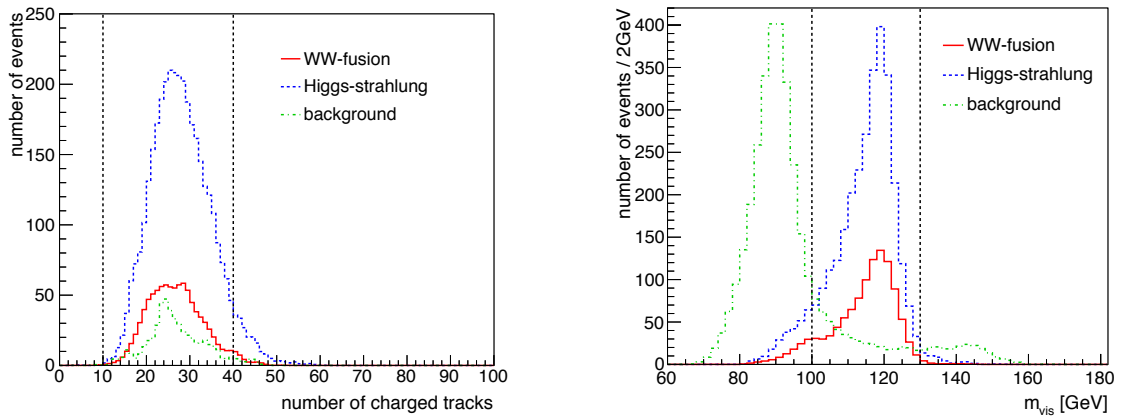


Figure A.1:  $N_{\text{ctrk}}$  and  $m_{\text{vis}}$  distribution for  $m_H = 120$  GeV after every other cut. A cut on  $N_{\text{ctrk}}$  and  $m_{\text{vis}}$  helps to reduce background and Higgs-strahlung.

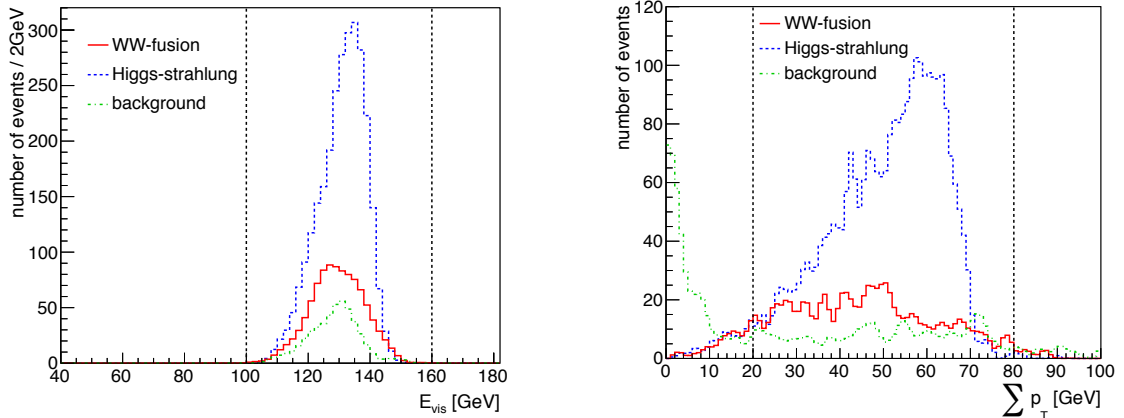


Figure A.2: Visible energy and total transverse momentum distribution for  $m_H = 120$  GeV after every other cut. A cut on  $\sum p_T$  helps to reduce background.

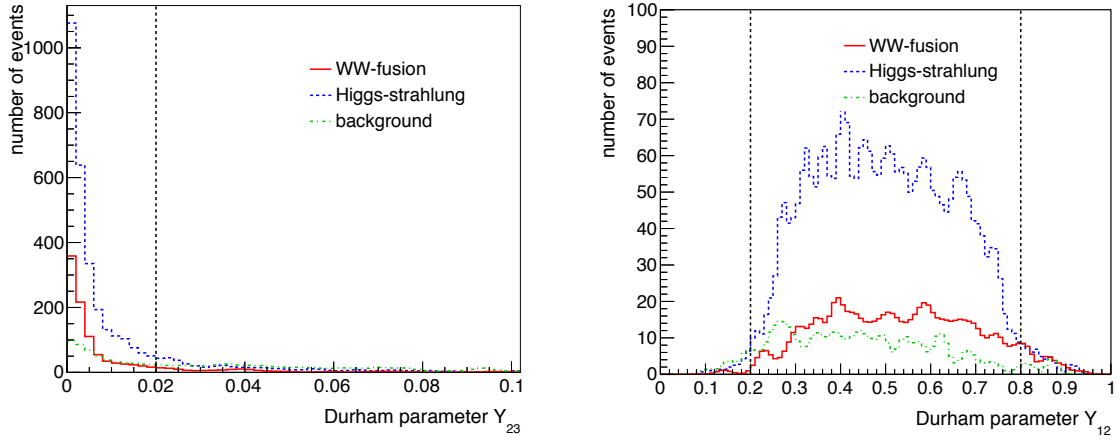


Figure A.3: *Durham parameter  $Y_{23}$  and  $Y_{12}$  for  $m_H = 120$  GeV after every other cut.*

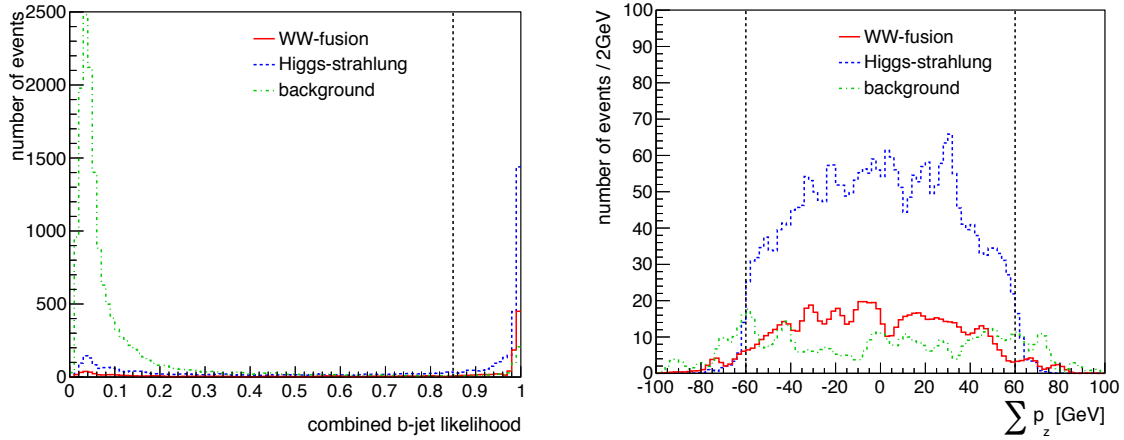


Figure A.4: *Combined b-jet likelihood and  $\sum p_z$  distribution for  $m_H = 120$  GeV after every other cut. The b-tag is very effective in background reduction.*

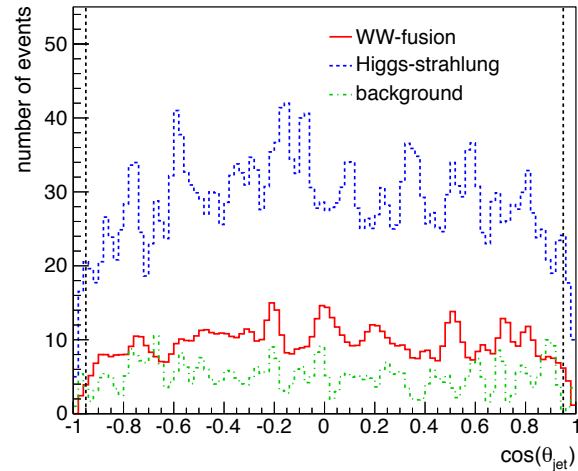


Figure A.5: *Angular distribution for  $m_H = 120$  GeV after every other cut.*

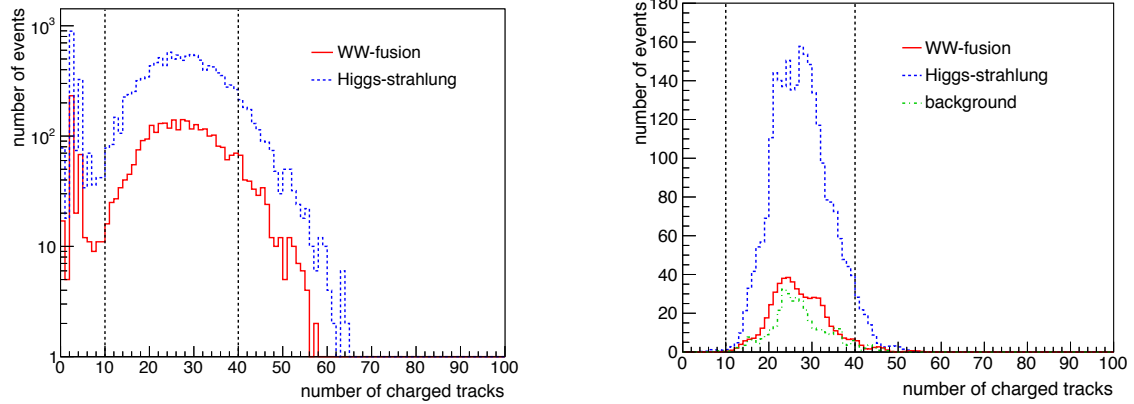
**A.2**  $m_H = 126$  GeV

Figure A.6: Number of charged tracks for  $m_H = 126$  GeV before (l.) and after (r.) every other cut. A cut on  $N_{\text{ctrk}}$  mainly reduces Higgs-strahlung.

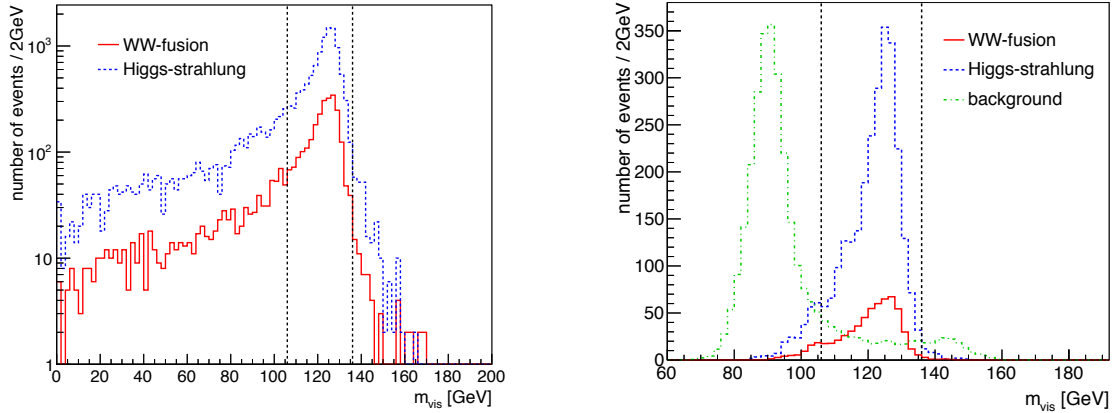


Figure A.7: Visible mass distribution for  $m_H = 126$  GeV before (l.) and after (r.) every other cut. A cut on  $m_{\text{vis}}$  helps to reduce background.

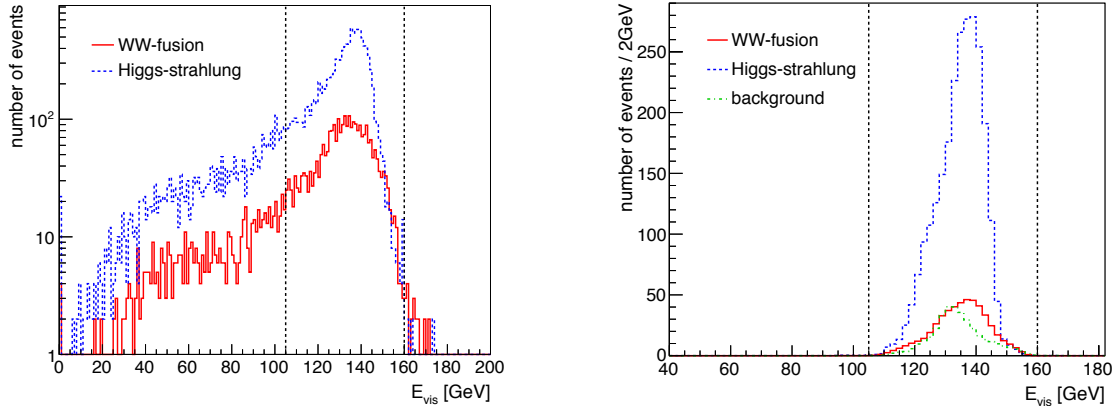


Figure A.8: Visible energy distribution for  $m_H = 126$  GeV before (l.) and after (r.) every other cut. A cut on  $E_{\text{vis}}$  is not effective in background reduction.

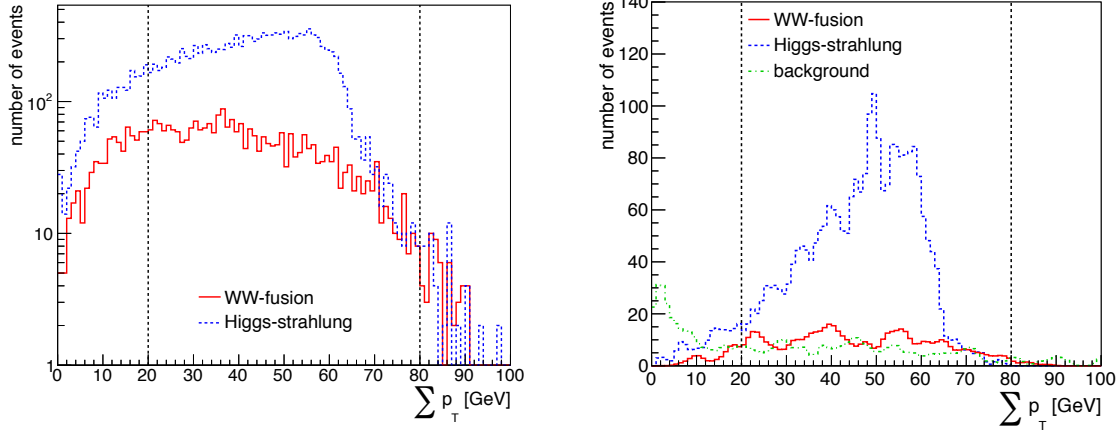


Figure A.9: Total transverse momentum for  $m_H = 126$  GeV before (l.) and after (r.) every other cut. A cut on  $\sum p_T$  helps to reduce background.

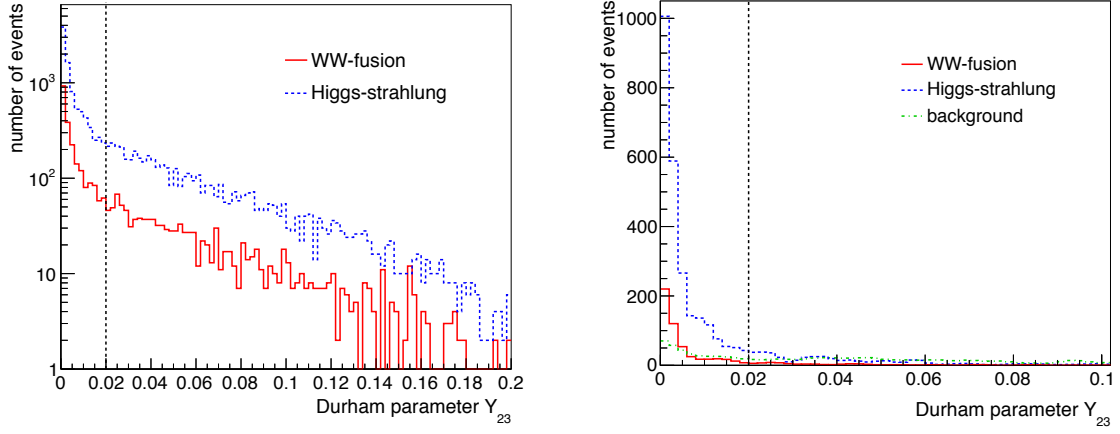


Figure A.10: Durham parameter  $Y_{23}$  for  $m_H = 126$  GeV before (l.) and after (r.) every other cut.

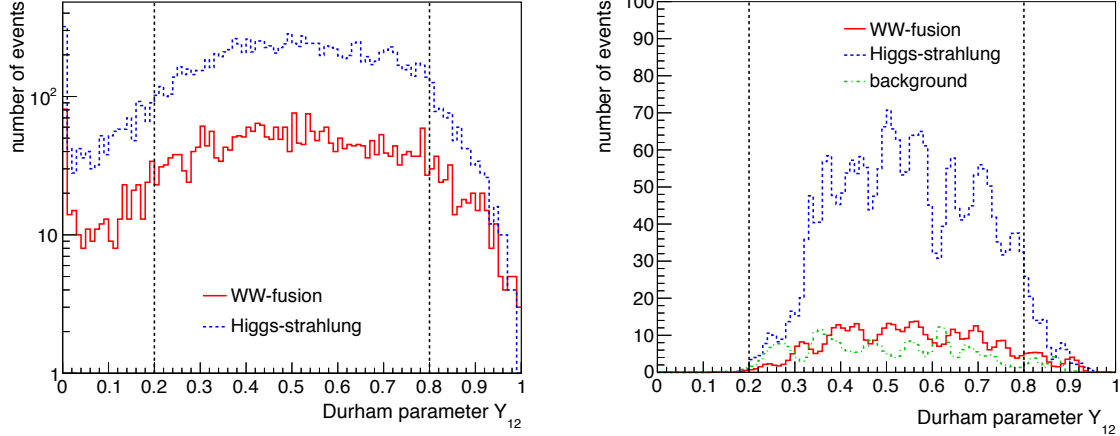


Figure A.11: Durham parameter  $Y_{12}$  for  $m_H = 126$  GeV before (l.) and after (r.) every other cut. A cut on  $Y_{12}$  mainly reduces Higgs-strahlung.

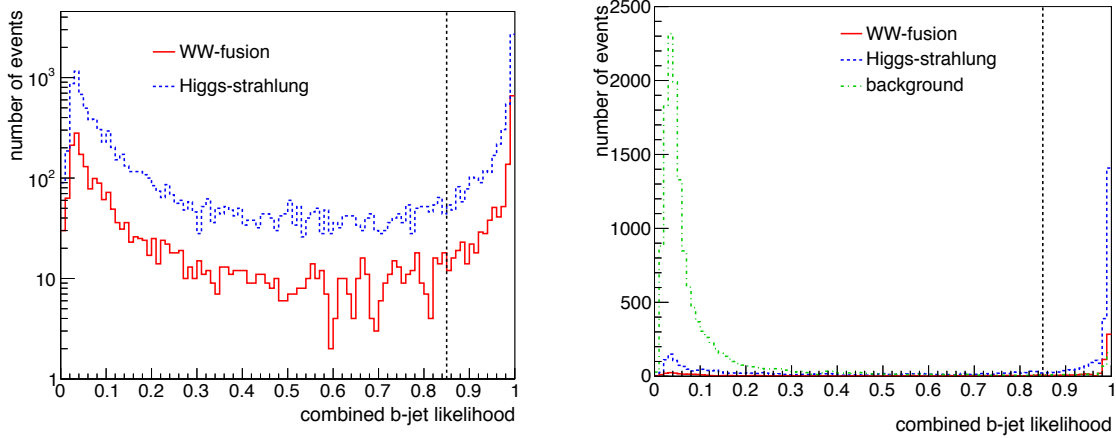


Figure A.12: Combined  $b$ -jet likelihood for  $m_H = 126$  GeV before (l.) and after (r.) every other cut. The  $b$ -tag is very effective.

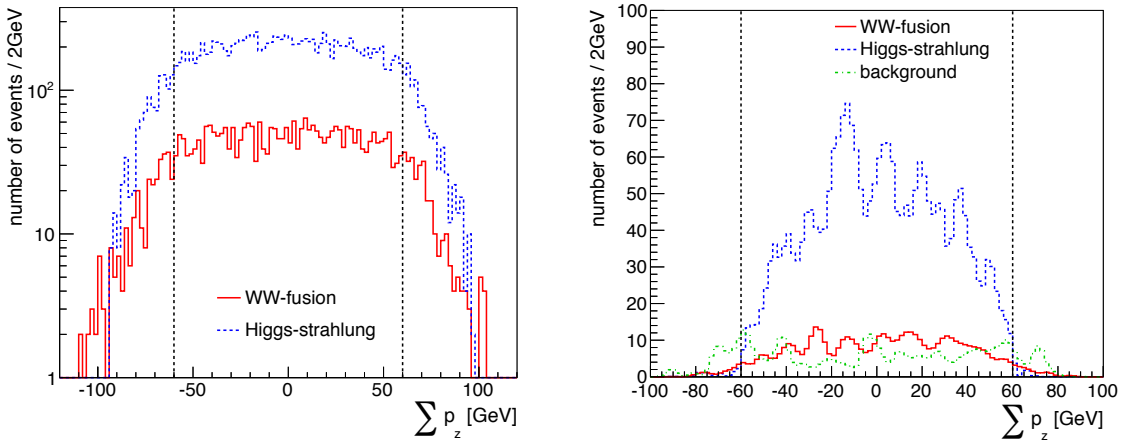


Figure A.13:  $\sum p_z$  distribution for  $m_H = 126$  GeV before (l.) and after (r.) every other cut. The cut helps to reduce background.

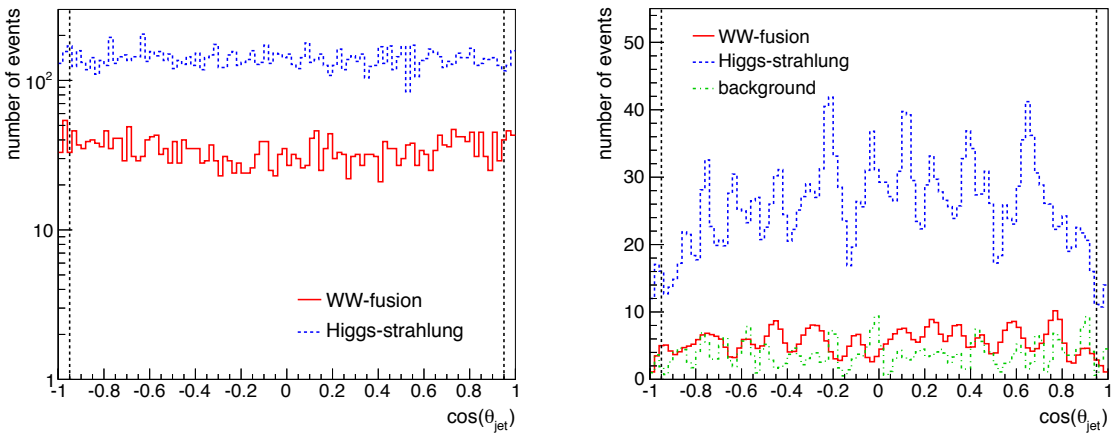


Figure A.14: Angular distribution for  $m_H = 126$  GeV before (l.) and after (r.) every other cut.

### A.3 $m_H = 130 \text{ GeV}$

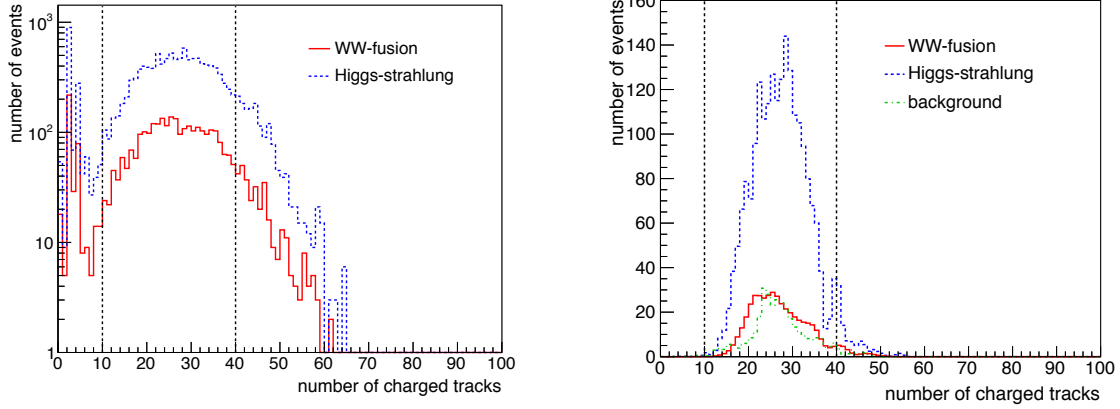


Figure A.15: Number of charged tracks for  $m_H = 130 \text{ GeV}$  before (l.) and after (r.) every other cut.

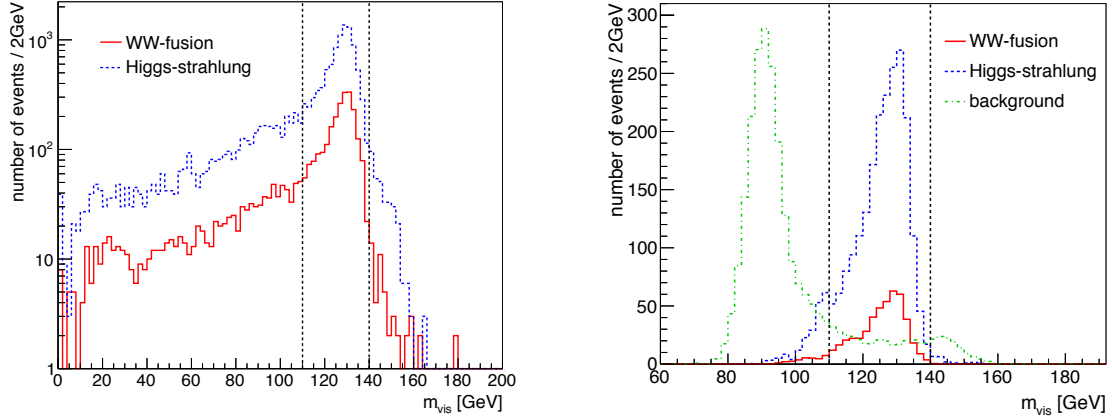


Figure A.16: Visible mass distribution for  $m_H = 130 \text{ GeV}$  before (l.) and after (r.) every other cut. A cut on  $m_{\text{vis}}$  helps to reduce background.

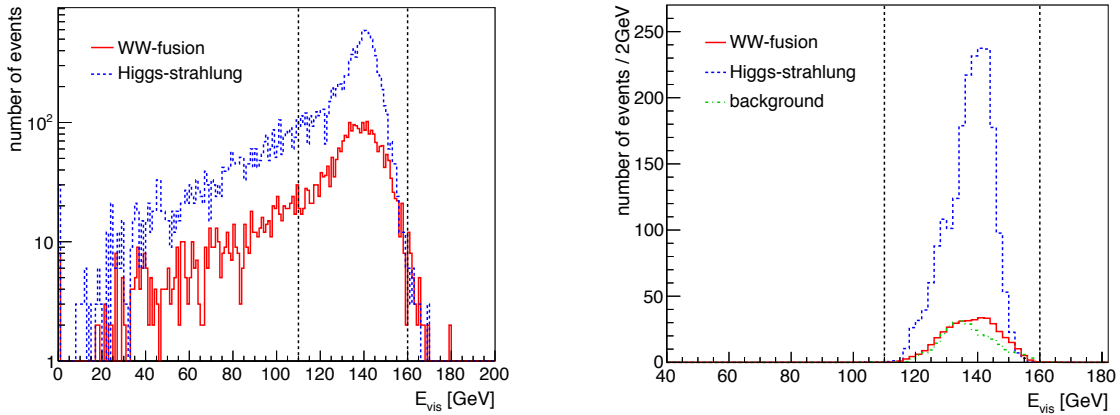


Figure A.17: Visible energy distribution for  $m_H = 130 \text{ GeV}$  before (l.) and after (r.) every other cut. A cut on  $E_{\text{vis}}$  does not remove background further.

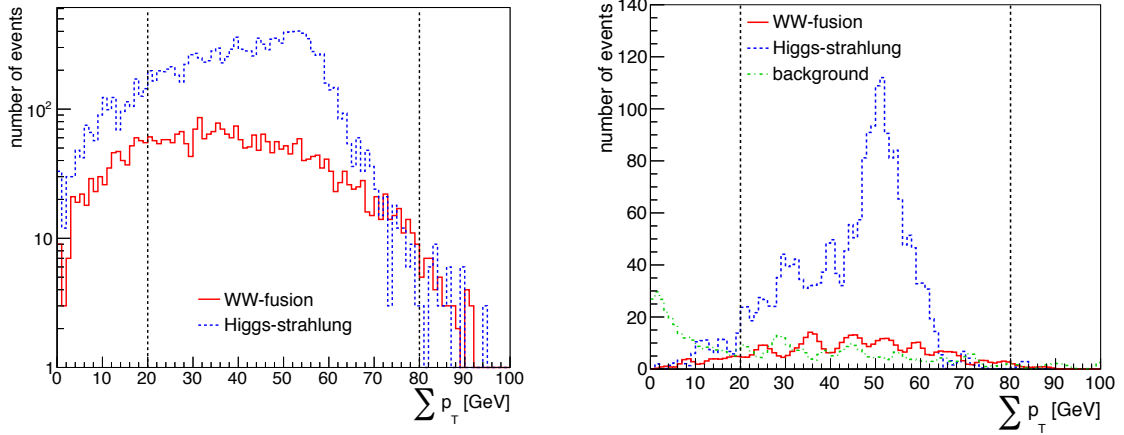


Figure A.18: Total transverse momentum for  $m_H = 130$  GeV before (l.) and after (r.) every other cut. A cut on  $\sum p_T$  helps to remove background.

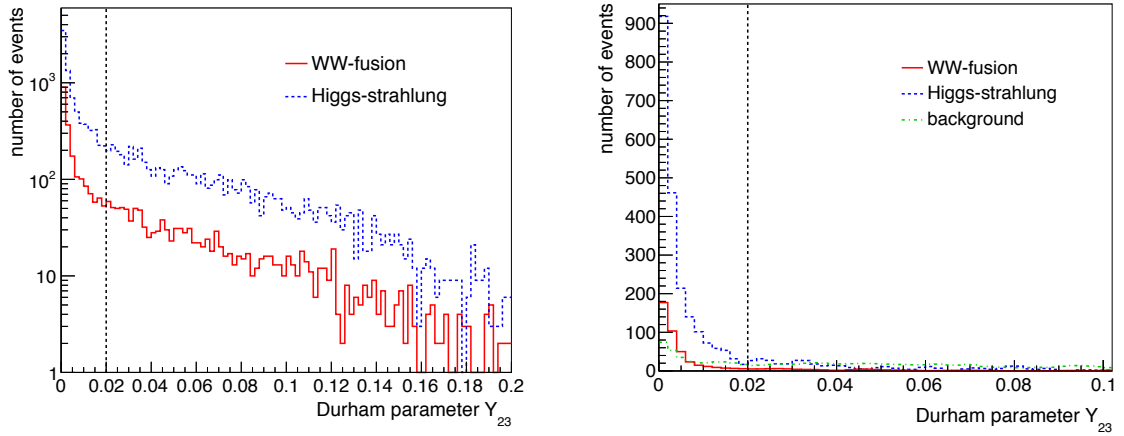


Figure A.19: Durham parameter  $Y_{23}$  for  $m_H = 130$  GeV before (l.) and after (r.) every other cut.

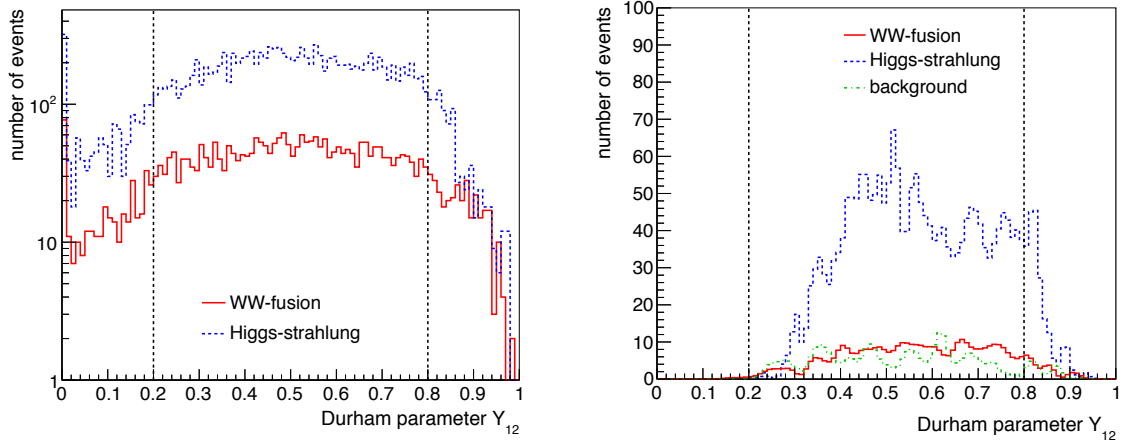


Figure A.20: Durham parameter  $Y_{12}$  for  $m_H = 130$  GeV before (l.) and after (r.) every other cut. A cut on  $Y_{12}$  helps to reduce Higgs-strahlung.

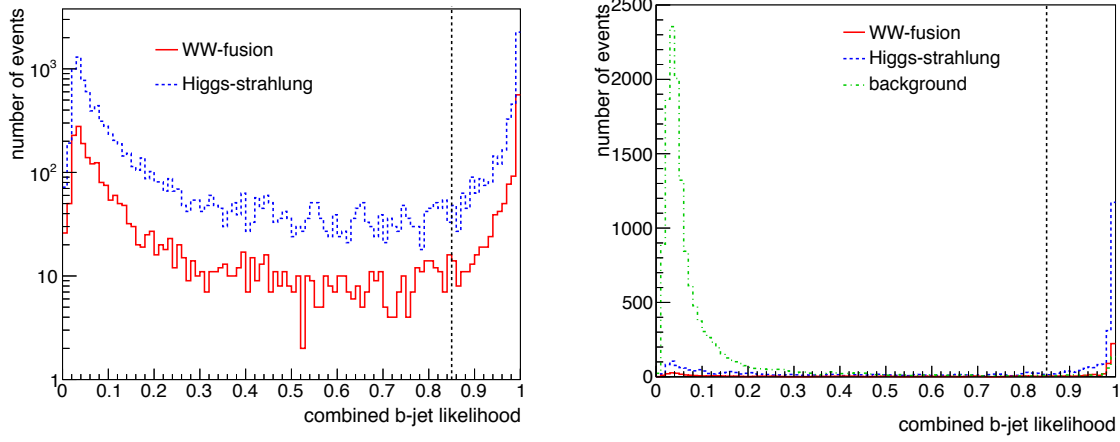


Figure A.21: Combined  $b$ -jet likelihood for  $m_H = 130$  GeV before (l.) and after (r.) every other cut. The  $b$ -tag is very effective in background reduction.

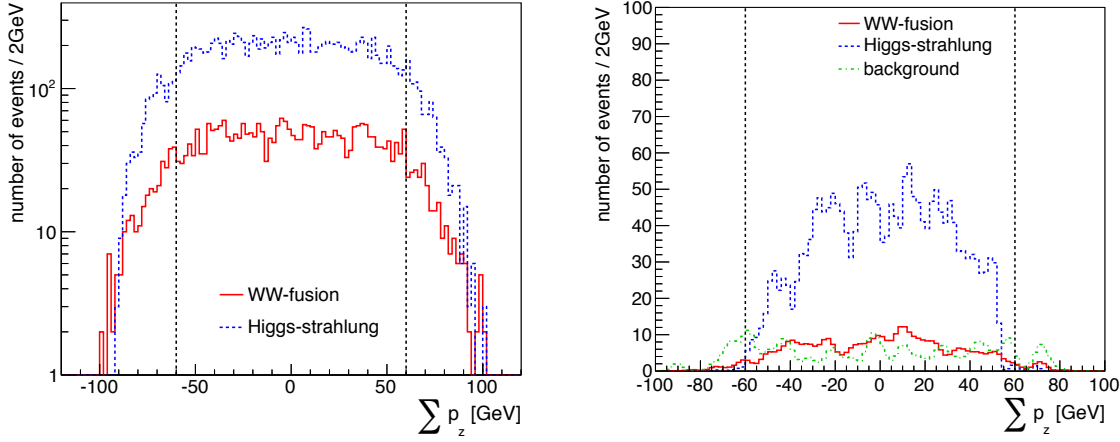


Figure A.22:  $\sum p_z$  distribution for  $m_H = 130$  GeV before (l.) and after (r.) every other cut. A cut on  $\sum p_z$  helps to reduce background.

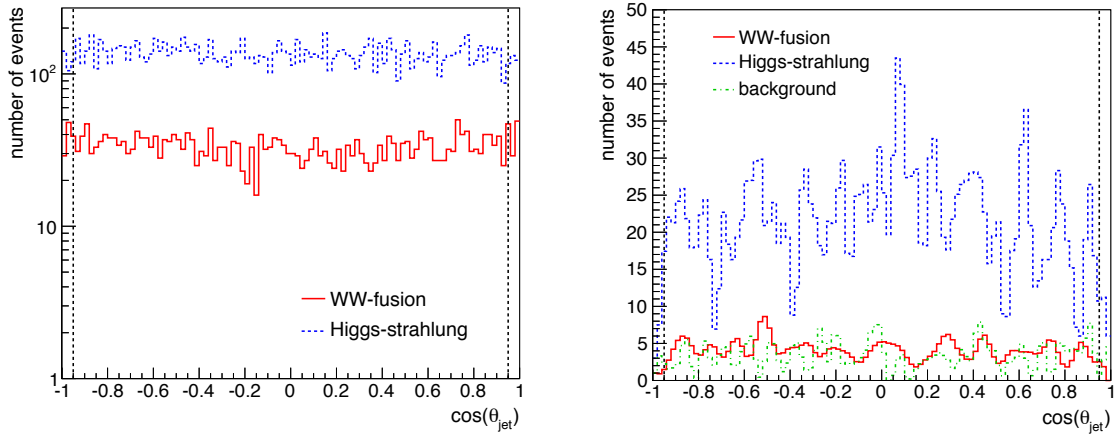


Figure A.23: Angular distribution for  $m_H = 130$  GeV before (l.) and after (r.) every other cut.

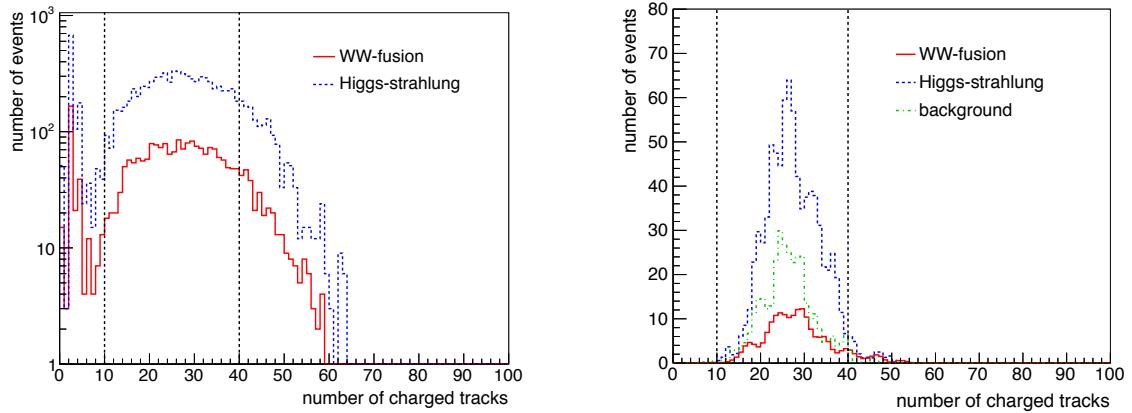
**A.4**  $m_H = 140$  GeV

Figure A.24: Number of charged tracks for  $m_H = 140$  GeV before (l.) and after (r.) every other cut.

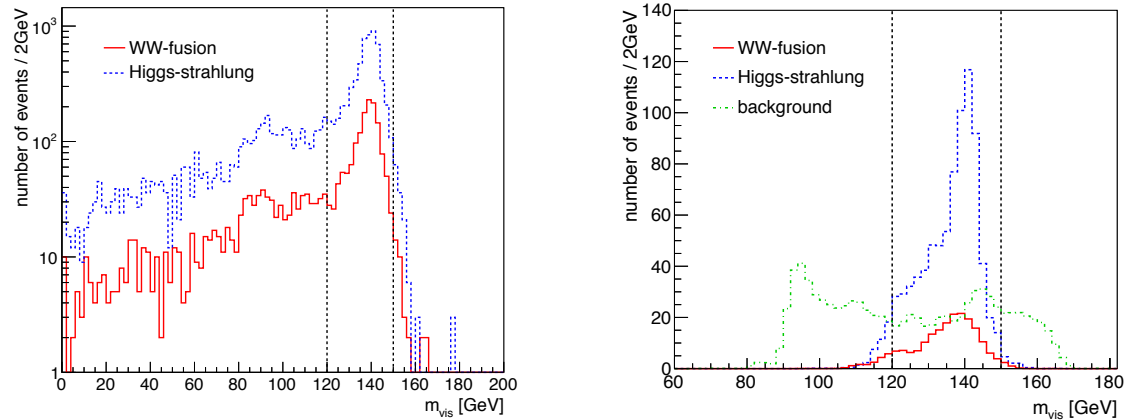


Figure A.25: Visible mass distribution for  $m_H = 140$  GeV before (l.) and after (r.) every other cut. A cut on  $m_{\text{vis}}$  helps to remove background.

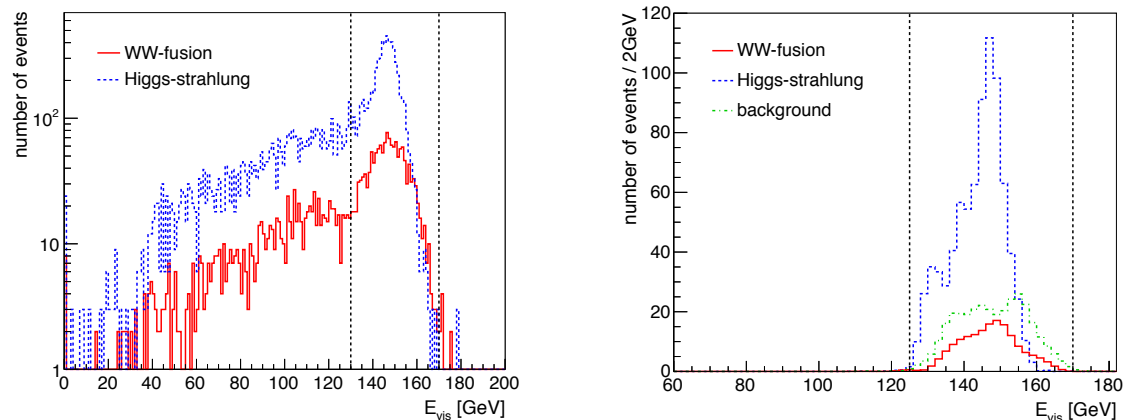


Figure A.26: Visible energy distribution for  $m_H = 140$  GeV before (l.) and after (r.) every other cut.

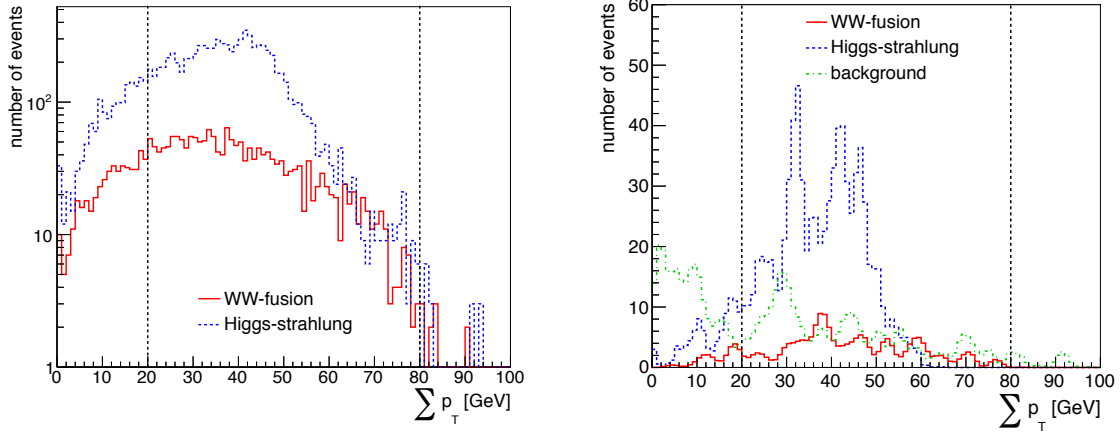


Figure A.27: Total transverse momentum for  $m_H = 140$  GeV before (l.) and after (r.) every other cut. The cut helps to remove background.

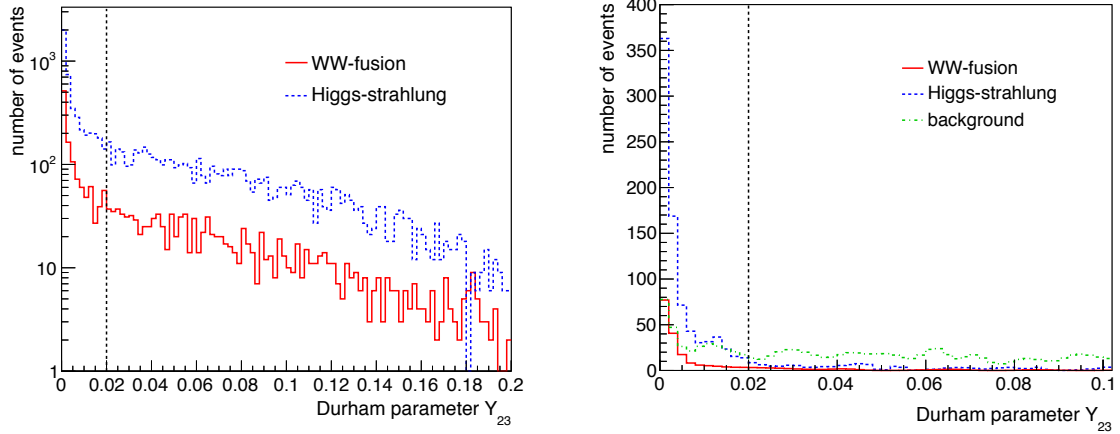


Figure A.28: Durham parameter  $Y_{23}$  for  $m_H = 140$  GeV before (l.) and after (r.) every other cut.

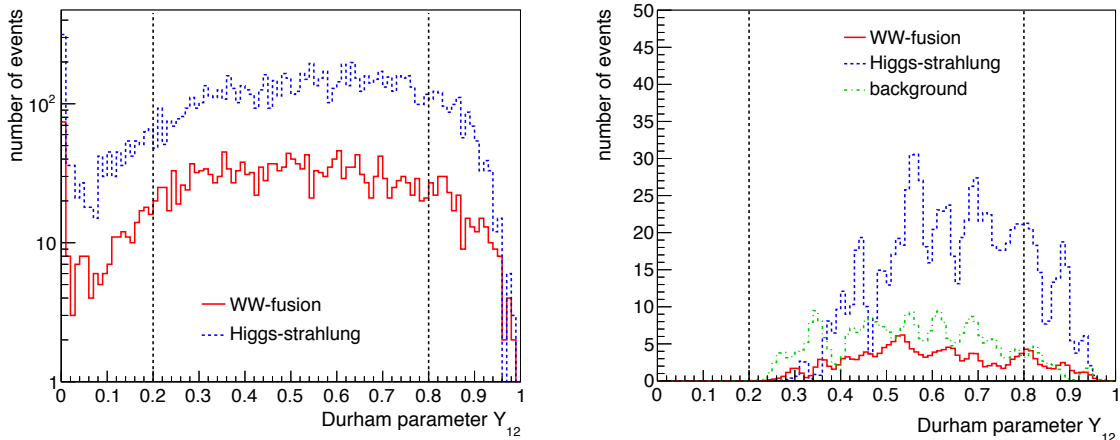


Figure A.29: Durham parameter  $Y_{12}$  for  $m_H = 140$  GeV before (l.) and after (r.) every other cut. A cut on  $Y_{12}$  helps to remove Higgs-strahlung.

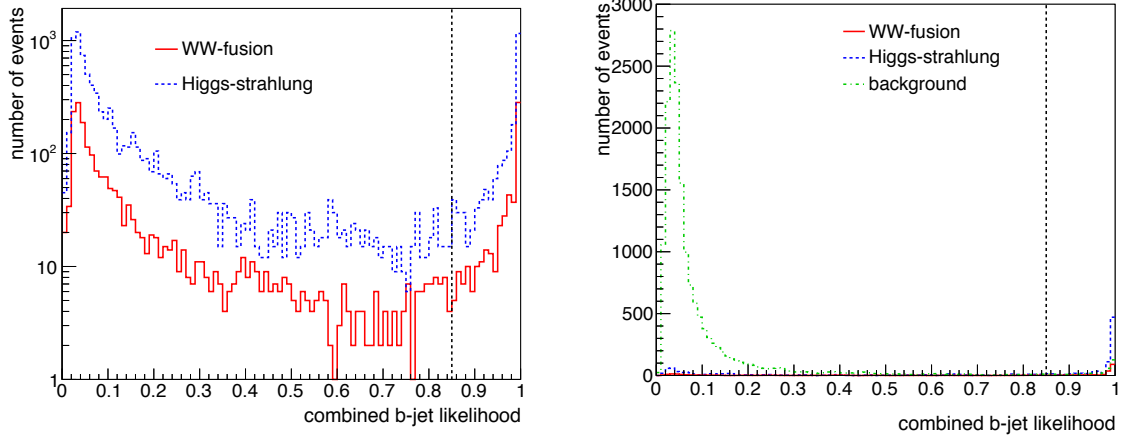


Figure A.30: *Combined b-jet likelihood for  $m_H = 140$  GeV before (l.) and after (r.) every other cut. The b-tag is very effective.*

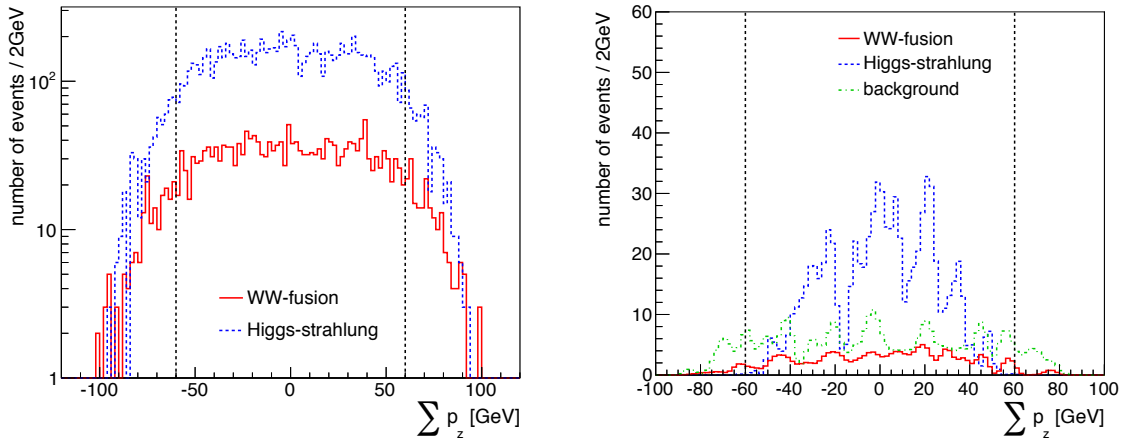


Figure A.31:  *$\sum p_z$  distribution for  $m_H = 140$  GeV before (l.) and after (r.) every other cut.*

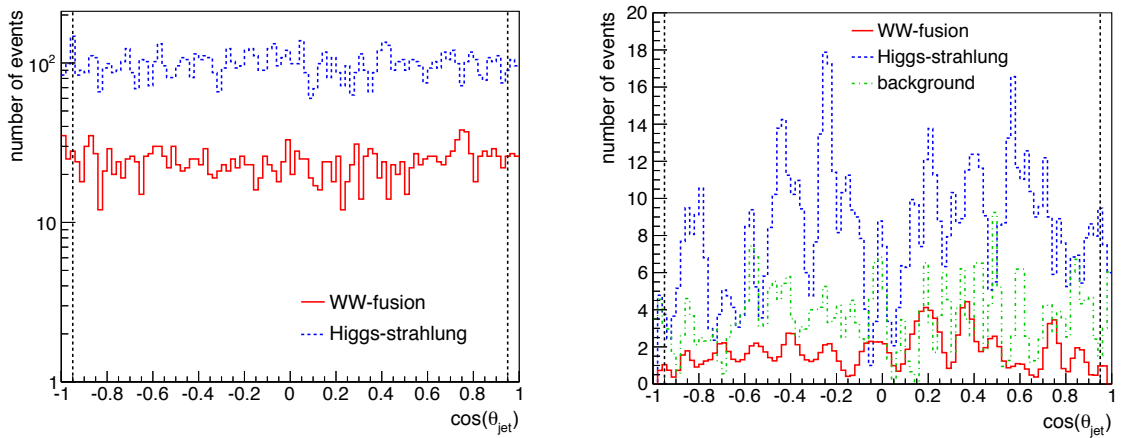


Figure A.32: *Angular distribution for  $m_H = 140$  GeV before (l.) and after (r.) every other cut.*



# List of Figures

2.1	Potential $V(\phi) = \frac{1}{2}\mu^2\phi^2 + \frac{1}{4}\lambda\phi^4$ for $\mu^2 > 0$ and $\mu^2 < 0$ . . . . .	6
2.2	2012 ATLAS results on the Higgs search in the two-photon channel . . . . .	10
2.3	2012 ATLAS results on the Higgs search: Probability to produce a signal-like excess . . . . .	10
2.4	Higgs boson production channels . . . . .	11
2.5	Production cross section $\sigma$ as a function of $\sqrt{s}$ and as a function of $m_H$ . . . . .	12
2.6	Branching ratios of the SM Higgs boson as a function of $m_H$ . . . . .	13
2.7	Total decay width of the SM Higgs boson as a function of $m_H$ . . . . .	14
3.1	Basic design of the ILC . . . . .	17
3.2	SiD detector and ILD detector . . . . .	19
5.1	W-boson pair production process . . . . .	25
5.2	Background processes with $b\bar{b}v_e\bar{v}_e$ final state . . . . .	26
5.3	Background processes with $b\bar{b}v_l\bar{v}_l$ final state . . . . .	26
5.4	Z-boson pair production process . . . . .	27
5.5	Single W- and Z-boson production process . . . . .	28
5.6	Two-fermion production process . . . . .	28
5.7	Production cross section $\sigma$ for SM processes as a function of $\sqrt{s}$ . . . . .	29
6.1	WW-fusion process and decay $H \rightarrow WW$ described by coupling $g_{HWW}$ . . . . .	33
6.2	Number of charged tracks for $m_H = 120$ GeV . . . . .	36
6.3	Visible mass distribution for $m_H = 120$ GeV . . . . .	37
6.4	Visible energy distribution for $m_H = 120$ GeV . . . . .	38
6.5	Total transverse momentum for $m_H = 120$ GeV . . . . .	39

6.6	Durham parameter $Y_{23}$ for $m_H = 120$ GeV . . . . .	40
6.7	Durham parameter $Y_{12}$ for $m_H = 120$ GeV . . . . .	41
6.8	Combined b-jet likelihood for $m_H = 120$ GeV . . . . .	42
6.9	Total momentum in beam direction for $m_H = 120$ GeV . . . . .	43
6.10	Angular distribution of the jets for $m_H = 120$ GeV . . . . .	44
6.11	Missing mass distribution of the signal for $m_H = 120$ GeV before cuts . . . . .	48
6.12	Missing mass distribution of the signal for $m_H = 126$ GeV before cuts . . . . .	48
6.13	Missing mass distribution of the signal for $m_H = 130$ GeV before cuts . . . . .	48
6.14	Missing mass distribution of the signal for $m_H = 140$ GeV before cuts . . . . .	48
6.15	Missing mass distribution of the background before cuts . . . . .	49
6.16	Missing mass distribution for $m_H = 120$ GeV after cuts . . . . .	50
6.17	Missing mass distribution for $m_H = 126$ GeV after cuts . . . . .	50
6.18	Missing mass distribution for $m_H = 130$ GeV after cuts . . . . .	50
6.19	Missing mass distribution for $m_H = 140$ GeV after cuts . . . . .	51
6.20	Missing mass distribution for $m_H = 120$ GeV at $\sqrt{s} = 350$ GeV (l.) and $\sqrt{s} = 500$ GeV (r.) for TESLA. . . . .	53
A.1	Number of charged tracks and visible mass distribution for $m_H = 120$ GeV after every other cut . . . . .	63
A.2	Visible energy and total transverse momentum distribution for $m_H = 120$ GeV after every other cut . . . . .	63
A.3	Durham parameter $Y_{23}$ and $Y_{12}$ for $m_H = 120$ GeV after every other cut . .	64
A.4	Combined b-jet likelihood and $\sum p_z$ distribution for $m_H = 120$ GeV after every other cut . . . . .	64
A.5	Angular distribution for $m_H = 120$ GeV after every other cut . . . . .	64
A.6	Number of charged tracks for $m_H = 126$ GeV before and after cuts . . . . .	65
A.7	Visible mass distribution for $m_H = 126$ GeV before and after cuts . . . . .	65
A.8	Visible energy distribution for $m_H = 126$ GeV before and after cuts . . . . .	65
A.9	Total transverse momentum distribution for $m_H = 126$ GeV before and after cuts . . . . .	66
A.10	Durham parameter $Y_{23}$ for $m_H = 126$ GeV before and after cuts . . . . .	66
A.11	Durham parameter $Y_{12}$ for $m_H = 126$ GeV before and after cuts . . . . .	66
A.12	Combined b-jet likelihood for $m_H = 126$ GeV before and after cuts . . . . .	67

---

A.13 $\sum p_z$ distribution for $m_H = 126$ GeV before and after cuts . . . . .	67
A.14 Angular distribution for $m_H = 126$ GeV before and after cuts . . . . .	67
A.15 Number of charged tracks for $m_H = 130$ GeV before and after cuts . . . . .	68
A.16 Visible mass distribution for $m_H = 130$ GeV before and after cuts . . . . .	68
A.17 Visible energy distribution for $m_H = 130$ GeV before and after cuts . . . . .	68
A.18 Total transverse momentum distribution for $m_H = 130$ GeV before and after cuts . . . . .	69
A.19 Durham parameter $Y_{23}$ for $m_H = 130$ GeV before and after cuts . . . . .	69
A.20 Durham parameter $Y_{12}$ for $m_H = 130$ GeV before and after cuts . . . . .	69
A.21 Combined b-jet likelihood for $m_H = 130$ GeV before and after cuts . . . . .	70
A.22 $\sum p_z$ distribution for $m_H = 130$ GeV before and after cuts . . . . .	70
A.23 Angular distribution for $m_H = 130$ GeV before and after cuts . . . . .	70
A.24 Number of charged tracks for $m_H = 140$ GeV before and after cuts . . . . .	71
A.25 Visible mass distribution for $m_H = 140$ GeV before and after cuts . . . . .	71
A.26 Visible energy distribution for $m_H = 140$ GeV before and after cuts . . . . .	71
A.27 Total transverse momentum distribution for $m_H = 140$ GeV before and after cuts . . . . .	72
A.28 Durham parameter $Y_{23}$ for $m_H = 140$ GeV before and after cuts . . . . .	72
A.29 Durham parameter $Y_{12}$ for $m_H = 140$ GeV before and after cuts . . . . .	72
A.30 Combined b-jet likelihood for $m_H = 140$ GeV before and after cuts . . . . .	73
A.31 $\sum p_z$ distribution for $m_H = 140$ GeV before and after cuts . . . . .	73
A.32 Angular distribution for $m_H = 140$ GeV before and after cuts . . . . .	73



# List of Tables

2.1	Lepton and quark classification by their charge $Q/ e $ . . . . .	4
2.2	SM gauge bosons . . . . .	4
5.1	Number of events in the $\nu_l \bar{\nu}_l H$ signal samples . . . . .	31
5.2	Number of WW-fusion events in the signal samples . . . . .	31
5.3	Number of Higgs-strahlung events in the signal samples . . . . .	31
5.4	Background samples . . . . .	31
6.1	Number of Higgs-strahlung, WW-fusion and background events before the event selection . . . . .	35
6.2	Cutflow and number of WW-fusion and Higgs-strahlung events for the four Higgs masses after every cut . . . . .	44
6.3	Efficiency $\epsilon$ of WW-fusion and Higgs-strahlung events for the four different Higgs masses. . . . .	45
6.4	Cutflow and number of events for every background process for $m_H = 120$ GeV	45
6.5	Cutflow and number of events for every background process for $m_H = 126$ GeV	45
6.6	Cutflow and number of events for every background process for $m_H = 130$ GeV	46
6.7	Cutflow and number of events for every background process for $m_H = 140$ GeV	46
6.8	Number of WW-fusion, Higgs-strahlung and background events resulting from the $\chi^2$ -fit for each of the four Higgs masses. . . . .	49
6.9	Measurement accuracies of the WW-fusion cross section obtained in the low Higgs mass region at $\sqrt{s} = 250$ GeV, assuming $250 \text{ fb}^{-1}$ of data. . . . .	51
6.10	Measurement accuracies of the Higgs-strahlung cross section obtained for the low Higgs mass range at $\sqrt{s} = 250$ GeV, assuming $250 \text{ fb}^{-1}$ of data. . . . .	53

6.11 Measurement accuracies of the total decay width of the Higgs boson in the low Higgs mass region at $\sqrt{s} = 250$ GeV. Value * is extrapolated from the other results. . . . .	56
6.12 Summary of the results obtained for $\Delta\sigma(\text{WW})/\sigma(\text{WW})$ and $\Delta\Gamma_{\text{H}}^{\text{tot}}/\Gamma_{\text{H}}^{\text{tot}}$ at $\sqrt{s} = 250$ GeV, $\sqrt{s} = 350$ GeV and $\sqrt{s} = 500$ GeV. . . . .	57
6.13 Measurement accuracies of $\Gamma_{\text{H}}^{\text{tot}}$ obtained using indirect methods dealing with the determination of $g_{\text{HWW}}$ . . . . .	58
7.1 Final results achieved for $\Delta\sigma(\text{WW})/\sigma(\text{WW})$ , $\Delta\sigma(\text{ZH})/\sigma(\text{ZH})$ and $\Delta\Gamma_{\text{H}}^{\text{tot}}/\Gamma_{\text{H}}^{\text{tot}}$	60

# Bibliography

- [1] D. GRIFFITHS: *Introduction to Elementary Particles*, Second revised edition, WILEY-VCH Verlag GmbH & Co. KGaA, 2008.
- [2] D. H. PERKINS: *Introduction to High Energy Physics*, 4th Edition, Cambridge University Press, 2000.
- [3] F. HALZEN, A. D. MARTIN: *Quarks & Leptons: An Introductory Course in Modern Particle Physics*, John Wiley & Sons, 1984.
- [4] TA-PEI CHENG, LING-FONG LI: *Gauge theory of elementary particle physics*, Oxford University Press, 1984.
- [5] M. E. PESKIN, D. V. SCHROEDER: *An introduction to Quantum Field Theory*, Westview Press, 1995.
- [6] J. BERINGER ET AL. (PDG): Phys. Rev. **D86** (2012) 010001.
- [7] D. AAD ET AL. (ATLAS COLLABORATION), Phys. Rev. Lett. **108**, 111803 (2012).
- [8] D. AAD ET AL. (ATLAS COLLABORATION), Phys. Rev. Lett. **108**, 111802 (2012).
- [9] S. CHATRCHYAN ET AL. (CMS COLLABORATION), Phys. Rev. Lett. **108**, 111804 (2012).
- [10] D. CARMI, A. FALKOWSKI, E. KUFLIK, T. VOLANSKY, J. ZUPAN: *Higgs After the Discovery: A Status Report*, arXiv:1207.1718v3 [hep-ph], 2012.
- [11] ATLAS COLLABORATION: *Observation of a new particle in the search for the Standard Model Higgs boson with the ATLAS detector at LHC*, arXiv:1207.7214v1 [hep-ex], 2012.
- [12] CMS COLLABORATION: *Observation of a new boson at a mass of 125 GeV with the CMS experiment at the LHC*, arXiv:1207.7235v1 [hep-ex], 2012.
- [13] R. D. HEUER ET AL.: *TESLA Technical Design Report Part 3: Physics at an e<sup>+</sup>e<sup>-</sup> Linear Collider*, DESY-2001-011, arXiv:hep-ph/0106315v1.

- [14] A. DJOUADI, J. LYKKEN, K. MÖNIG, ET AL.: *ILC Reference Design Report Volume 2 - Physics at the ILC*, arXiv:0709.1893v1 [hep-ph], 2007.
- [15] M. SPIRA, P. ZERWAS: Lect. Notes Phys. **512** (1998) 161-225, arXiv:hep-ph/9803257v2.
- [16] A. DJOUADI, J. KALINOWSKI, M. SPIRA: Comput. Phys. Commun. **108** : 56-74, 1998, arXiv:hep-ph/9704448v1.
- [17] S. HEINEMAYER, ET AL.: *Toward High Precision Higgs boson Measurements at the International Linear e<sup>+</sup>e<sup>-</sup> Collider*, arXiv:hep-ph/0511332v2, 2006.
- [18] M. SCHUMACHER: *Higgs Physics at a Future e<sup>+</sup>e<sup>-</sup> Linear Collider*, arXiv:hep-ph/0107273v1, 2001.
- [19] THE ILD CONCEPT GROUP: *The International Large Detector: Letter of Intent*, arXiv:1006.3396v1 [hep-ex], 2010.
- [20] N. PHINNEY, N. TOGE, N. WALKER, ET AL.: *ILC Reference Design Report Volume 3 - Accelerators*, arXiv:0712.2361v1 [physics.acc-ph], 2007.
- [21] INTERACTIONS.ORG Particle Physics News and Resources  
<http://www.interactions.org/imagebank/>, 2008.
- [22] *International Linear Collider Submission to European Strategy Discussion 2012*, ILC ESD-2012/1.
- [23] H. AIHARA, P. BURROWS, M. OREGLIA: SiD Letter of Intent, arXiv:0911.0006v1 [physics.ins-det], 2009.
- [24] J. BRAU, Y. OKADA, N. WALKER, ET AL.: *ILC Reference Design Report Volume 1 - Executive Summary*, arXiv:0712.1950v1 [physics.acc-ph], 2007.
- [25] T. BEHNKE, C. DAMERELL, J. JAROS, A. MYAMOTO, ET AL.: *ILC Reference Design Report Volume 4 - Detectors*, arXiv:0712.2356v1 [physics.ins-det], 2007.
- [26] M. THOMSON: J. Phys. Conf. Ser. **110** (2008) 092032.
- [27] W. KILIAN, T. OHL, J. REUTER: Eur. Phys. J. **C71** (2011) 1742, arXiv:0708.4233 [hep-ph].
- [28] T. SJÖSTRAND: Comput. Phys. Commun. **82** (1994) 74.
- [29] M. MORETTI, T. OHL, J. REUTER: *O'Mega An Optimizing Matrix Element Generator*, arXiv:hep-ph/0102195-rev, 2001.
- [30] ILCSoft: <http://ilcsoft.desy.de/portal>.

- [31] G. MUSAT, Proceedings of LCWS 2004, 437-439;  
 P. MORA DE FREITAS, Proceedings of LCWS 2004, 441-444;  
 See also [http://ilcsoft.desy.de/portal/software\\_packages/mokka/](http://ilcsoft.desy.de/portal/software_packages/mokka/).
- [32] GEAR: [http://ilcsoft.desy.de/portal/software\\_packages/gear/](http://ilcsoft.desy.de/portal/software_packages/gear/).
- [33] F. GAEDE, T. BEHNKE, N. GRAF, T. JOHNSON: *LCIO - A persistency framework for linear collider simulation studies*, arXiv:physics/0306114v1 [physics.data-an]; See also <http://lcio.desy.de/>.
- [34] F. GAEDE: Nucl. Instrum. Meth. **A559** (2006) 177;  
[http://ilcsoft.desy.de/portal/software\\_packages/marlin/](http://ilcsoft.desy.de/portal/software_packages/marlin/).
- [35] RENE BRUN AND FONS RADEMAKERS: Nucl. Inst. & Meth. in Phys. Res. **A389** (1997) 81-86. See also <http://root.cern.ch/>.
- [36] W. KILIAN, M. KRÄMER, P. ZERWAS: Phys. Lett. **B373** (1996) 135,  
 arXiv:hep-ph/9512355v1.
- [37] N. MEYER: *Higgs-Boson at TESLA - Studies on production in WW-fusion and total decay width*, Diploma thesis, University of Hamburg, 2000;  
 K. DESCH, N. MEYER: *Higgs Production in WW-fusion at TESLA*,  
 LC-PHSM-2001-025, 2001.
- [38] A. RASPEREZA: *Search for Neutral Higgs Bosons in  $e^+e^-$ -Collisions*, Dissertation, HU Berlin, 2002.
- [39] <http://www-zeuthen.desy.de/ILC/physics/>.
- [40] G. MOORTGAT-PICK: J. Phys. Conf. Ser. **295** (2011) 012159.
- [41] N. BROWN, W. J. STIRLING: Z. Phys. **C53** (1992) 629;  
 S. CATANI ET AL.: Phys. Lett. **B269** (1991) 432.
- [42] D. BAILEY ET AL.: Nucl. Inst. & Meth. in Phys. Res. **A610** (2009) 573-589.
- [43] H. LI, R. PÖSCHL, F. RICHARD: *HZ Recoil Mass and Cross Section Analysis in ILD*, LC-PHSM-2009-006, arXiv:1202.1439v1 [hep-ex], 2012.
- [44] H. ONO, A. MIYAMOTO: *Higgs Branching Fraction Study in ILC*, Proceedings of LCWS 2011, arXiv:1202.4955v1 [hep-ex];  
 H. ONO, <http://ilcagenda.linearcollider.org/sessionDisplay.py?sessionId=19&confId=5414#20120424>, KILC12.
- [45] G. BORISOV, F. RICHARD: *Precise measurement of Higgs decay rate into  $WW^*$  at future  $e^+e^-$ -Linear Colliders*, arXiv:hep-ph/9905413v1.

- [46] J. TIAN, H. ONO, KILC12, <http://ilcagenda.linearcollider.org/sessionDisplay.py?sessionId=19&confId=5414#20120424>.
- [47] P. NIEZURAWSKI: *Final results for the SM Higgs-boson production at the Photon Collider*, Presented at the International Linear Collider Workshop LCWS05, Stanford, USA, arXiv:hep-ph/0507004v1.
- [48] E. BOOS, J.-C. BRIENT, D. W. REID, H. J. SCHREIBER, R. SHANIDZE: *Measuring the Higgs Branching Fraction into two Photons at Future Linear ee Colliders*, Eur. Phys. J. **C19**: 455-461, 2001, arXiv:hep-ph/0011366v1.
- [49] D. BINOSI, L. THEUSSL: *JaxoDraw - A graphical user interface for drawing Feynman diagrams*, <http://dx.doi.org/10.1016/j.cpc.2009.02.020>.

# Eidesstattliche Versicherung

Hiermit versichere ich, Claude Fabienne Dürig, dass ich die vorliegende Arbeit selbstständig und nur unter Benutzung der angegebenen Literatur und Hilfsmittel angefertigt habe. Stellen, die wörtlich oder sinngemäß aus anderen Schriften entnommen sind, habe ich als solche kenntlich gemacht. Die Arbeit hat in gleicher oder ähnlicher Form noch keiner Prüfungsbehörde vorgelegen.

I hereby certify that the work presented here was accomplished by myself and without the use of illegitimate means or support, and that no sources and tools were used other than those cited.

Bonn: \_\_\_\_\_

Signature: \_\_\_\_\_



